基於凸分析之盲蔽非負訊號源分離於生物醫學與超光譜影像分析

Convex Analysis Based Non-negative Blind Source Separation for Biomedical and Hyperspectral Image Analysis

論文作者：詹宗翰
Tsung-Han Chan

指導教授：祁忠勇 博士
Dr. Chong-Yung Chi
馬榮健 博士
Dr. Wing-Kin Ma

國 立 清 華 大 學

通 訊 工 程 研 究 所

博 士 論 文

中 華 民 國 九 十 八 年 七 月

國 立 清 華 大 學

博碩士論文全文電子檔著作權授權書

（提供授權人裝訂於紙本論文書名頁之次頁用）

本授權書所授權之學位論文，為本人於國立清華大學通訊工程研究所 ＿＿＿甲＿＿＿組， 97 學年度第 二 學期取得博士學位之論文。

論文題目：基於凸分析之盲蔽非負訊號源分離於生物醫學與超光譜影像分析

指導教授：祁忠勇、馬榮健

■ 同意

本人茲將本著作，以非專屬、無償授權國立清華大學與台灣聯合大學系統圖書館：基於推動讀者間「資源共享、互惠合作」之理念，與回饋社會與學術研究之目的，國立清華大學及台灣聯合大學系統圖書館得不限地域、時間與次數，以紙本、光碟或數位化等各種方法收錄、重製與利用；於著作權法合理使用範圍內，讀者得進行線上檢索、閱覽、下載或列印。

論文電子全文上載網路公開之範圍及時間：

本校及台灣聯合大學系統區域網路	■ 立即公開
校外網際網路	■ 立即公開

■ 全文電子檔送交國家圖書館

授 權 人：詹宗翰

親筆簽名：＿＿＿＿＿＿＿＿＿＿

中華民國 98 年 8 月 17 日

國 立 清 華 大 學

博碩士紙本論文著作權授權書

（提供授權人裝訂於全文電子檔授權書之次頁用）

本授權書所授權之學位論文，為本人於國立清華大學通訊工程研究所 _____甲_____組， 97 學年度第__二__學期取得博士學位之論文。

論文題目：基於凸分析之盲蔽非負訊號源分離於生物醫學與超光譜影像分析
指導教授：祁忠勇、馬榮健

■ 同意

本人茲將本著作，以非專屬、無償授權國立清華大學，基於推動讀者間「資源共享、互惠合作」之理念，與回饋社會與學術研究之目的，國立清華大學圖書館得以紙本收錄、重製與利用；於著作權法合理使用範圍內，讀者得進行閱覽或列印。

本論文為本人向經濟部智慧局申請專利(未申請者本條款請不予理會)的附件之一，申請文號為：_____，請將論文延至____年____月____日再公開。

授 權 人：詹宗翰

親筆簽名：_詹宗翰_____

中華民國 98 年 8 月 17 日

國家圖書館
博碩士論文電子檔案上網授權書

（提供授權人裝訂於紙本論文本校授權書之後）

ID：GH000935608

本授權書所授權之論文為授權人在國立清華大學通訊工程研究所 97 學年度第_二_學期取得博士學位之論文。

論文題目：基於凸分析之盲蔽非負訊號源分離於生物醫學與超光譜影像分析

指導教授：祁忠勇、馬榮健

茲同意將授權人擁有著作權之上列論文電子全文（含摘要），非專屬、無償授權國家圖書館，不限地域、時間與次數，以微縮、光碟或其他各種數位化方式將上列論文重製，並得將數位化之上列論文及論文電子檔以上載網路方式，提供讀者基於個人非營利性質之線上檢索、閱覽、下載或列印。

☐ 讀者基於非營利性質之線上檢索、閱覽、下載或列印上列論文，應依著作權法相關規定辦理。

☐ 論文電子全文上載網路公開之範圍及時間：立即公開。

授權人：詹宗翰

親筆簽名：＿＿＿＿＿＿＿＿

民國 98 年 8 月 17 日

國立清華大學博士學位論文
指導教授推薦書

學　系
<u>　通訊工程　</u>研究所<u>　詹宗翰　</u>君所提之論文

<u>基於凸分析之盲蔽非負訊號源分離於生物醫</u>
<u>學與超光譜影像分析</u>

經由本人指導撰述，同意提付審查。

指導教授＿＿＿＿＿＿＿＿＿＿＿＿（簽章）

中華民國　９８　年　７　月　３０　日

國立清華大學博士學位論文

考試委員審定書

學　系
　通訊工程　研究所　詹宗翰　君所提之論文

基於凸分析之盲蔽非負訊號源分離於生物醫
學與超光譜影像分析

經本委員會審查，符合博士資格標準。

學位考試委員會

主持人＿＿＿＿＿＿＿＿＿＿＿＿＿＿（簽章）
委　員＿＿＿＿＿＿＿＿＿＿　＿＿＿＿＿＿＿＿＿＿
　　　　＿＿＿＿＿＿＿＿＿＿　＿＿＿＿＿＿＿＿＿＿
　　　　＿＿＿＿＿＿＿＿＿＿　＿＿＿＿＿＿＿＿＿＿
　　　　＿＿＿＿＿＿＿＿＿＿　＿＿＿＿＿＿＿＿＿＿

中華民國　９８　年　７　月　３０　日

中文摘要

本論文探討一種在現實世界中(如多通道生物醫學影像分析和超光譜影像分析)可廣泛應用的技術–盲蔽非負訊號源分離(non-negative blind source separation, nBSS)。完全不同於現存相關方法所使用的技術，如非負擴充之獨立成分分析(independent component analysis)和非負矩陣分解(non-negative matrix factorization)，我們在本論文中利用凸幾何(convex geometry)發展出不須訊號源統計獨立/不相關性之兩種 nBSS 的框架(framework)。

第一種框架稱為 convex analysis of mixtures of non-negative sources (CAMNS)。CAMNS 巧妙地利用實用性的模型假設(稱為訊號源局部主導(local dominance))連接 nBSS 和凸幾何之關係。它推導出基於凸分析之 nBSS 確定性準則，進而將 nBSS 的問題精練成找尋一個多面集(polyhedral set)所有極點(extreme point)的問題(即極點列舉問題(extreme point enumeration problem))。我們推衍出兩個基於線性規劃(linear program)的方法來有效地找出極點，其一是分析式的且提供完善的理論保證；而另一方法是啟發式的，當模型假設並不完全滿足時可提供較好的強健性(robustness)。我們針對幾組數據進行模擬，並與目前具代表性的 nBSS 方法比較，其結果證明了 CAMNS 的方法具有較好的效能。此外，真實生物醫學影像的實驗結果也評估出 CAMNS 的高度實用性。

在高光譜遙感中，分解一個數據立方體(data cube)成不同物質之光譜特徵(即端元(endmember))與其相應豐度分數(abundance fractions)，稱為高光譜分解。此高光譜分解

本質與 nBSS 問題具有許多共同性質，而且在分析固體表面的礦物成分方面，扮演著至關重要的角色。第二種框架是從一個全新的凸分析與最佳化角度透視高光譜分解。我們利用凸分析的概念分別針對 Winter 於九零年代晚期所提出「端元可由觀測像素集合內之最大體積單純型(simplex)的頂點所決定」及 Craig 於九零年代中期所提出「端元可由最小體積且同時包括觀測像素集合之單純型的頂點所決定」的直觀想法(但無嚴格的分析與証明)來制定出兩個高光譜分解(hyperspectral unmixing)的最佳化問題。我們藉由證明當訊號源是局部主導時，此兩者最佳化問題的最佳解得出真正的端元，以証明兩者最佳化問題的關係，並且說明了如何利用交替式(alternating)線性規劃有效地解決這兩個問題。我們並以幾組數據進行 Monte Carlo 模擬，其結果驗證了理論分析的結果，也充分展示出我們所提出算法的功效。最後利用 1997 年內華達州 Cuprite 礦址所採集的數據進行高光譜影像實驗，証實我們提出方法的實驗結果與地面實況(ground truth)具有高度的相似性。

我們相信本論文所提出的兩個 nBSS 框架已對 nBSS 的研究領域提供了新的維度，不僅將在生物醫學影像和高光譜影像分析上期望成為重要的訊號處理工具，且對於非負訊號源分離的其他潛在應用如分析化學、基因訊號之去卷積和超高解析度亦是如此。

Abstract

This dissertation deals with the topic of non-negative blind source separation (nBSS), a widely-applicable technique in many real-world applications, such as multichannel biomedical image analysis and hyper-spectral image analysis. Fundamentally, unlike the skills involved in relevant existing frameworks, such as non-negative extension of independent component analysis (ICA) and non-negative matrix factorization (NMF), we exploit convex geometry to develop two nBSS frameworks without any source statistical independence/uncorrelatedness assumption.

The first framework called convex analysis of mixtures of non-negative sources (CAMNS) makes use of an insightful and practical model assumption (called source local dominance) to connect nBSS and convex geometry. It leads to a deterministic, convex analysis based nBSS criterion that boils down nBSS problem to the problem of finding all the extreme points of an observation-constructed polyhedral set (or an extreme point enumeration problem). We derive two linear programming based methods for efficiently locating the extreme points. One is analytically based and provides some appealing theoretical guarantees, while the other is heuristic but provides better robustness when model assumptions are not perfectly satisfied. Simulation results for several data sets are presented to demonstrate the efficacy of the CAMNS-based methods over several existing benchmark nBSS methods. In addition, experimental results with real biomedical images are presented to evaluate the high practical applicability of CAMNS.

In hyperspectral remote sensing, unmixing a data cube into the spectral signatures (or endmenbers) and their corresponding mixing proportion (or abundance fractions) plays a crucial role in analyzing the mineralogical composition of a solid surface. Such an unmixing problem nature has a lot in common with nBSS problem. The second framework describes a new convex analysis and optimization perspective to hyperspectral unmixing. By the notion of convex analysis, we formulate two optimization problems for hyperspectral unmixing, which have intuitive ideas (or beliefs without any rigorous analysis and proof) that *"the endmembers are determined by vertices of the maximum volume simplex within all the observed pixels"* proposed by Winter in late 1990, and that *"the endmembers are determined by the vertices of a minimum volume simplex enclosing all the observed pixels"* proposed by Craig in mid 1990, respectively. We show the relation between the two formulated optimization problems, by proving that both of their optimal solutions yield the true endmembers when the abundance fractions (sources) are locally dominant. We also illustrate how the two problems can be efficiently solved by alternating linear programming. Monte Carlo simulation results for several data sets are presented to validate our analytical results, and demonstrate the efficacy of the proposed algorithms. The experimental results of our nBSS method for real hyperspectral image data collected by airbone visible/infrared imaging spectrometer flight over the Cuprite mining site, Nevada, in 1997, show a high agreement with the reported ground truth.

We believe that the proposed two nBSS frameworks in this dissertation have provided new dimensions to the nBSS research area, and will expectantly serve as important signal processing tools not only for biomedical image analysis and hyperspectral image analysis but also for other potential applications, such as analytical chemistry, deconvolution of genomic signals, and superresolution image reconstruction, where the sources are non-negative in nature.

Acknowledgments

Working toward my Ph.D. degree is a hard and challenging experience, and it was with the best support from numerous people I could succeed in that. I feel honored and duty-bound to express my gratitude to them. To begin with, I wish to express my sincere gratitude to my advisor, Prof. Chong-Yung Chi, for his expert guidance, constant inspiration, and full support. His meticulous attitude and high research expectations made him as my role model for my future career. I wish to extend my deepest appreciation to my co-advisor, Prof. Wing-Kin Ma, Chinese University of Hong Kong, for his selfless dedication, motivation, and great patience with which he taught me how to do a good research from scratch. His various research dimensions and fluent presentations inspired me to emulate him. Though my advisor and co-advisor are not a man of many words, their oral and written comments are highly perceptive, helpful, and appropriate. They were instrumental in making me understand the core of research.

I am indebted to Prof. Yue Wang, Virginia Polytechnic Institute and State University (Virginia Tech), who guided me at Virginia Tech during my overseas exchange program from Mar. 2008 to Feb. 2009. I would like to thank him for his kindly and patiently teaching me how to think a problem "outside the box." His rich experience in managing collaboration with numerous research groups made me admire him. I also deeply appreciate Prof. Elizabeth Hillman, Columbia University, NY, and Dr. Richard Levenson, Cambridge Research & Instrumentation, Inc., for their valuable

and constant company make me have more strength to accomplish my Ph.D. degree. I firmly believe that getting this Ph.D. degree is a new beginning, and will strive my best to keep going further.

Tsung-Han Chan

Hsinchu, Aug 18, 2009.

Table of Contents

List of Figures

List of Tables

List of Notations

$\mathbb{R}, \mathbb{R}^N, \mathbb{R}^{M \times N}$ Set of real numbers, $N \times 1$ vectors, $M \times N$ matrices

$\mathbb{R}_+, \mathbb{R}_+^N, \mathbb{R}_+^{M \times N}$ Set of non-negative real numbers, $N \times 1$ vectors, $M \times N$ matrices

$\mathbf{X}^\dagger$ Moore-Penrose inverse or pseudo-inverse of matrix $\mathbf{X}$

$\mathbf{1}_N$ $N \times 1$ vector with all the components equal to unity

$\mathbf{I}_N$ $N \times N$ identity matrix

$\mathbf{e}_i$ Unit vector of proper dimension with the ith entry equal to 1

$\succeq$ Componentwise inequality

$\| \cdot \|$ Euclidean norm

$\mathcal{N}(\boldsymbol{\mu}, \boldsymbol{\Sigma})$ Gaussian distribution with mean $\boldsymbol{\mu}$ and covariance $\boldsymbol{\Sigma}$

$\mathrm{diag}\{x_1, \ldots, x_N\}$ Diagonal matrix with diagonal entries $x_1, \ldots, x_N$

$\det(\mathbf{X})$ Determinant of a square matrix $\mathbf{X}$

Chapter 1

Introduction

Blind source separation (BSS) is a signal processing problem and its purpose is to separate source signals from observations, without information of how the source signals are mixed in the observations. BSS has been a very challenging topic in the signal processing community for many years, and it has stimulated significant research interest due to its wide range of applications. BSS has been applied to wireless communications and speech processing, and recently there has been significant contribution to image analysis.

BSS methods are 'blind' in the sense that the mixing process is not known, at least not explicitly. In fact, it is universally true that some certain assumptions on the source characteristics (and sometimes on the mixing characteristics as well) would be exploited during the blind source separation process. Conventional BSS approaches aim to design a demixing matrix such that its outputs (or source estimates) fulfill some criteria established from the assumptions made. For instance, independent component analysis (ICA) [1, 2], a major and very representative BSS framework on which many BSS methods are based, assumes that the sources are mutually uncorrelated/independent random processes possibly with non-Gaussian distributions. Other possible source assumptions include quasi-stationarity [3, 4] (speech signals are

quasi-stationary), and boundness of the source magnitudes [5, 6, 7] (suitable for digital signals). In choosing an advisable BSS method for a particular application, it is important to examine whether the underlying assumptions of the BSS method are suitable for the application of interest.

This dissertation focuses on non-negative blind source separation (nBSS), in which the source signals are assumed to take on non-negative values. In fact, images are non-negative signals. Potential applications of nBSS include biomedical imaging [8], hyperspectral imaging [9], and analytical chemistry [10]. In biomedical imaging and hyperspectral imaging, for instance, there are realistic, meaningful problems where nBSS may serve as a powerful image analysis tool.

In nBSS, utilization of source non-negativity to achieve perfect separation has been an intriguing subject that has received much attention recently. Presently available nBSS methods can be classified into two groups. One group is similar to ICA, which assumes that the sources are non-negative and mutually statistically uncorrelated or independent. Methods falling in this group include non-negative ICA (nICA) [11], stochastic non-negative ICA (SNICA) [12], and Bayesian positive source separation (BPSS) [13], to name a few. nICA takes source non-negativity into account, and has been shown to provide perfect separation when the sources have non-vanishing density around zero (which is also called the well-grounded condition) [14]. SNICA uses a simulated annealing algorithm for extracting non-negative sources under the minimum mutual information criterion. BPSS also uses source non-negativity. It applies Bayesian estimation with both the sources and mixing matrix assumed to be Gamma distributed. However, the statistical source independence assumption may be violated in certain image scenarios such as biomedical image analysis [8] and hyperspectral image analysis [9].

Another group of nBSS methods does not rely on statistical assumptions. Roughly speaking, these methods explicitly exploit source non-negativity or even mixing ma-

2

trix non-negativity, with an attempt to achieve some kind of least square fitting criterion. Methods falling in this group are generally known as (or may be vaguely recognized as) non-negative matrix factorization (NMF) [15, 16]. An advantage with NMF is that it does not operate on the premise of mutual uncorrelatedness/independence as in the first group of nBSS methods. NMF is a nonconvex constrained optimization problem. A popular way of handling NMF is to apply gradient descent [16], but it is known to be suboptimal and slowly convergent. A projected quasi-Newton method has been incorporated in NMF to speed up its convergence [17]. Alternatively, alternating least squares (ALS) [18, 19, 20, 21] can also be applied. Fundamentally, the original NMF [15, 16] may not yield unique factorization, and this means that NMF may fail to provide perfect separation. Possible circumstances under which NMF draws a unique decomposition can be found in [22]. Simply speaking, unique NMF would be possible if both the source signals and mixing process exhibit some form of sparsity. Some recent works have focused on incorporating additional penalty functions or constraints, such as sparse constraints, to strengthen the NMF uniqueness [23, 24].

Unlike ICA and NMF from their onset, in this dissertation nBSS problems are deterministically studied via convex analysis without involving the design of demixing matrix. Convex analysis and optimization techniques have drawn considerable attention in signal processing, serving as powerful tools for various topics such as communications [25, 26, 27, 28, 29, 30], array signal processing [31], and sensor networks [32]. Also, the endeavor of employing convex analysis here is motivated by the fact that some concepts, such as affine hull and convex hull, are quite suitable for analysis of the biomedical images [33, 34] and hyperspectral images [35, 36].

In Chapter 4, we present our nBSS framework, called convex analysis of mixtures of non-negative sources (CAMNS) [37, 38, 39], which utilizes convex geometry to analyze the relationships between the observations and sources in a vector space, where

3

each vector represents an image after vectorization. Apart from source non-negativity, CAMNS also adopts a deterministic assumption called *local dominance*. We initially introduced this assumption to capture the sparse characteristics of biomedical images [33,34], but we also found that the local dominance assumption can be perfectly or approximately satisfied for high-contrast images such as human portraits. (We however should stress that the local dominance assumption is different from the sparsity assumption in compressive sensing.) Under the local dominance assumption and some standard nBSS assumptions, we can show using convex analysis that the true source vectors are exactly the extreme points of an observation-constructed polyhedral set. This geometrical discovery is surprising, with a profound implication that perfect blind source separation can be achieved by solving an extreme point finding problem that is fundamentally different from any other existing nBSS approaches to our best knowledge. Then two methods for practical implementation of CAMNS are presented. The first one is analysis-based, using LPs to locate all the extreme points systematically. Its analysis-based construction endows it with several theoretical appealing properties. Though the second one is heuristic in approach, it is intuitively expected to have better robustness against mismatch of model assumptions. In our simulation results, the second method was found to exhibit better separation performance over the first. In addition, we also conducted several experiments to show the wide applicability of our CAMNS framework.

In hyperspectral remote sensing, unmixing a data cube into the spectral signatures and their corresponding abundance fractions plays a crucial role in analyzing the mineralogical composition of a solid surface. Such an unmixing problem nature has a lot in common with nBSS problem. In Chapter 5, we provide a convex analysis and optimization perspective to hyperspectral unmixing problems [40, 41, 42], which analytically proves the intuitive ideas of Winter's [43, 44] and Craig's [45] unmixing criteria, respectively. In contrast to CAMNS framework where each vector represents

4

a vectorized image, hyperspectral unmixing problems here are analyzed by applying convex geometry to the observed pixel vector space, where each vector represents the radiances over all the observed spectral bands. We first perform dimension reduction of the observed pixels through a convex analysis concept called affine set fitting [39], and show that all the dimension-reduced pixels are enclosed by a simplex. The main idea of Winter's (or Craig's) unmixing criterion is to find a maximum-volume (or minimum-volume) simplex within (or enclosing) all the dimension-reduced pixels. Based on these two unmixing criteria, we formulate two optimization problems for hyperspectral unmixing, and prove that both of them lead to unique identification of the true endmembers when the local dominance assumption holds true. We also develop two unmixing algorithms to handle the formulated problems in a cyclic fashion by solving a sequence of LPs, which can be readily implemented by any available LP software. Finally, some simulation results and experimental results for real hyperspectral data are presented to demonstrate the superior performance of the proposed methods over several existing benchmark methods.

To understand the position of the proposed nBSS over numerous areas of BSS, we give an overview of the existing BSS algorithms in Figure 1.

The dissertation is organized as follows. In Chapter 2, the nBSS problem statement, general assumptions, and potential applications are presented. In Chapter 3, we review some basic concepts of convex analysis, which would be useful for understanding of the mathematical derivations in the ensuing development. The CAMNS framework that includes new nBSS criterion and two methods for fulfilling the criterion are introduced in Chapter 4. Then, in Chapter 5, we introduce our convex analysis based problem formulations for hyperspectral unmixing, and the associated alternating LPs methods for solving them. Finally, some conclusions and future directions are provided in Chapter 6.

5

Approach		Statistical							Deterministic		
Criterion		High-order statistics	Second-order statistics			Information theoretic		Bayesian framework	Least square fitting		Convex geometry
Features	Uncorrelatedness	Yes	Yes			Yes			No		No
	Independence	Yes	No			Yes			No		No
	Non-Gaussianity	No							No		No
	Stationarity	Yes	No	Yes					No		No
Non-negativity	Source	No		Yes	No		Yes	Yes			Yes
	Mixing process			No			No				No
	Sparsity	No							Yes	No	No
Typical algorithm		FastICA [1, 2]	Parra's joint diagonalization [3]	nICA [11]	SOBI [1, 2]	Infomax [1, 2]	SNICA [12]	BPSS [13]	NMF with sparsity constraint [23]	NMF [15]	To be presented in this dissertation
Application		Wireless comms.	Speech separation & analysis		Wireless comms.		Analytical chemistry		Image analysis & analytical chemistry		

Figure 1.1. An overview of existing algorithms in BSS of instantaneous mixtures.

Chapter 2

nBSS Problem Statement and

Assumptions

The scenario under consideration is that of linear instantaneous mixtures. The signal model is

$$\mathbf{x}[n] = \mathbf{A}\mathbf{s}[n] = \sum_{i=1}^{N} \mathbf{a}_i s_i[n], \qquad n = 1, \ldots, L \tag{2.1}$$

where $\mathbf{s}[n] = [\ s_1[n], \ldots, s_N[n]\ ]^T$ is the input or source vector sequence with N denoting the input dimension (or the number of sources), $\mathbf{x}[n] = [\ x_1[n], \ldots, x_M[n]\ ]^T$ is the output or observation vector sequence with M denoting the output dimension (or the number of observations), $\mathbf{A} = [\ \mathbf{a}_1, \ldots, \mathbf{a}_N\ ] \in \mathbb{R}^{M \times N}$ is the mixing matrix describing the input-output relation, and $L \gg \max\{M, N\}$ is the sequence (or data) length. Note that (2.1) can also be rewritten as

$$\boldsymbol{x}_i = \sum_{j=1}^{N} a_{ij} \boldsymbol{s}_j, \ i = 1, \ldots, M, \tag{2.2}$$

where a_{ij} is the (i, j)th element of $\mathbf{A}$, $\boldsymbol{s}_j = [\ s_j[1], \ldots, s_j[L]\ ]^T$ is a vector representing the jth source signal and $\boldsymbol{x}_i = [\ x_i[1], \ldots, x_i[L]\ ]^T$ is a vector representing the ith

observed signal.

In BSS, the problem is to retrieve the sources $s_1, \ldots, s_N$ and the mixing matrix $\mathbf{A}$ from the observations $x_1, \ldots, x_M$, without any prior knowledge about $s_1, \ldots, s_N$ and $\mathbf{A}$. BSS has shown great potential in various applications [1, 2], and here we describe two examples in biomedical image analysis, and the other in hyperspectral image analysis [9].

Example 1 Magnetic Resonance Imaging (MRI)

Dynamic contrast-enhanced MRI (DCE-MRI) uses various molecular weight contrast agents to assess tumor vasculature perfusion and permeability, and has potential utility in evaluating the efficacy of angiogenesis inhibitors in cancer treatment [8]. While DCE-MRI can provide a meaningful estimation of vasculature permeability when a tumor is homogeneous, many malignant tumors show markedly heterogeneous areas of permeability, and thereby each observed image x_i (which denotes the observed image acquired at the ith time point) often represent a convex mixture of more than one distinct vasculature sources $s_1, \ldots, s_N$ independent of spatial resolution.

The raw DCE-MRI images of breast tumor, for example, are given on the top of Figure 2.1, and its bottom plot illustrates the temporal mixing process of the source patterns where the tumor angiogenic activities $x_1, \ldots, x_M$ represent the weighted summation of spatially-distributed vascular permeability associated with different perfusion rates $s_1, \ldots, s_N$. The BSS methods can be applied to computationally estimate time activity curves $\mathbf{a}_1, \ldots, \mathbf{a}_N$ (each of which represents the mixing coefficients over M time points for one source) and underlying compartment vascular permeability $s_1, \ldots, s_N$ within the tumor site.

Example 2 Dynamic Fluorescent Imaging (DFI)

DFI exploits highly specific and biocompatible fluorescent contrast agents to interro-

8
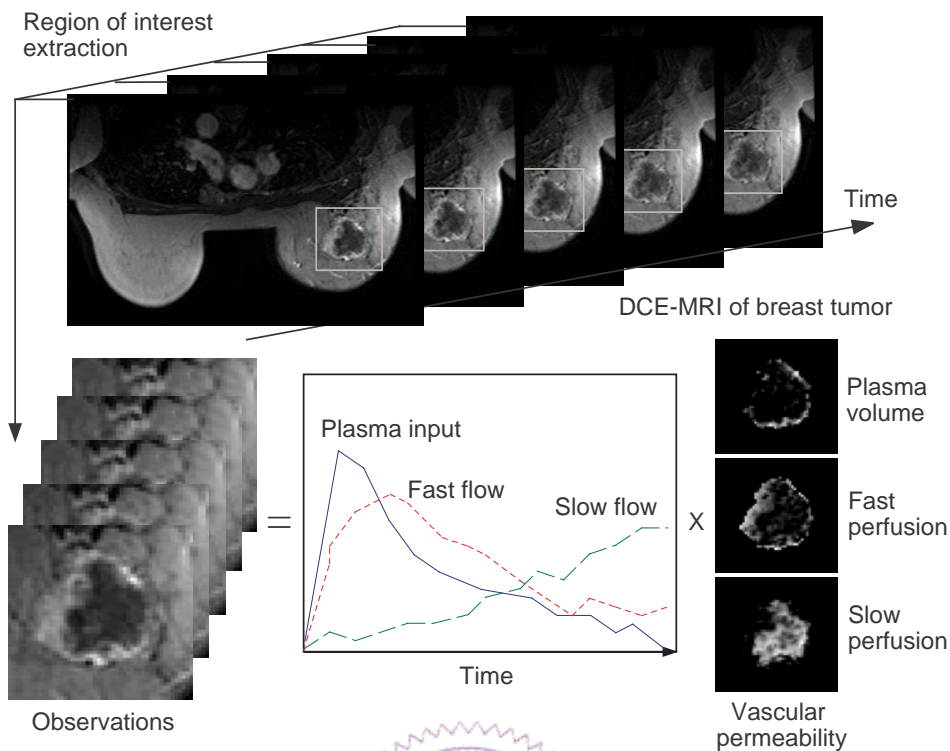
Figure 2.1. The BSS problem in DCE-MRI applications.

gate small animals for drug development and disease research [46]. The DFI technique generates a time series of images acquired after injection of an inert dye, where the dye's differential biodistribution dynamics allow precise delineation and identification of major organs. However, due mainly to the malign effects of light scatter and absorption, spatial resolution and imaging depth are the limitations of planar optical approaches.

The DFI data acquired in a mouse study, for instance, is shown in Figure 2.2, where each DFI image $\boldsymbol{x}_i$ (which represents the observed image acquired at the ith time point) is delineated as a linear mixture of the anatomical maps associated with different organs $\boldsymbol{s}_1, \ldots, \boldsymbol{s}_N$. BSS methods can be used to numerically unmix the observed images into the anatomical maps $\boldsymbol{s}_1, \ldots, \boldsymbol{s}_N$ and their mixing portions $\mathbf{A}$.
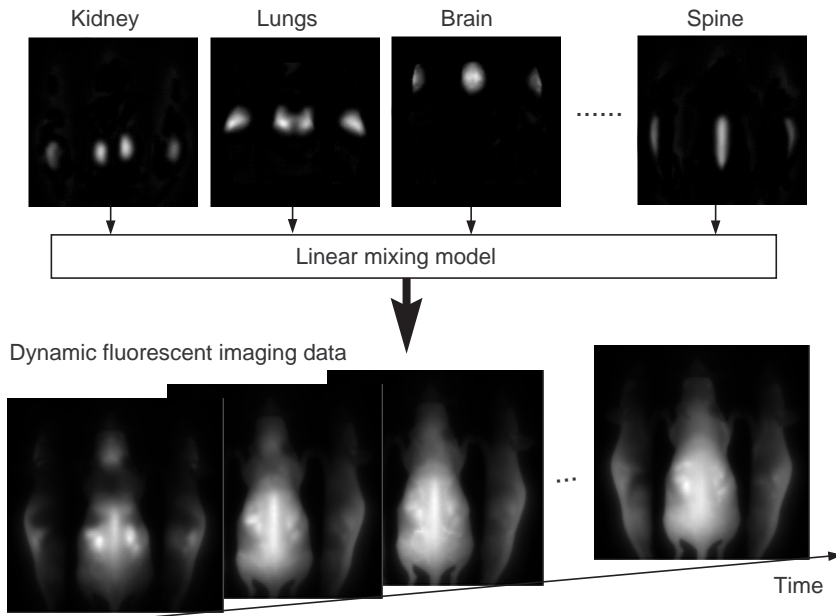
Figure 2.2. The BSS problem in dynamic fluorescent image analysis.

Example 3 Hyperspectral Imaging

Hyperspectral remote sensing exploits the electromagnetic (EM) scattering patterns of distinct materials at specific wavelengths, and measures the scattered portion of the EM spectrum from the visible region through the near-infrared over hundreds of narrow contiguous bands. However, due to low spatial resolution of the hyperspectral sensor used, each pixel of the observed spectra usually comprises multiple spectra from distinct materials (endmember signatures).

Figure 2.3 shows that there are three materials (i.e., soil, water, and vegetation) distributed over the ground surface, and the measured spectrum for each pixel $\mathbf{x}[n]$ is composed of different endmember signatures $\mathbf{a}_1, \ldots, \mathbf{a}_N$ [47]. To analyze the components from which each observed pixel is constituted, the BSS methods can be applied here to unmix each pixel $\mathbf{x}[n]$ into several endmember signatures $\mathbf{a}_1, \ldots, \mathbf{a}_N$ and their mixing proportions $s_1[n], \ldots, s_N[n]$.

Like most nBSS techniques, the proposed frameworks to be presented in this
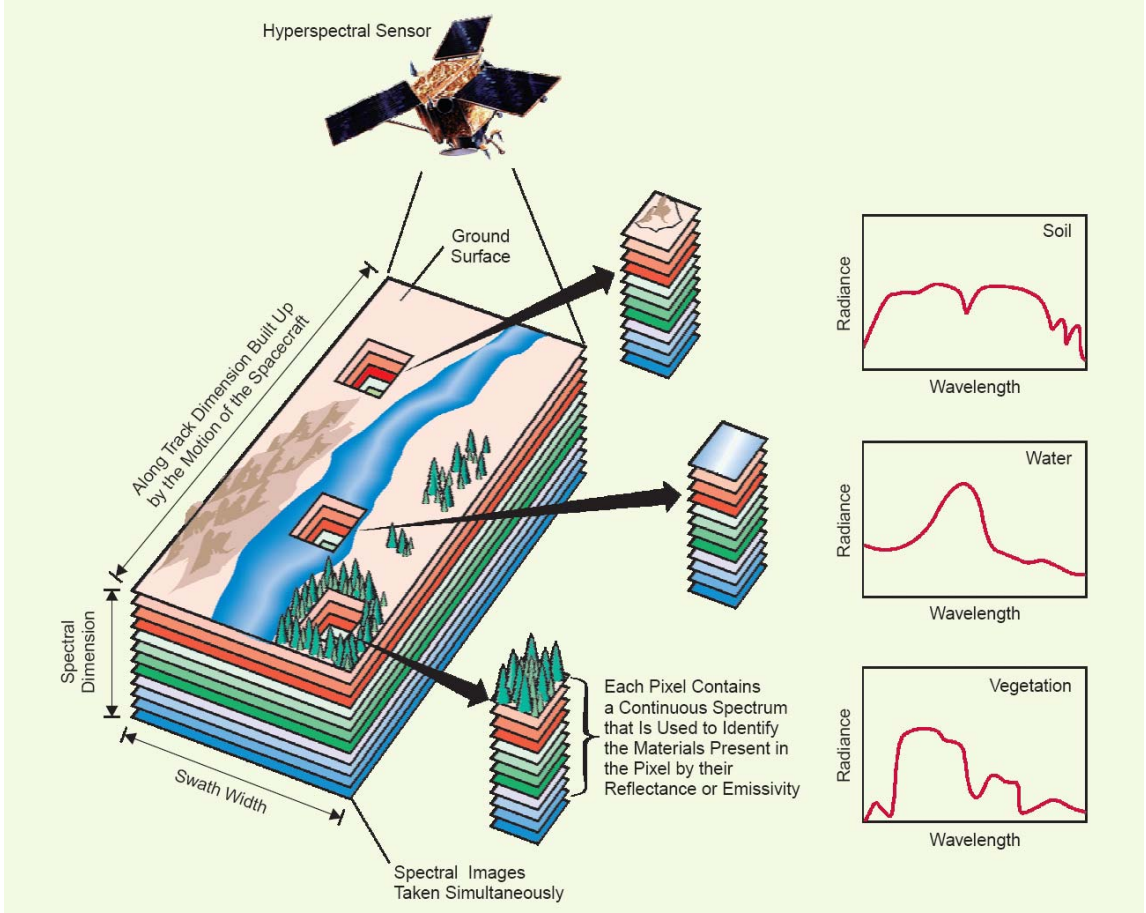
Figure 2.3. The BSS problem in hyperspectral image analysis for remote sensing. Courtesy to G. Shaw and D. Manolakis [47].

dissertation are based on the following assumptions:

(A1) All $\boldsymbol{s}_j$ are componentwise non-negative; i.e., for each j, $\boldsymbol{s}_j \in \mathbb{R}_+^L$.

(A2) $M \geq N$ and $\mathbf{A}$ is of full column rank.

(A3) Each source signal vector is *local dominant*, in the following sense: For each $i \in \{1, \ldots, N\}$, there exists an (unknown) index ℓ_i such that $s_i[\ell_i] > 0$ and $s_j[\ell_i] = 0$, $\forall j \neq i$.

Assumption (A1) is true in image analysis [8, 9], where image intensities are represented by non-negative quantities. Assumption (A2) is rather standard in nBSS. Assumption (A3) may be satisfied when the source signals are sparse (or contain

11

many zeros). In brain MRI, for instance, the non-overlapping region of the spatial distribution of a fast perfusion and a slow perfusion source images [8] can be higher than 95%. For high contrast images such as human portraits, we found that (A3) would also be an appropriate assumption. An illustration of the local dominance assumption is given in Figure 2.4. One can clearly see that the source signals need not be sparse, but spare or high-contrast sources would possibly lead to source local dominance assumption.
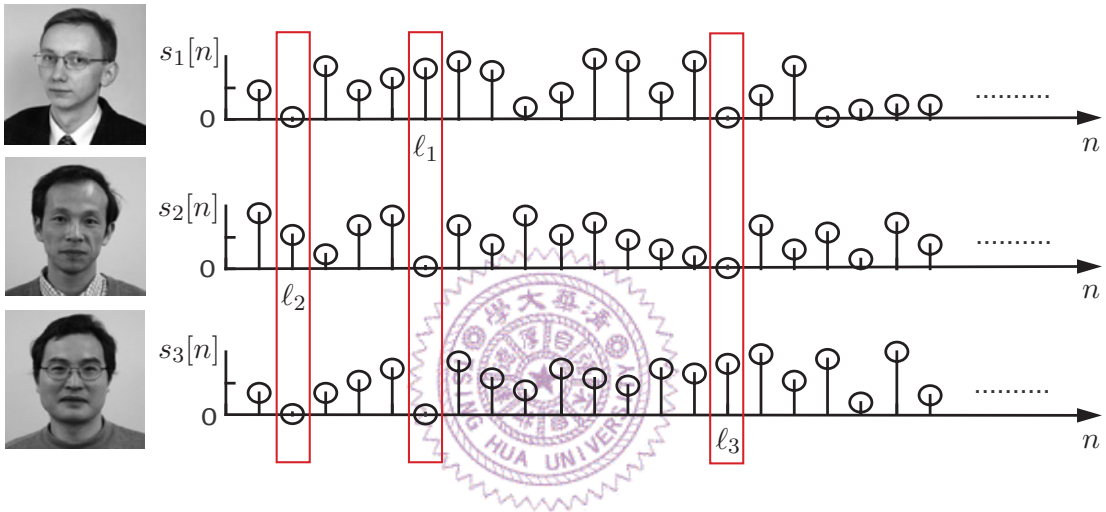
Figure 2.4. Illustration of local dominance assumption for the case of $N = 3$.

(A4) The mixing matrix has unit row sum; i.e., for all $i = 1, \ldots, M$,

$$\sum_{j=1}^{N} a_{ij} = 1. \tag{2.3}$$

(A5) Each source vector sequence has unit sum; i.e., for all $n = 1, \ldots, L$,

$$\sum_{i=1}^{N} s_i[n] = 1. \tag{2.4}$$

Assumptions (A4) and (A5) are essential for development of nBSS methods in Chapter

12

4 and Chapter 5, respectively, though they can be relaxed through a model reformulation [34]. Moreover, in MRI (e.g., in Example 1), (A4) is automatically satisfied due to the so-called partial volume effect [34]. In hyperspectral imaging (e.g., in Example 3), (A5) is intrinsically satisfied due to the full-additivity of source vector sequence.

We now show in the following example that how we can relax (A4):

Example 4 Suppose that (A4) is not satisfied. For simplicity of exposition of the idea, assume non-negative mixing; i.e., $a_{ij} \geq 0$ for all (i, j) (extension to $a_{ij} \in \mathbb{R}$ is possible). Under such circumstances, the observations are all non-negative and we can assume that $\boldsymbol{x}_i^T \mathbf{1}_L \neq 0$ for all $i = 1, \ldots, M$. Likewise, we can assume $\boldsymbol{s}_j^T \mathbf{1}_L \neq 0$ for all j. The idea is to enforce (A4) by normalizing the observation vectors $\boldsymbol{x}_i$ in (2.2):

$$\bar{\boldsymbol{x}}_i \triangleq \frac{\boldsymbol{x}_i}{\boldsymbol{x}_i^T \mathbf{1}_L} = \sum_{j=1}^{N} \left(\frac{a_{ij} \boldsymbol{s}_j^T \mathbf{1}_L}{\boldsymbol{x}_i^T \mathbf{1}_L} \right) \left(\frac{\boldsymbol{s}_j}{\boldsymbol{s}_j^T \mathbf{1}_L} \right). \tag{2.5}$$

By letting $\bar{a}_{ij} = a_{ij} \boldsymbol{s}_j^T \mathbf{1}_L / \boldsymbol{x}_i^T \mathbf{1}_L$ and $\bar{\boldsymbol{s}}_j = \boldsymbol{s}_j / \boldsymbol{s}_j^T \mathbf{1}_L$, we obtain a model $\bar{\boldsymbol{x}}_i = \sum_{j=1}^{N} \bar{a}_{ij} \bar{\boldsymbol{s}}_j$ which has the same form as the original signal model in (2.2). It is easy to show that not only the new mixing matrix, denoted by $\bar{\mathbf{A}} = [\bar{a}_{ij}]_{M \times N}$, has unit row sum [or (A4)], but also the model reformulation (2.5) satisfies (A1) and (A3).

It should also be noted that (2.5) does not damage the rank of the mixing matrix. Specifically, if the original mixing matrix $\mathbf{A}$ satisfies (A2), then the new mixing matrix $\bar{\mathbf{A}}$ also satisfies (A2). To show this, we notice that the relationship of $\mathbf{A}$ and $\bar{\mathbf{A}}$ can be expressed as

$$\bar{\mathbf{A}} = \mathbf{D}_1^{-1} \mathbf{A} \mathbf{D}_2 \tag{2.6}$$

where $\mathbf{D}_1 = \mathrm{diag}(\boldsymbol{x}_1^T \mathbf{1}_L, ..., \boldsymbol{x}_M^T \mathbf{1}_L)$ and $\mathbf{D}_2 = \mathrm{diag}(\boldsymbol{s}_1^T \mathbf{1}_L, ..., \boldsymbol{s}_N^T \mathbf{1}_L)$. Since $\mathbf{D}_1$ and $\mathbf{D}_2$ are of full rank, we have $\mathrm{rank}(\bar{\mathbf{A}}) = \mathrm{rank}(\mathbf{A})$.

Likewise, the following example shows how assumption (A5) can be relaxed using

similar idea as in Example 4:

Example 5 Suppose that (A5) does not hold. Assume that $\mathbf{1}_M^T \mathbf{x}[n] \neq 0$ for all $n = 1, \ldots, L$ and $\mathbf{a}_i^T \mathbf{1}_M \neq 0$ for all $i = 1, \ldots, N$. The idea is to enforce (A5) by normalizing the observation vector sequence $\mathbf{x}[n]$ in (2.1):

$$\bar{\mathbf{x}}[n] \triangleq \frac{\mathbf{x}[n]}{\mathbf{1}_M^T \mathbf{x}[n]} = \sum_{j=1}^{N} \left(\frac{s_i[n]\mathbf{a}_i^T \mathbf{1}_M}{\mathbf{1}_M^T \mathbf{x}[n]} \right) \left(\frac{\mathbf{a}_i}{\mathbf{a}_i^T \mathbf{1}_M} \right). \tag{2.7}$$

By letting $\bar{s}_i[n] = s_i[n]\mathbf{a}_i^T \mathbf{1}_M / \mathbf{1}_M^T \mathbf{x}[n]$ and $\bar{\mathbf{a}}_i = \mathbf{a}_i / \mathbf{a}_i^T \mathbf{1}_M$, we obtain a model $\bar{\mathbf{x}}[n] = \sum_{j=1}^{N} \bar{s}_i[n]\bar{\mathbf{a}}_i$ which has the same form as the original signal model in (2.1). It is easy to show that the new source vector sequence, denoted by $\bar{\mathbf{s}}[n] = [\ \bar{s}_1[n], \ldots, \bar{s}_N[n]\ ]^T$, has unit sum [or (A5)], and the model reformulation (2.7) also satisfies (A1) and (A3).

To show that the model reformulation (2.7) satisfies (A2), we notice that the relationship of $\mathbf{A}$ and $\bar{\mathbf{A}}$ can be expressed as

$$\bar{\mathbf{A}} = \mathbf{A}\mathbf{D}_3, \tag{2.8}$$

where $\mathbf{D}_3 = \mathrm{diag}(\mathbf{a}_1^T \mathbf{1}_M, \ldots, \mathbf{a}_N^T \mathbf{1}_M)$. Since $\mathbf{D}_3$ is of full rank, we get $\mathrm{rank}(\bar{\mathbf{A}}) = \mathrm{rank}(\mathbf{A})$.

Chapter 3

Review of Some Basic Concepts in Convex Analysis

We analyze the geometric structures of the signal model by utilizing some fundamental convex analysis concepts, namely affine hull, convex hull, and their properties. As we will see in next two Chapters, such a convex analysis will shed light into how we can separate the sources. Here we provide a review of some essential concepts. Readers who are interested in further details of convex analysis are referred to the literature such as [48], [49], [50].

3.1   Affine Hull

Given a set of vectors $\{s_1, \ldots, s_N\} \subset \mathbb{R}^L$, the *affine hull* is defined as

$$\mathrm{aff}\{s_1, \ldots, s_N\} = \left\{ \, x = \sum_{i=1}^{N} \theta_i s_i \,\, \middle| \,\, \theta \in \mathbb{R}^N, \sum_{i=1}^{N} \theta_i = 1 \, \right\}. \qquad (3.1)$$

Some examples of affine hulls are illustrated in Figure 3.1. We see that for $N = 2$, an affine hull is a line passing through s_1 and s_2; and for $N = 3$, it is a plane passing

through s_1, s_2, and s_3.
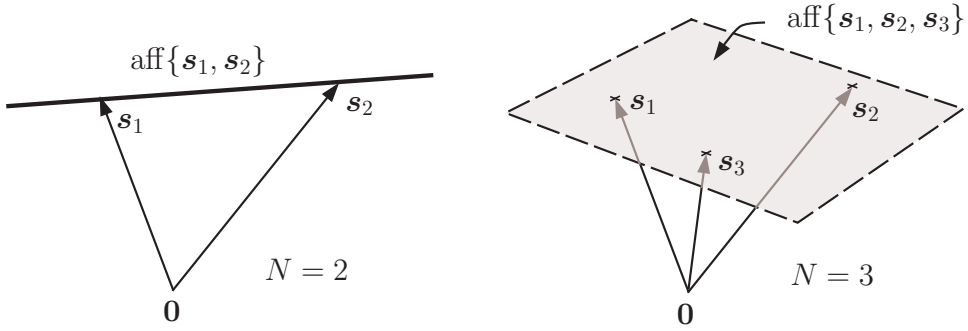
Figure 3.1. Examples of affine hulls for $N = 2$ and $N = 3$.

An affine hull can always be represented by

$$\text{aff}\{s_1, \ldots, s_N\} = \{\, x = \mathbf{C}\alpha + \mathbf{d} \mid \alpha \in \mathbb{R}^P \,\} \tag{3.2}$$

for some $\mathbf{d} \in \mathbb{R}^L$ (non-unique), for some full column rank $\mathbf{C} \in \mathbb{R}^{L \times P}$ (also non-unique), and for some $P \geq 1$. To understand this, consider a simple example where $\{s_1, \ldots, s_N\}$ is linearly independent. One can verify that (3.1) can be rewritten as (3.2), with

$$\mathbf{d} = s_N, \quad \mathbf{C} = [\, s_1 - s_N, s_2 - s_N, \ldots, s_{N-1} - s_N \,],$$

$$P = N - 1, \quad \alpha = [\, \theta_1, \ldots, \theta_{N-1} \,]^T.$$

The integer P in (3.2) is called the *affine dimension*, which characterizes the effective dimension of the affine hull. The affine dimension must satisfy $P \leq N - 1$. Moreover,

Property 1 *If $\{s_1, \ldots, s_N\}$ is an affinely independent set (which means that $\{s_1 - s_N, \ldots, s_{N-1} - s_N\}$ is linearly independent), then the affine dimension is maximal; i.e., $P = N - 1$.*

16

3.2 Convex Hull

Given a set of vectors $\{s_1, \ldots, s_N\} \subset \mathbb{R}^L$, the *convex hull* is defined as

$$\text{conv}\{s_1, \ldots, s_N\} = \left\{ x = \sum_{i=1}^N \theta_i s_i \ \middle| \ \theta \in \mathbb{R}_+^N, \sum_{i=1}^N \theta_i = 1 \right\}. \tag{3.3}$$

A convex hull would be a line segment for $N = 2$, a triangle for $N = 3$. This is illustrated in Figure 3.2.
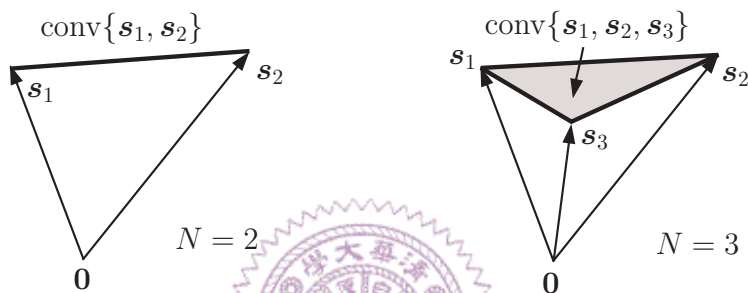
Figure 3.2. Examples of convex hulls for $N = 2$ and $N = 3$.

An important concept related to convex hull is *extreme points*, also known as *vertices*. From a geometric perspective, extreme points are the 'corner points' of the convex hull. A point $x \in \text{conv}\{s_1, \ldots, s_N\}$ is said to be an extreme point of $\text{conv}\{s_1, \ldots, s_N\}$ if x can never be a non-trivial convex combination of $s_1, \ldots, s_N$; i.e.,

$$x \neq \sum_{i=1}^N \theta_i s_i \tag{3.4}$$

for all $\theta \in \mathbb{R}_+^N$, $\sum_{i=1}^N \theta_i = 1$, and $\theta \neq e_i$ for any i. Some basic properties about extreme points are as follows:

Property 2 *The set of extreme points of $\text{conv}\{s_1, \ldots, s_N\}$ must be either the full set or a subset of $\{s_1, \ldots, s_N\}$.*

Property 3 *If $\{s_1, \ldots, s_N\}$ is affinely independent, then the set of extreme points of* conv$\{s_1, \ldots, s_N\}$ *is exactly* $\{s_1, \ldots, s_N\}$.

For example, in the illustrations in Figure 3.2 the extreme points are the 'corner' points $\{s_1, \ldots, s_N\}$.

A special, but representative case of convex hull is *simplex*. A convex hull is called a simplex if $L = N - 1$ and $\{s_1, \ldots, s_N\}$ is affinely independent. It follows that

Property 4 *The set of extreme points of a simplex* conv$\{s_1, \ldots, s_N\} \subset \mathbb{R}^{N-1}$ *is* $\{s_1, \ldots, s_N\}$.

In other words, a simplex on $\mathbb{R}^{N-1}$ is a convex hull with exactly N extreme points. A simplex for $N = 2$ is a line segment on $\mathbb{R}$, while a simplex for $N = 3$ is a triangle on $\mathbb{R}^2$.

18

Chapter 4

Convex Analysis of Mixtures of Non-negative Sources

In this chapter, we will first introduce the new nBSS criterion via CAMNS and its profound implications that perfect blind separation can be achieved by finding all the extreme points of an observation-constructed polyhedral set. We then develop two extreme point finding algorithms for fulfilling CAMNS criterion, using a systematic LP approach and a heuristic alternating volume maximization approach, respectively. We finally carry out some simulations and real data experiments to evaluate the performance of the proposed CAMNS-based nBSS methods and some existing nBSS methods. Throughout this chapter, we will focus on the signal model (2.2) and assume that

(A1) All the elements of $\boldsymbol{s}_j$ are non-negative, i.e., $\boldsymbol{s}_j \in \mathbb{R}_+^L$ for all $j = 1, \ldots, N$.

(A2) $M \geq N$ and $\mathbf{A}$ is of full column rank.

(A3) (Source local dominance) For each $i \in \{1, \ldots, N\}$, there exists an (unknown) index ℓ_i such that $s_i[\ell_i] > 0$ and $s_j[\ell_i] = 0$, $\forall j \neq i$.

(A4) Sum of each row of $\mathbf{A}$ is unity, i.e., $\sum_{j=1}^{N} a_{ij} = 1$ for all $i = 1, \ldots, M$.

are satisfied. Before getting into the details of CAMNS, Figure 4.1 shows some diagrams to give an outline of how CAMNS works.
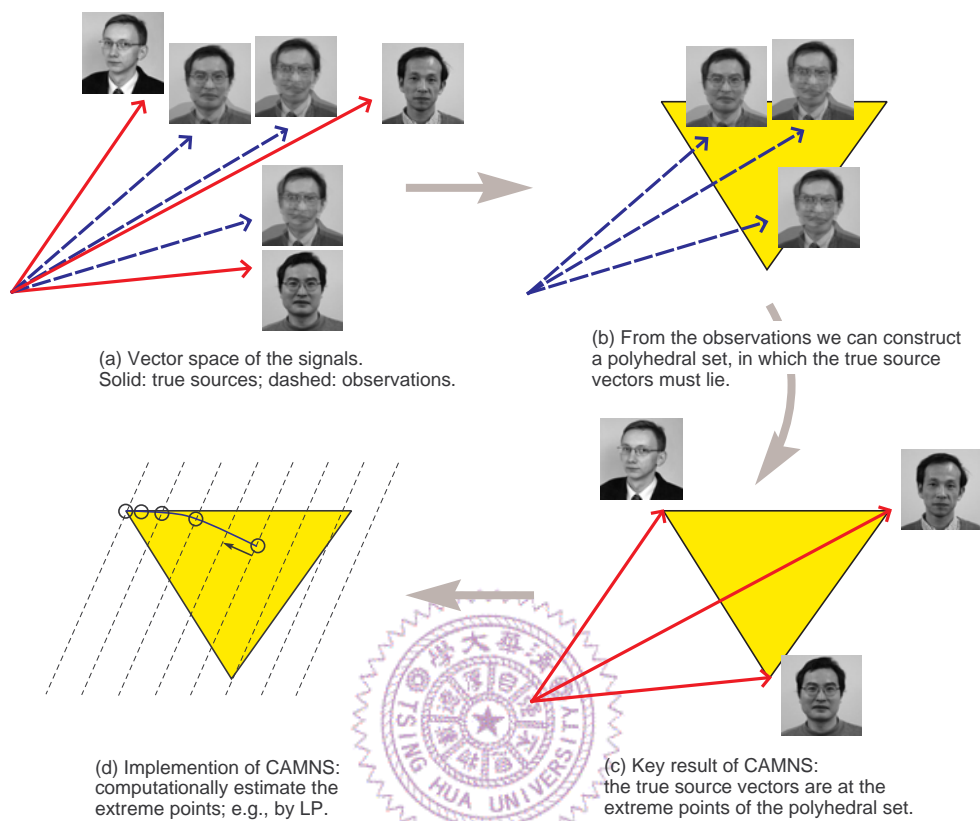
Figure 4.1. An intuitive illustration of how CAMNS operates.

4.1 nBSS Criterion via CAMNS

Applying convex analysis to the nBSS problem in (2.2) under (A1)-(A4) will lead to an nBSS criterion that guarantees perfect source separation.

4.1.1 Convex Analysis of the Problem, and the CAMNS Criterion

Recall from (2.2) that the signal model is given by

$$\boldsymbol{x}_i = \sum_{j=1}^{N} a_{ij} \boldsymbol{s}_j, \ i = 1, \ldots, M.$$

Since $\sum_{j=1}^{N} a_{ij} = 1$ [(A4)], every $\boldsymbol{x}_i$ is indeed an affine combination of $\{\boldsymbol{s}_1, \ldots, \boldsymbol{s}_N\}$:

$$\boldsymbol{x}_i \in \mathrm{aff}\{\boldsymbol{s}_1, \ldots, \boldsymbol{s}_N\} \tag{4.1}$$

for any $i = 1, \ldots, M$. Hence an interesting question is the following: Can we use the observations $\boldsymbol{x}_1, \ldots, \boldsymbol{x}_M$ to construct the source affine hull $\mathrm{aff}\{\boldsymbol{s}_1, \ldots, \boldsymbol{s}_N\}$?

To answer the question above, let us first consider the following lemma:

Lemma 1 *The observation affine hull is identical to the source affine hull; that is,*

$$\mathrm{aff}\{\boldsymbol{s}_1, \ldots, \boldsymbol{s}_N\} = \mathrm{aff}\{\boldsymbol{x}_1, \ldots, \boldsymbol{x}_M\}. \tag{4.2}$$

The proof of Lemma 1 is given in Appendix A.1. An illustration is shown in Figure 4.2(a) to pictorially demonstrate the affine hull equivalence in Lemma 1.

Thus, by constructing the observation affine hull, the source affine hull can be obtained. Using the affine representation of an affine hull, $\mathrm{aff}\{\boldsymbol{s}_1, \ldots, \boldsymbol{s}_N\}$ (or $\mathrm{aff}\{\boldsymbol{x}_1, \ldots, \boldsymbol{x}_M\}$) can be characterized as

$$\mathrm{aff}\{\boldsymbol{s}_1, \ldots, \boldsymbol{s}_N\} = \left\{\ \boldsymbol{x} = \mathbf{C}\boldsymbol{\alpha} + \mathbf{d} \ \middle|\ \boldsymbol{\alpha} \in \mathbb{R}^P\ \right\} \tag{4.3}$$

for some $(\mathbf{C}, \mathbf{d}) \in \mathbb{R}^{L \times P} \times \mathbb{R}^L$ such that $\mathrm{rank}(\mathbf{C}) = P$, with P being the affine dimension. From (A3) it can be shown that (see Appendix A.2)
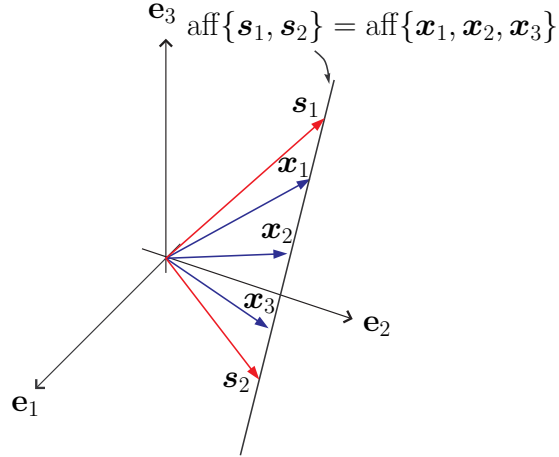
Figure 4.2. A geometric illustration of the affine hull equivalence in Lemma 1, for the case of $N = 2$, $M = 3$, and $L = 3$.

Lemma 2 *The set of source vectors* $\{s_1, \ldots, s_N\}$ *is linearly independent.*

Hence, by Property 1 the affine dimension of $\text{aff}\{s_1, \ldots, s_N\}$ is maximal; i.e., $P = N - 1$. For the special case of $M = N$ (the number of inputs being equal to the number of outputs), it is easy to obtain $(\mathbf{C}, \mathbf{d})$ from the observations $x_1, \ldots, x_M$; see the review in Chapter 3.

For $M \geq N$, a method called *affine set fitting* would be required. Since $(\mathbf{C}, \mathbf{d})$ is non-unique, without loss of generality one can restrict $\mathbf{C}^T \mathbf{C} = \mathbf{I}_{N-1}$ (semi-unitary matrix). The following affine set fitting problem is used to find $(\mathbf{C}, \mathbf{d})$

$$(\mathbf{C}, \mathbf{d}) = \arg \min_{\substack{\tilde{\mathbf{C}}, \tilde{\mathbf{d}} \\ \tilde{\mathbf{C}}^T \tilde{\mathbf{C}} = \mathbf{I}_{N-1}}} \sum_{i=1}^{M} e_{\mathcal{A}(\tilde{\mathbf{C}}, \tilde{\mathbf{d}})}(x_i) \tag{4.4}$$

where $e_{\mathcal{A}}(x)$ is the projection error of x onto $\mathcal{A}$, defined as

$$e_{\mathcal{A}}(x) = \min_{\tilde{x} \in \mathcal{A}} \|x - \tilde{x}\|_2^2, \tag{4.5}$$

and

$$\mathcal{A}(\tilde{\mathbf{C}}, \tilde{\mathbf{d}}) = \{\tilde{x} = \tilde{\mathbf{C}}\alpha + \tilde{\mathbf{d}} \mid \alpha \in \mathbb{R}^{N-1}\} \tag{4.6}$$

22

is an affine set parameterized by $(\tilde{\mathbf{C}}, \tilde{\mathbf{d}})$. The objective of (4.4) is to find an $(N-1)$-dimensional affine set that has the minimum projection error with respect to the observations (which is zero for the noise-free case). Problem (4.4) is shown to have a closed-form solution:

Proposition 1 *A solution to the affine set fitting problem in (4.4) is*

$$\mathbf{d} = \frac{1}{M} \sum_{i=1}^{M} \boldsymbol{x}_i \tag{4.7}$$

$$\mathbf{C} = [\ \boldsymbol{q}_1(\mathbf{UU}^T), \boldsymbol{q}_2(\mathbf{UU}^T), \dots, \boldsymbol{q}_{N-1}(\mathbf{UU}^T)\ ] \tag{4.8}$$

where $\mathbf{U} = [\ \boldsymbol{x}_1 - \mathbf{d}, \dots, \boldsymbol{x}_M - \mathbf{d}\ ] \in \mathbb{R}^{L \times M}$, *and the notation* $\boldsymbol{q}_i(\mathbf{R})$ *denotes the eigenvector associated with the ith principal eigenvalue of the input matrix* $\mathbf{R}$.

The proof of the above proposition is given in Appendix A.3. We should stress that this affine set fitting provides a best affine set in terms of minimizing the projection error. Hence, in the presence of additive noise, it has an additional advantage of noise mitigation for $M > N$.

Let us emphasize that we are dealing with non-negative sources. Hence, any source vector $\boldsymbol{s}_i$ must lie in

$$\mathcal{S} \triangleq \mathrm{aff}\{\boldsymbol{s}_1, \dots, \boldsymbol{s}_N\} \cap \mathbb{R}_+^L$$
$$= \mathcal{A}(\mathbf{C}, \mathbf{d}) \cap \mathbb{R}_+^L$$
$$= \{\boldsymbol{x} \mid \boldsymbol{x} = \mathbf{C}\boldsymbol{\alpha} + \mathbf{d},\ \boldsymbol{x} \succeq \mathbf{0},\ \boldsymbol{\alpha} \in \mathbb{R}^{N-1}\}, \tag{4.9}$$

which is a polyhedral set and can be constructed by observations, i.e., $\mathbf{C}$ and $\mathbf{d}$ in Proposition 1. The following lemma (with the proof given in Appendix A.4) plays an important role:

Lemma 3 *The polyhedral set $\mathcal{S}$ is identical to the source convex hull; that is,*

$$\mathcal{S} = \mathrm{conv}\{\boldsymbol{s}_1, \ldots, \boldsymbol{s}_N\}. \tag{4.10}$$

Following the illustration in Figure 4.2, in Figure 4.3 we geometrically demonstrate the equivalence of $\mathcal{S}$ and $\mathrm{conv}\{\boldsymbol{s}_1, \ldots, \boldsymbol{s}_N\}$. This surprising result is due mainly to the local dominance [A3].
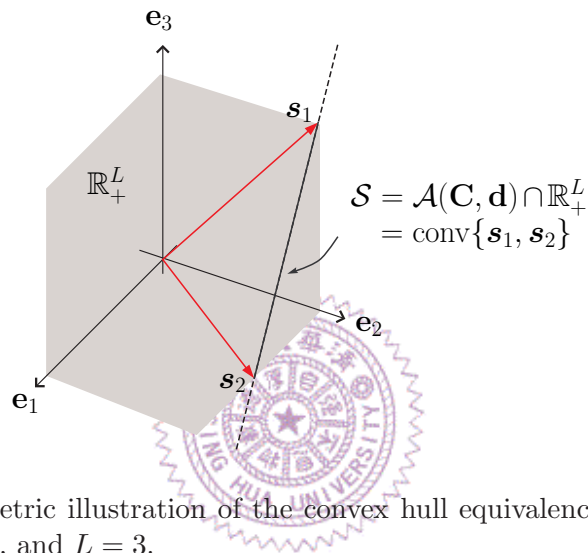
Figure 4.3. A geometric illustration of the convex hull equivalence in Lemma 3, for the case of $N = 2$, $M = 3$, and $L = 3$.

Furthermore, we can deduce from Lemma 2 and Property 3 that

Lemma 4 *The set of extreme points of $\mathrm{conv}\{\boldsymbol{s}_1, \ldots, \boldsymbol{s}_N\}$ is $\{\boldsymbol{s}_1, \ldots, \boldsymbol{s}_N\}$.*

Summarizing all the results above, we establish an nBSS criterion as follows:

Criterion 1 *Use the affine set fitting solution in Proposition 1 to compute* $(\mathbf{C}, \mathbf{d})$. *Then, find all the extreme points of the polyhedral set*

$$\mathcal{S} = \left\{ \boldsymbol{x} \in \mathbb{R}^L \;\middle|\; \boldsymbol{x} = \mathbf{C}\boldsymbol{\alpha} + \mathbf{d} \succeq \mathbf{0}, \; \boldsymbol{\alpha} \in \mathbb{R}^{N-1} \right\} \tag{4.11}$$

and denote the obtained set of extreme points by $\{\hat{\boldsymbol{s}}_1, \ldots, \hat{\boldsymbol{s}}_N\}$. *Output* $\{\hat{\boldsymbol{s}}_1, \ldots, \hat{\boldsymbol{s}}_N\}$ *as the set of estimated source vectors.*

It follows from the above development that

Theorem 1 *The solution to Criterion 1 is uniquely given by the set of true source vectors* $\{\boldsymbol{s}_1, \ldots, \boldsymbol{s}_N\}$, *under the premises in* (A1) *to* (A4).

The implication of Theorem 1 is profound. It suggests that the true source vectors can be perfectly identified by finding all the extreme points of $\mathcal{S}$. To our best knowledge, this convex analysis based nBSS criterion cannot be found in any presently available literature and is highly expected to provide a new avenue to nBSS.

In the next subsection we will describe a systematic LP-based method for efficiently realizing Criterion 1.

4.1.2 Alternative Form of the CAMNS Criterion

There is an alternative form to the CAMNS criterion (Criterion 1). The alternative form is useful for deriving simple CAMNS algorithms in some special cases. It will also shed light into the volume maximization heuristics considered later in this chapter.

Consider the pre-image of the observation-constructed polyhedral set $\mathcal{S}$, under the

mapping $\boldsymbol{s} = \mathbf{C}\boldsymbol{\alpha} + \mathbf{d}$:

$$\mathcal{F} = \left\{ \boldsymbol{\alpha} \in \mathbb{R}^{N-1} \mid \mathbf{C}\boldsymbol{\alpha} + \mathbf{d} \succeq \mathbf{0} \right\}$$
$$= \left\{ \boldsymbol{\alpha} \in \mathbb{R}^{N-1} \mid \mathbf{c}_n^T \boldsymbol{\alpha} + d_n \geq 0, \ n = 1, \ldots, L \right\} \tag{4.12}$$

where $\mathbf{c}_n^T$ is the nth row of $\mathbf{C}$. There is a direct correspondence between the extreme points of $\mathcal{S}$ and $\mathcal{F}$:

Lemma 5 *The polyhedral set $\mathcal{F}$ in (4.12) is equivalent to a simplex*

$$\mathcal{F} = \mathrm{conv}\{\boldsymbol{\alpha}_1, \ldots, \boldsymbol{\alpha}_N\} \tag{4.13}$$

where each $\boldsymbol{\alpha}_i \in \mathbb{R}^{N-1}$ satisfies

$$\mathbf{C}\boldsymbol{\alpha}_i + \mathbf{d} = \boldsymbol{s}_i. \tag{4.14}$$

The proof of Lemma 5 is given in Appendix A.5. Since the set of extreme points of a simplex $\mathrm{conv}\{\boldsymbol{\alpha}_1, \ldots, \boldsymbol{\alpha}_N\}$ is $\{\boldsymbol{\alpha}_1, \ldots, \boldsymbol{\alpha}_N\}$ (Property 4 in Chapter 3), we have the following alternative nBSS criterion:

Criterion 2 (Alternative form of Criterion 1) *Use the affine set fitting solution in Proposition 1 to compute* $(\mathbf{C}, \mathbf{d})$. *Then, find all the extreme points of the simplex*

$$\mathcal{F} = \left\{ \boldsymbol{\alpha} \in \mathbb{R}^{N-1} \mid \mathbf{C}\boldsymbol{\alpha} + \mathbf{d} \succeq \mathbf{0} \right\} \tag{4.15}$$

and denote the obtained set of extreme points by $\{\hat{\boldsymbol{\alpha}}_1, \ldots, \hat{\boldsymbol{\alpha}}_N\}$. *Output*

$$\hat{s}_i = \mathbf{C}\hat{\boldsymbol{\alpha}}_i + \mathbf{d}, \; i = 1, \ldots, N \tag{4.16}$$

as the set of estimated source vectors.

It follows directly from Theorem 1 and Lemma 5 that

Theorem 2 *The solution to Criterion 2 is uniquely given by the set of true source vectors* $\{\boldsymbol{s}_1, \ldots, \boldsymbol{s}_N\}$, *under the premises in* (A1) *to* (A4).

Based on Criterion 2, a simple nBSS algorithm for the two-source case is as follows:

Example 6 For $N = 2$, the simplex $\mathcal{F}$ is a line segment on $\mathbb{R}$. Hence, by locating the two endpoints of the line segment, the extreme points will be found. To see how this can be done, let us examine $\mathcal{F}$ (in polyhedral form)

$$\mathcal{F} = \{\alpha \in \mathbb{R} \mid c_n\alpha + d_n \geq 0, \; n = 1, ..., L\}. \tag{4.17}$$

From (4.17) we see that $\alpha \in \mathcal{F}$ implies the following two conditions:

$$\alpha \geq -d_n/c_n, \text{ for all } n \text{ such that } c_n > 0, \tag{4.18}$$

$$\alpha \leq -d_n/c_n, \text{ for all } n \text{ such that } c_n < 0. \tag{4.19}$$

We therefore conclude from (4.18) and (4.19) that the extreme points are given by

$$\alpha_1 = \max\{-d_n/c_n \mid c_n > 0, \ n = 1, 2, ..., L\}, \qquad (4.20)$$

$$\alpha_2 = \min\{-d_n/c_n \mid c_n < 0, \ n = 1, 2, ..., L\}. \qquad (4.21)$$

Thus, for two sources, CAMNS blind source separation reduces to a simple closed-form solution.

4.2 Systematic Linear Programming Method for CAMNS

This section and the next section are dedicated to the practical implementations of CAMNS. In this section, we propose an approach that uses linear programs (LPs) to systematically fulfil Criterion 1. An appealing characteristic of this CAMNS-LP method is that though Criterion 1 does not appear to be related to convex optimization at first look, yet it can be exactly solved by CAMNS-LP as long as the assumptions (A1)-(A4) are true.

Our problem as specified in Criterion 1 is to find all the extreme points of the polyhedral set $\mathcal{S}$ in (4.9). In the optimization literature this problem is known as vertex enumeration; see in the literature [51, 52, 53] and the references therein. The available extreme-point finding methods are sophisticated, requiring no assumption on the extreme points. However, the complexity of those methods would increase exponentially with the number of inequalities, which is L by (4.11) (note that L is the data length in our problem and is often large in practice). The notable difference of our innovative algorithm here is that we exploit the the linear independence characteristic of the extreme points $\boldsymbol{s}_1, ..., \boldsymbol{s}_N$ (Lemma 2). By doing so we will establish an extreme-point finding method (for CAMNS) whose complexity is polynomial in L.

Our approach is to identify one extreme point at one time. Consider the following linear minimization problem:

$$p^\star = \min_{s} \quad \mathbf{r}^T \boldsymbol{s}$$

$$\text{subject to (s.t.)} \quad \boldsymbol{s} \in \mathcal{S} \tag{4.22}$$

for some arbitrarily chosen direction $\mathbf{r} \in \mathbb{R}^L$, where $p^\star$ denotes the optimal objective value of (4.22). By the polyhedral representation of $\mathcal{S}$ in (4.9), problem (4.22) can be equivalently represented by an LP

$$p^\star = \min_{\boldsymbol{\alpha}} \quad \mathbf{r}^T(\mathbf{C}\boldsymbol{\alpha} + \mathbf{d})$$

$$\text{s.t.} \quad \mathbf{C}\boldsymbol{\alpha} + \mathbf{d} \succeq \mathbf{0} \tag{4.23}$$

which can be solved by readily available algorithms such as the polynomial-time interior-point methods [54, 55]. Problem (4.23) is the problem we solve in practice, but (4.22) is analogous to extreme-point search.

A fundamental result in LP theory is that $\mathbf{r}^T\boldsymbol{s}$, the objective function of (4.22), attains the minimum at a point of the boundary of $\mathcal{S}$. To provide more insights, some geometric illustrations are given in Figure 4.4. We can see that the solution of (4.22) may be uniquely given by one of the extreme points $\boldsymbol{s}_i$ [Figure 4.4(a)], or it may be any point on a face [Figure 4.4(b)]. The latter case poses a trouble to our task of identifying $\boldsymbol{s}_i$, but it is arguably not a usual situation. For instance, in the illustration in Figure 4.4(b), $\mathbf{r}$ must be normal to $\boldsymbol{s}_2 - \boldsymbol{s}_3$ which may be unlikely to happen for a randomly picked $\mathbf{r}$. With this intuition in mind, we can prove the following lemma:

Lemma 6 *Suppose that* $\mathbf{r}$ *is randomly generated following a distribution* $\mathcal{N}(\mathbf{0}, \mathbf{I}_L)$. *Then, with probability 1, the solution of (4.22) is uniquely given by* $\boldsymbol{s}_i$ *for some* $i \in \{1, ..., N\}$.

The proof of Lemma 6 is given in Appendix A.6. The idea behind the proof is
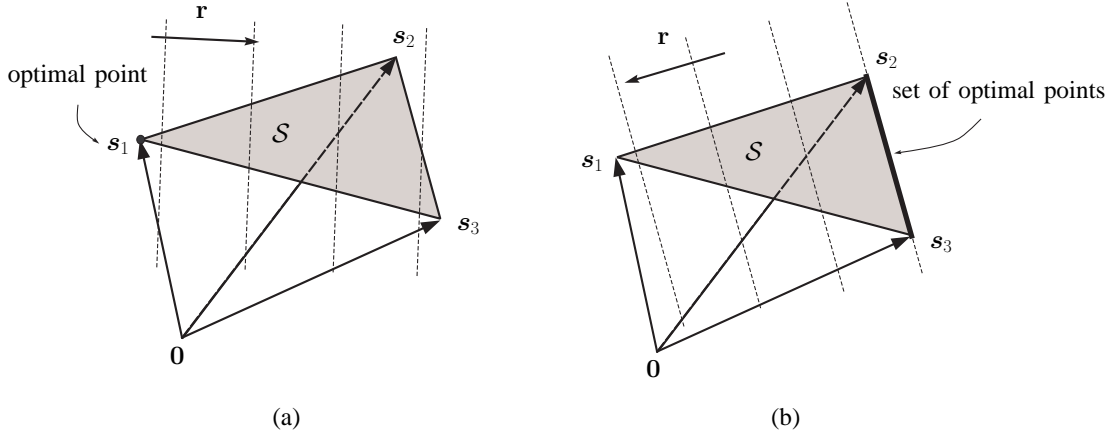
Figure 4.4. Geometric interpretation of an LP.

that undesired cases, such as that in Figure 4.4(b) happen with probability zero.

We may find another extreme point by solving the maximization counterpart of (4.22)

$$
\begin{aligned}
q^{\star} = \max_{\boldsymbol{\alpha}} \quad & \mathbf{r}^{T}(\mathbf{C}\boldsymbol{\alpha} + \mathbf{d}) \\
\text{s.t.} \quad & \mathbf{C}\boldsymbol{\alpha} + \mathbf{d} \succeq \mathbf{0}.
\end{aligned}
\tag{4.24}
$$

Using the same derivations as above, we can show the following: Under the premise of Lemma 6, the solution of (4.24) is, with probability 1, uniquely given by an extreme point $\boldsymbol{s}_i$ different from that in (4.22).

Suppose that we have identified l extreme points, say, without loss of generality, $\{\boldsymbol{s}_1, ..., \boldsymbol{s}_l\}$. Our interest is to refine the above LP extreme-point finding procedure such that the search space is restricted to $\{\boldsymbol{s}_{l+1}, ..., \boldsymbol{s}_N\}$. To do so, consider a thin QR decomposition [56] of $[\boldsymbol{s}_1, ..., \boldsymbol{s}_l]$

$$
[\boldsymbol{s}_1, ..., \boldsymbol{s}_l] = \mathbf{Q}_1 \mathbf{R}_1,
\tag{4.25}
$$

where $\mathbf{Q}_1 \in \mathbb{R}^{L \times l}$ is semi-unitary and $\mathbf{R}_1 \in \mathbb{R}^{l \times l}$ is upper triangular. Let

$$\mathbf{B} = \mathbf{I}_L - \mathbf{Q}_1 \mathbf{Q}_1^T. \tag{4.26}$$

We assume that $\mathbf{r}$ takes the form

$$\mathbf{r} = \mathbf{B}\boldsymbol{w} \tag{4.27}$$

for some $\boldsymbol{w} \in \mathbb{R}^L$, and consider solving (4.23) and (4.24) with such an $\mathbf{r}$. Since $\mathbf{r}$ is orthogonal to the old extreme points $\boldsymbol{s}_1, ..., \boldsymbol{s}_l$, the intuitive expectation is that (4.23) and (4.24) should both lead to new extreme points. Interestingly, we found theoretically that such an expectation is not true, but close. It can be shown that (see Appendix A.7)

Lemma 7 *Suppose that* $\mathbf{r} = \mathbf{B}\boldsymbol{w}$, *where* $\mathbf{B} \in \mathbb{R}^{L \times L}$ *is given by (4.26) and* $\boldsymbol{w}$ *is randomly generated following a distribution* $\mathcal{N}(\mathbf{0}, \mathbf{I}_L)$. *Then, with probability 1, at least one of the optimal solutions of (4.23) and (4.24) is a new extreme point; i.e.,* $\boldsymbol{s}_i$ *for some* $i \in \{l+1, ..., N\}$. *The certificate of finding new extreme points is indicated by* $|p^\star| \neq 0$ *for the case of (4.23), and* $|q^\star| \neq 0$ *for (4.24).*

By repeating the above described procedures, we can identify all the extreme points $\boldsymbol{s}_1, ..., \boldsymbol{s}_N$. The resultant CAMNS-LP method is summarized in Table 4.1.

The CAMNS-LP method in Table 4.1 is not only systematically straightforward to apply, but also efficient due to the maturity of convex optimization algorithms. Using a primal-dual interior-point method, each LP problem [or the problem in (4.22) or (4.24)] can be solved with a worst-case complexity of $\mathcal{O}(L^{0.5}(L(N-1)+(N-1)^3)) \simeq \mathcal{O}(L^{1.5}(N-1))$ for $L \gg N$ [55]. Since the algorithm solves $2(N-1)$ LP problems in the worst case, we infer that its worst-case complexity is $\mathcal{O}(L^{1.5}(N-1)^2)$.

Table 4.1. A summary of the CAMNS-LP method.

Given an affine set characterization 2-tuple $(\mathbf{C}, \mathbf{d})$.

Step 1. Set $l = 0$, and $\mathbf{B} = \mathbf{I}_L$.

Step 2. Randomly generate a vector $\boldsymbol{w} \sim \mathcal{N}(\mathbf{0}, \mathbf{I}_L)$, and set $\mathbf{r} := \mathbf{B}\boldsymbol{w}$.

Step 3. Solve the LPs

$$p^\star = \min_{\boldsymbol{\alpha}} \quad \mathbf{r}^T(\mathbf{C}\boldsymbol{\alpha} + \mathbf{d})$$
$$\text{s.t.} \quad \mathbf{C}\boldsymbol{\alpha} + \mathbf{d} \succeq \mathbf{0}$$

$$q^\star = \max_{\boldsymbol{\alpha}} \quad \mathbf{r}^T(\mathbf{C}\boldsymbol{\alpha} + \mathbf{d})$$
$$\text{s.t.} \quad \mathbf{C}\boldsymbol{\alpha} + \mathbf{d} \succeq \mathbf{0}$$

and obtain their optimal solutions, denoted by $\boldsymbol{\alpha}_1^\star$ and $\boldsymbol{\alpha}_2^\star$, respectively.

Step 4. If $l = 0$

$$\hat{\mathbf{S}} = [\ \mathbf{C}\boldsymbol{\alpha}_1^\star + \mathbf{d}, \ \mathbf{C}\boldsymbol{\alpha}_2^\star + \mathbf{d}\ ]$$

else

    If $|p^\star| \neq 0$ then $\hat{\mathbf{S}} := [\ \hat{\mathbf{S}}, \ \mathbf{C}\boldsymbol{\alpha}_1^\star + \mathbf{d}\ ]$.
    If $|q^\star| \neq 0$ then $\hat{\mathbf{S}} := [\ \hat{\mathbf{S}}, \ \mathbf{C}\boldsymbol{\alpha}_2^\star + \mathbf{d}\ ]$.

Step 5. Update l by the number of columns of $\hat{\mathbf{S}}$.

Step 6. Apply QR decomposition

$$\hat{\mathbf{S}} = \mathbf{Q}_1 \mathbf{R}_1,$$

where $\mathbf{Q}_1 \in \mathbb{R}^{L \times l}$ and $\mathbf{R}_1 \in \mathbb{R}^{l \times l}$. Update $\mathbf{B} := \mathbf{I}_L - \mathbf{Q}_1\mathbf{Q}_1^T$.

Step 7. Repeat **Step 2** to **Step 6** until $l = N$.

Based on Theorem 1, Lemma 6, Lemma 7, and the complexity discussion above, we conclude that

Proposition 2 *Table 4.1 finds all the true source vectors $\boldsymbol{s}_1, ..., \boldsymbol{s}_N$ with probability 1, under the premises of (A1)-(A4). It does so with a worst-case complexity of $\mathcal{O}(L^{1.5}(N-1)^2)$.*

We have provided a practical implementation of CAMNS-LP at `http://www.ee.cuhk.edu.hk/~wkma/CAMNS/CAMNS.htm`. The source codes were written in MATLAB, and are based on the reliable convex optimization software SeDuMi [54]. Readers who are interested in our work are encouraged to test the codes.

4.3 Alternating Volume Maximization Heuristics for CAMNS

The CAMNS-LP method developed in the last section elegantly takes advantage of the model assumptions to sequentially track down the extreme points or the true source vectors. In particular, the local dominant assumption (A3) plays a key role. Our simulation experience is that CAMNS-LP can provide good separation performance on average, even when the local dominance assumption is not perfectly satisfied. In this section we develop an alternate method that is also inspired by the CAMNS criterion, and it is intuitively expected to offer better robustness against model mismatch (violation of (A3)). As we will further elaborate soon, the idea is to perform simplex volume maximization. Unfortunately such an attempt will lead to a nonconvex optimization problem. We will propose an alternating, LP-based optimization heuristic approach to the simplex volume maximization problem. Although the alternating heuristics is suboptimal, simulation results will indicate that the alternating heuristics can provide a better separation than CAMNS-LP, by a factor of about several dBs in terms of sum-square-error performance (for data where local dominance is not perfectly satisfied).

Recall the CAMNS criterion in Criterion 2: Find the extreme points of the polyhedral set

$$\mathcal{F} = \left\{ \boldsymbol{\alpha} \in \mathbb{R}^{N-1} \mid \mathbf{C}\boldsymbol{\alpha} + \mathbf{d} \succeq \mathbf{0} \right\}$$

which, under the model assumptions in (A1)-(A4), is a simplex in form of

$$\mathcal{F} = \text{conv}\{\boldsymbol{\alpha}_1, \ldots, \boldsymbol{\alpha}_N\}.$$

For a simplex we can define its volume: A simplex, say denoted by $\text{conv}\{\boldsymbol{\beta}_1, \ldots, \boldsymbol{\beta}_N\} \subset \mathbb{R}^{N-1}$, has its volume given by [57]

$$V(\boldsymbol{\beta}_1, \ldots, \boldsymbol{\beta}_N) = \frac{|\det(\boldsymbol{\Delta}(\boldsymbol{\beta}_1, \ldots, \boldsymbol{\beta}_N))|}{(N-1)!}, \tag{4.28}$$

where

$$\boldsymbol{\Delta}(\boldsymbol{\beta}_1, \ldots, \boldsymbol{\beta}_N) = \begin{bmatrix} \boldsymbol{\beta}_1 & \cdots & \boldsymbol{\beta}_N \\ 1 & \cdots & 1 \end{bmatrix} \in \mathbb{R}^{N \times N}. \tag{4.29}$$

Suppose that $\{\boldsymbol{\beta}_1, \ldots, \boldsymbol{\beta}_N\} \subset \mathcal{F}$. As illustrated in the picture in Figure 4.5, the volume of $\text{conv}\{\boldsymbol{\beta}_1, \ldots, \boldsymbol{\beta}_N\}$ should be no greater than that of $\mathcal{F} = \text{conv}\{\boldsymbol{\alpha}_1, \ldots, \boldsymbol{\alpha}_N\}$. Hence, by finding $\{\boldsymbol{\beta}_1, \ldots, \boldsymbol{\beta}_N\} \subset \mathcal{F}$ such that its corresponding simplex volume is maximized, we would expect that $\{\boldsymbol{\beta}_1, \ldots, \boldsymbol{\beta}_N\}$ is exactly $\{\boldsymbol{\alpha}_1, \ldots, \boldsymbol{\alpha}_N\}$, the ground truth we are seeking. This leads to the following variation of the CAMNS criterion:
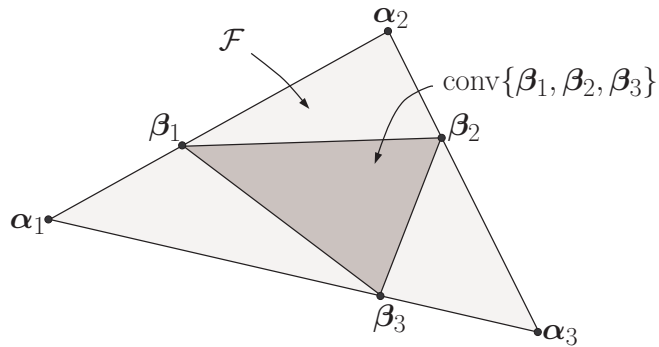
Figure 4.5. A geometric illustration for $\{\boldsymbol{\beta}_1, \ldots, \boldsymbol{\beta}_N\} \subset \mathcal{F}$ for $N = 3$.

Criterion 3 (Simplex Volume Maximization Alternative to Criterion 2)

Use the affine set fitting solution in Proposition 1 to compute $(\mathbf{C}, \mathbf{d})$*. Then, solve the volume maximization problem*

$$\{\hat{\boldsymbol{\alpha}}_1, \ldots, \hat{\boldsymbol{\alpha}}_N\} = \arg\max_{\boldsymbol{\beta}_1, \ldots, \boldsymbol{\beta}_N} \quad V(\boldsymbol{\beta}_1, \ldots, \boldsymbol{\beta}_N)$$

$$\text{s.t.} \quad \{\boldsymbol{\beta}_1, \ldots, \boldsymbol{\beta}_N\} \subset \mathcal{F}, \tag{4.30}$$

Output

$$\hat{\boldsymbol{s}}_i = \mathbf{C}\hat{\boldsymbol{\alpha}}_i + \mathbf{d}, \ i = 1, \ldots, N \tag{4.31}$$

as the set of estimated source vectors.

Like Criteria 1 and 2, Criterion 3 can be shown to provide perfect separation result as stated in the following theorem.

Theorem 3 *The globally optimal solution of (4.30) is uniquely given by* $\boldsymbol{\alpha}_1, \ldots, \boldsymbol{\alpha}_N$, *under the premises of (A1)-(A4).*

The proof of Theorem 3 is given in Appendix A.8. As we mentioned in the beginning of this section, what is interesting with simplex volume maximization is when local dominance is not perfectly satisfied: The polyhedral set $\mathcal{F}$ may no longer be a simplex under such circumstances, though it would exhibit a geometric structure similar to a simplex. Simplex volume maximization would still be applicable, because it gives a 'best' simplex approximation to $\mathcal{F}$. Figure 4.6 provides an illustration of our argument above.

In the volume maximization approach, the challenge is with the simplex volume maximization problem in (4.30). To see this, we substitute (4.12) and (4.28) into
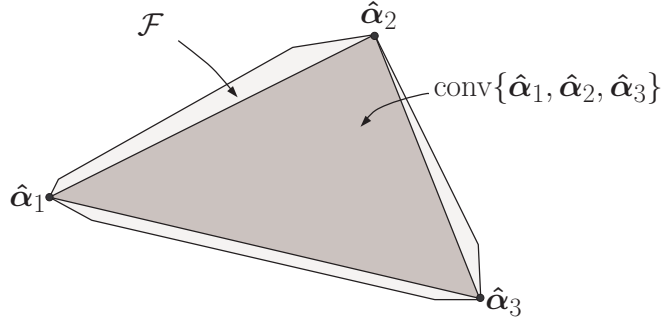
Figure 4.6. A geometric illustration for Criterion 3 when the local dominance assumption is not perfectly satisfied.

(4.30) to obtain a more explicit formulation of the simplex volume maximization problem:

$$\max_{\boldsymbol{\beta}_1,\ldots,\boldsymbol{\beta}_N} \quad |\det\left(\boldsymbol{\Delta}(\boldsymbol{\beta}_1,\ldots,\boldsymbol{\beta}_N)\right)|$$
$$\text{s.t.} \quad \mathbf{C}\boldsymbol{\beta}_i + \mathbf{d} \succeq \mathbf{0}, \ \forall \, i = 1,\ldots,N \tag{4.32}$$

The constraints of the problem above are affine (and convex), but the objective function is nonconvex.

Although a globally optimal solution of (4.32) may be difficult to obtain, we can approximate (4.32) in a convenient manner by using an alternating optimization heuristics proposed as follows. If we apply the cofactor expansion of $\boldsymbol{\Delta}(\boldsymbol{\beta}_1,\ldots,\boldsymbol{\beta}_N)$ along the jth column (for any j), we obtain an expression

$$\det(\boldsymbol{\Delta}(\boldsymbol{\beta}_1,\ldots,\boldsymbol{\beta}_N)) = \mathbf{b}_j^T\boldsymbol{\beta}_j + (-1)^{N+j}\det(\boldsymbol{\mathcal{B}}_{Nj}), \tag{4.33}$$

where $\mathbf{b}_j = [(-1)^{i+j}\det(\boldsymbol{\mathcal{B}}_{ij})]_{i=1}^{N-1} \in \mathbb{R}^{N-1}$ and $\boldsymbol{\mathcal{B}}_{ij} \in \mathbb{R}^{(N-1)\times(N-1)}$ is a submatrix of $\boldsymbol{\Delta}(\boldsymbol{\beta}_1,\ldots,\boldsymbol{\beta}_N)$ with the ith row and jth column being removed [57]. It is apparent from (5.22) that $\det(\boldsymbol{\Delta}(\boldsymbol{\beta}_1,\ldots,\boldsymbol{\beta}_N))$ is affine in each $\boldsymbol{\beta}_j$. Now, consider the partial

36

maximization of (4.32) with respect to $\boldsymbol{\beta}_j$, while fixing $\boldsymbol{\beta}_1, \ldots, \boldsymbol{\beta}_{j-1}, \boldsymbol{\beta}_{j+1}, \ldots, \boldsymbol{\beta}_N$:

$$\max_{\boldsymbol{\beta}_j \in \mathbb{R}^{N-1}} \quad \left| \mathbf{b}_j^T \boldsymbol{\beta}_j + (-1)^{N+j} \det(\boldsymbol{\mathcal{B}}_{Nj}) \right|$$
$$\text{s.t.} \quad \mathbf{C}\boldsymbol{\beta}_j + \mathbf{d} \succeq \mathbf{0}. \tag{4.34}$$

The objective function in (4.34) is still nonconvex, but (4.34) can be solved in a globally optimal manner by breaking it into two LPs:

$$p^\star = \max_{\boldsymbol{\beta}_j \in \mathbb{R}^{N-1}} \quad \mathbf{b}_j^T \boldsymbol{\beta}_j + (-1)^{N+j} \det(\boldsymbol{\mathcal{B}}_{Nj})$$
$$\text{s.t.} \quad \mathbf{C}\boldsymbol{\beta}_j + \mathbf{d} \succeq \mathbf{0}. \tag{4.35}$$

and

$$q^\star = \min_{\boldsymbol{\beta}_j \in \mathbb{R}^{N-1}} \quad \mathbf{b}_j^T \boldsymbol{\beta}_j + (-1)^{N+j} \det(\boldsymbol{\mathcal{B}}_{Nj})$$
$$\text{s.t.} \quad \mathbf{C}\boldsymbol{\beta}_j + \mathbf{d} \succeq \mathbf{0}. \tag{4.36}$$

The optimal solution of (4.34), denoted by $\hat{\boldsymbol{\alpha}}_j$, is the optimal solution of (4.35) if $|p^\star| > |q^\star|$, and the optimal solution of (4.36) if $|q^\star| > |p^\star|$. This partial maximization is conducted alternately (i.e., $j := (j \text{ modulo } N) + 1$) until some stopping rule is satisfied.

The CAMNS alternating volume maximization heuristics, or simply CAMNS-AVM, is summarized in Table 4.2.

Like alternating optimization in many other applications, the number of iterations required for CAMNS-AVM to terminate may be difficult to analyze. From the simulations (to be presented in the next section), we found that for an accuracy of $\varepsilon = 10^{-13}$, CAMNS-AVM takes about 2 to 4 iterations to terminate, which is surprisingly quite small. Following the same complexity evaluation as in CAMNS-LP, CAMNS-AVM has a complexity of $\mathcal{O}(N^2 L^{1.5})$ per iteration. This means that CAMNS-AVM is only

37

Table 4.2. A summary of the CAMNS-AVM method.

Given a convergence tolerance $\varepsilon > 0$, an affine set characterization 2-tuple $(\mathbf{C}, \mathbf{d})$, and the observations $\boldsymbol{x}_1, \ldots, \boldsymbol{x}_M$.

Step 1. Initialize $\boldsymbol{\beta}_1, \ldots, \boldsymbol{\beta}_N \in \mathcal{F}$. (our suggested choice: Randomly choose N vectors out of the M observation-constructed vectors $\{\ \mathbf{C}^\dagger(\boldsymbol{x}_i - \mathbf{d}),\ i = 1, \ldots, M\ \}$). Set

$$\boldsymbol{\Delta}(\boldsymbol{\beta}_1, \ldots, \boldsymbol{\beta}_N) = \left[\begin{array}{ccc} \boldsymbol{\beta}_1 & \cdots & \boldsymbol{\beta}_N \\ 1 & \cdots & 1 \end{array} \right],$$

$\varrho := |\det(\boldsymbol{\Delta}(\boldsymbol{\beta}_1, \ldots, \boldsymbol{\beta}_N))|$, and $j := 1$.

Step 2. Update $\boldsymbol{\mathcal{B}}_{ij}$ by a submatrix of $\boldsymbol{\Delta}(\boldsymbol{\beta}_1, \ldots, \boldsymbol{\beta}_N)$ with the ith row and jth column removed, and $\mathbf{b}_j := [(-1)^{i+j}\det(\boldsymbol{\mathcal{B}}_{ij})]_{i=1}^{N-1}$.

Step 3. Solve the LPs

$$p^\star = \max_{\boldsymbol{\beta}_j \in \mathbb{R}^{N-1}} \quad \mathbf{b}_j^T \boldsymbol{\beta}_j + (-1)^{N+j}\det(\boldsymbol{\mathcal{B}}_{Nj})$$
$$\text{s.t.} \quad \mathbf{C}\boldsymbol{\beta}_j + \mathbf{d} \succeq \mathbf{0}.$$

and

$$q^\star = \min_{\boldsymbol{\beta}_j \in \mathbb{R}^{N-1}} \quad \mathbf{b}_j^T \boldsymbol{\beta}_j + (-1)^{N+j}\det(\boldsymbol{\mathcal{B}}_{Nj})$$
$$\text{s.t.} \quad \mathbf{C}\boldsymbol{\beta}_j + \mathbf{d} \succeq \mathbf{0}.$$

and thereby obtain their optimal solutions, denoted by $\bar{\boldsymbol{\beta}}_j$ and $\underline{\boldsymbol{\beta}}_j$, respectively.

Step 4. If $|p^\star| > |q^\star|$, then update $\boldsymbol{\beta}_j := \bar{\boldsymbol{\beta}}_j$. Otherwise, update $\boldsymbol{\beta}_j := \underline{\boldsymbol{\beta}}_j$.

Step 5. If $(j \text{ modulo } N) \neq 0$, then $j := j + 1$, and go to **Step 2**, else

    If $|\max\{|p^\star|, |q^\star|\} - \varrho|/\varrho < \varepsilon$, then $\hat{\boldsymbol{\alpha}}_i = \boldsymbol{\beta}_i$ for $i = 1, \ldots, N$.

    Otherwise, set $\varrho := \max\{|p^\star|, |q^\star|\}$, $j := 1$, and go to **Step 2**.

Step 6. Compute the source estimates $\hat{\boldsymbol{s}}_1, \ldots, \hat{\boldsymbol{s}}_N$ through $\hat{\boldsymbol{s}}_j = \mathbf{C}\hat{\boldsymbol{\alpha}}_j + \mathbf{d}$.
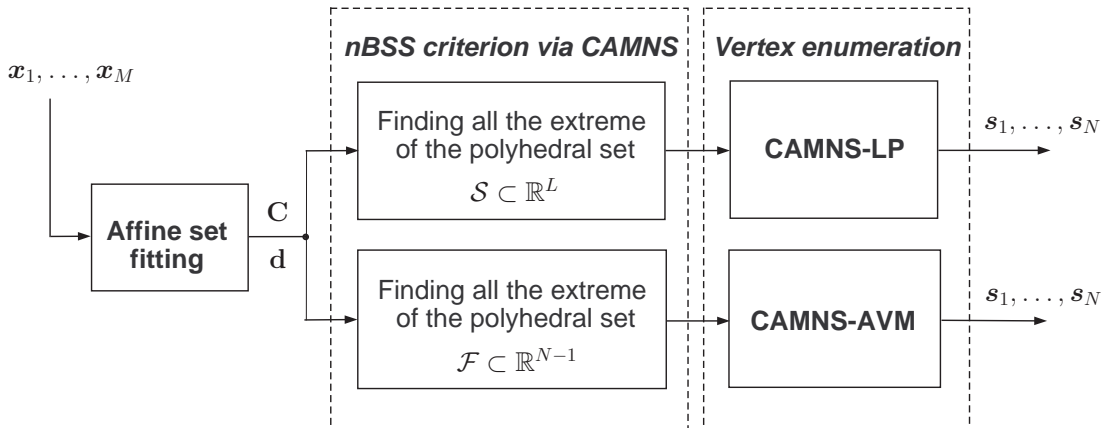
Figure 4.7. Signal processing flow chart of the proposed CAMNS-based algorithms.

about 2 to 4 times more computationally expensive than CAMNS-LP (by our empirical experience).

We summarize CAMNS criterion and the associated algorithms by a signal processing flow chart in Figure 4.7.

4.4 Numerical Results

To demonstrate the efficacy of the CAMNS-LP and CAMNS-AVM methods, four simulation results are presented here. Section 4.4.2 considers a cell image scenario where our task is to distinguish different types of cells. Section 4.4.3 focuses on a challenging scenario where ghosting effects take place in photography. Section 4.4.4 considers a problem in which the sources are faces of five different persons. Section 4.4.5 uses Monte Carlo simulation to evaluate the performance of CAMNS-based algorithms under noisy condition. For performance comparison, we also test three standard nBSS algorithms, namely non-negative matrix factorization (NMF) [15], non-negative independent component analysis (nICA) [11], and Ergodan's algorithm (a BSS method that exploits magnitude bounds of the sources) [6].

The performance measure used in this chapter is described as follows. Let $\mathbf{S} =$

$[\boldsymbol{s}_1, \ldots, \boldsymbol{s}_N]$ be the true multi-source signal matrix, and $\hat{\mathbf{S}} = [\hat{\boldsymbol{s}}_1, \ldots, \hat{\boldsymbol{s}}_N]$ be the multi-source output of a BSS algorithm. It is well known that a BSS algorithm is inherently subject to permutation and scaling ambiguities. We propose a sum square error (SSE) measure for $\mathbf{S}$ and $\hat{\mathbf{S}}$ [58,59], given as follows:

$$e(\mathbf{S}, \hat{\mathbf{S}}) = \min_{\boldsymbol{\pi} \in \Pi_N} \sum_{i=1}^{N} \left\| \boldsymbol{s}_i - \frac{\|\boldsymbol{s}_i\|}{\|\hat{\boldsymbol{s}}_{\pi_i}\|} \hat{\boldsymbol{s}}_{\pi_i} \right\|^2 \tag{4.37}$$

where $\boldsymbol{\pi} = (\pi_1, \ldots, \pi_N)$, and $\Pi_N = \{\boldsymbol{\pi} \in \mathbb{R}^N \mid \pi_i \in \{1, 2, \ldots, N\}, \ \pi_i \neq \pi_j \text{ for } i \neq j\}$ is the set of all permutations of $\{1, 2, ..., N\}$. The optimization of (4.37) is to adjust the permutation $\boldsymbol{\pi}$ such that the best match between true and estimated signals is yielded, while the factor $\|\boldsymbol{s}_i\| / \|\hat{\boldsymbol{s}}_{\pi_i}\|$ is to get rid of the scaling ambiguity. Problem (4.37) is the optimal assignment problem which can be efficiently solved by Hungarian algorithm [1] [60].

4.4.1 Example of 2-source Case: Dual-energy Chest X-ray Imaging

Dual-energy chest x-ray imaging is clinically used for detecting calcified granuloma, a symptom of lung nodules [61]. The diagnostic images are acquired from two stacked detectors separated by a copper filter along which x-rays at two different energies are passed. For visualizing the symptom of calcified granuloma, it is necessary to separate bone structures and soft tissue from the diagnostic images.

In this simulation we have two 164×164 source images, one representing bone structure and the other corresponding soft tissue. The two images were taken from [62] and they are displayed in Figure 4.8(a). Each image was represented by a source vector $\boldsymbol{s}_i \in \mathbb{R}^L$, by scanning the image vertically from top left to bottom right (thereby

---

[1] A Matlab implementation is available at `http://si.utia.cas.cz/Tichavsky.html`.

$L = 164^2 = 26896$). We found that the two source signals satisfy the local dominant assumption [or (A3)] perfectly, by numerical inspection. The observation vectors, or the diagnostic images are synthetically generated using a mixing matrix

$$\mathbf{A} = \begin{bmatrix} 0.55 & 0.45 \\ 0.63 & 0.37 \end{bmatrix}. \tag{4.38}$$

The mixed images are shown in Figure 4.8(b). The separated images of the various nBSS methods are illustrated in Figure 4.8(c)-(g). By visual inspection, the CAMNS-based methods appeared to yield the best separation among the various methods. In Table 4.3, the various methods were quantitatively compared, in terms of the SSE in (4.37). The table indicates that the CAMNS-based methods achieved perfect separation.

4.4.2 Example of 3-Source Case: Cell Separation

In this example three 125×125 cell images were taken from [2] as the source images and are displayed in Figure 4.9(a). For the three source images, we found that the local dominance assumption is not perfectly satisfied. To shed some light into this, we propose a measure called the *local dominance proximity factor* (LDPF) of the ith source, defined as follows:

$$\kappa_i = \max_{n=1,\dots,L} \frac{s_i[n]}{\sum_{j \neq i} s_j[n]}. \tag{4.39}$$

When $\kappa_i = \infty$, we have the ith source satisfying the local dominance assumption perfectly. The values of κ_i's in this example are shown in Table 4.4, where we see that the LDPFs of the three sources are strong but not infinite.

The three observation vectors were synthetically generated using a mixing matrix
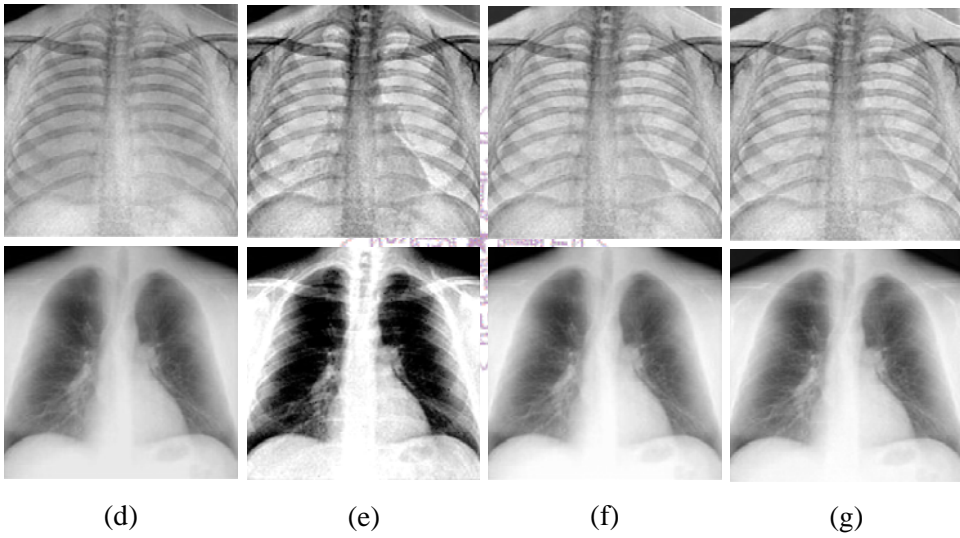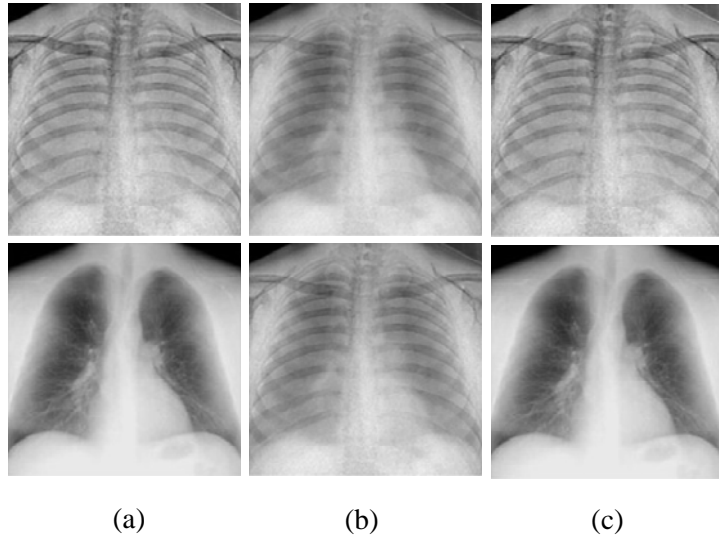
Figure 4.8. Dual-energy chest x-ray imaging: (a) The sources, (b) the synthetic observations, and the extracted sources obtained by (c) CAMNS-AVM method, (d) CAMNS-LP method, (e) NMF, (f) nICA and (g) Erdogan's algorithm.

$$\mathbf{A} = \begin{bmatrix} 0.20 & 0.62 & 0.18 \\ 0.35 & 0.37 & 0.28 \\ 0.40 & 0.40 & 0.20 \end{bmatrix}. \tag{4.40}$$

The mixed images are shown in Figure 4.9(b). The separated images of the various nBSS methods are illustrated in Figure 4.9(c)-(g). By visual inspection, the CAMNS-

Table 4.3. The SSEs of the various nBSS methods in the four scenarios.

	SSE $e(\mathbf{S}, \hat{\mathbf{S}})$ (in dB)				
	CAMNS-AVM	CAMNS-LP	NMF	nICA	Erdogan's algorithm
Dual-energy X-ray	-261.139	-252.215	30.837	24.421	23.837
Cell separation	3.710	12.323	23.426	19.691	19.002
Ghosting reduction	11.909	20.754	38.620	41.896	39.126
Human face separation	0.816	17.188	39.828	43.581	45.438

based methods provided good separation, despite the fact that the local dominance assumption is not perfectly satisfied. This result indicates that the CAMNS-based methods are robust against violation of local dominance. The SSE performance of the various methods is given in Table 4.3. We observe that the CAMNS-AVM method yielded the best performance among all the methods under test, and then followed by CAMNS-LP. This suggests that CAMNS-AVM was more robust than CAMNS-LP, when local dominance is not exactly satisfied. This result will be further confirmed by the Monte Carlo simulation in Section 4.4.5. Moreover, the SSE performance of nICA and Erdogan's algorithm are reasonably good. The reason for this is that the source uncorrelatedness assumption required by nICA and Erdogan's algorithm is approximately satisfied in this example. To see this, we calculate the average cross-correlation between the sources; i.e.,

$$\varrho = \frac{2}{N(N-1)} \left(\sum_{i=1}^{N-1} \sum_{j=i+1}^{N} \frac{(\boldsymbol{s}_i - \boldsymbol{\mu}(\boldsymbol{s}_i))^T (\boldsymbol{s}_j - \boldsymbol{\mu}(\boldsymbol{s}_j))}{\|\boldsymbol{s}_i - \boldsymbol{\mu}(\boldsymbol{s}_i)\| \|\boldsymbol{s}_j - \boldsymbol{\mu}(\boldsymbol{s}_j)\|} \right), \qquad (4.41)$$

where $\boldsymbol{\mu}(\boldsymbol{s}) = (\mathbf{1}_L^T \boldsymbol{s}/L)\mathbf{1}_L$ for any $\boldsymbol{s} \in \mathbb{R}^L$. The value of ϱ in this example is shown in Table 4.5, where we see that the average cross-correlation between the three sources is quite small (approximately zero). As we will see later when the sources are highly dependent, i.e., large value of ϱ, the performance of nICA and Erdogan's algorithm is significantly degraded.
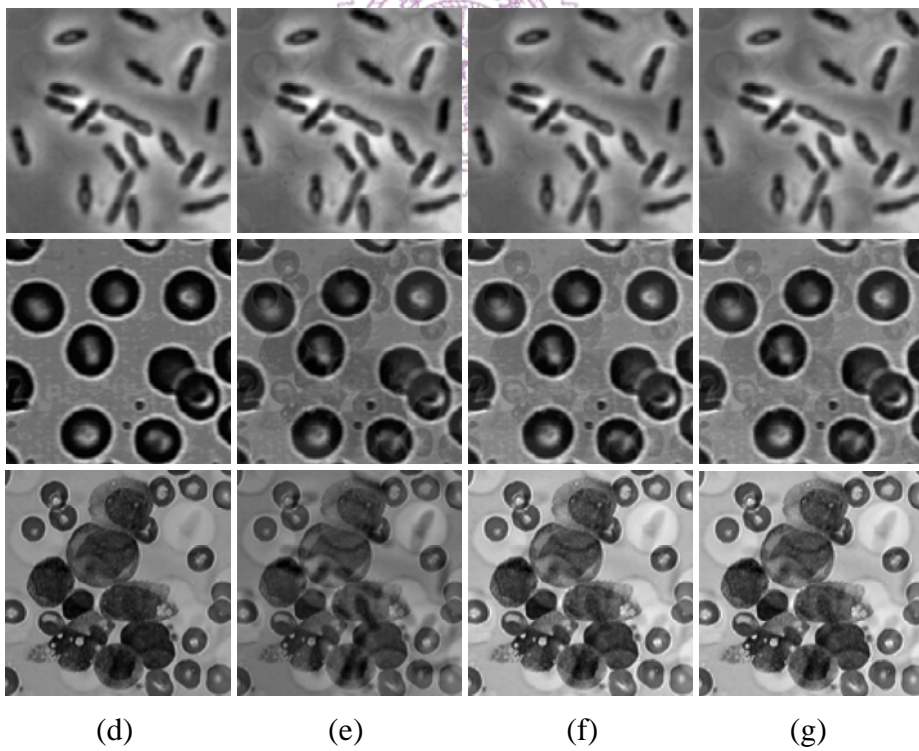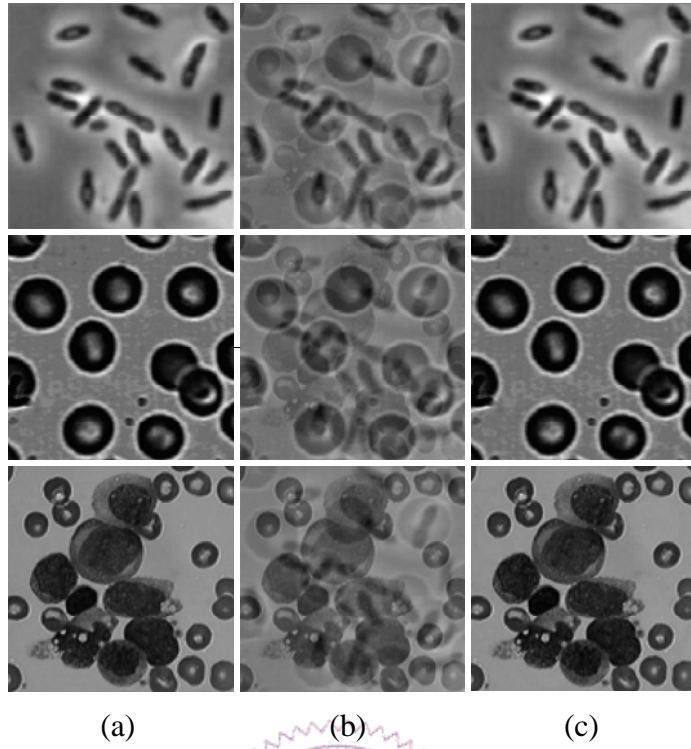
Figure 4.9. Cell separation: (a) The sources, (b) the synthetic observations, and the extracted sources obtained by (c) CAMNS-AVM method, (d) CAMNS-LP method, (e) NMF, (f) nICA and (g) Erdogan's algorithm.

Table 4.4. Local dominance proximity factors in the four scenarios.

	κ_i				
	source 1	source 2	source 3	source 4	source 5
Dual-energy X-ray	∞	∞	-	-	-
Cell separation	48.667	3.821	15.200	-	-
Ghosting reduction	2.133	2.385	2.384	2.080	-
Human face separation	10.450	9.107	5.000	3.467	2.450

Table 4.5. Average cross-correlation between the sources ϱ in the four scenarios.

	Dual-energy X-ray	Cell separation	Ghosting reduction	Human face separation
ϱ	0.650	0.023	0.349	0.320

4.4.3 Example of 4-Source Case: Ghosting Effect

We used a 285×285 Lena image taken from [2] as one source and then shifted it diagonally to create three more sources; see Figure 4.10(a). Apparently, these sources are strongly correlated. Even worse, their LDPFs, shown in Table 4.4 are poor when compared to the previous examples. The mixing matrix used was

$$\mathbf{A} = \begin{bmatrix} 0.02 & 0.37 & 0.31 & 0.30 \\ 0.31 & 0.21 & 0.26 & 0.22 \\ 0.05 & 0.38 & 0.28 & 0.29 \\ 0.33 & 0.23 & 0.21 & 0.23 \end{bmatrix}. \tag{4.42}$$

Figure 4.10(b) displays the synthetic observations, where the mixing effect is reminiscent of the ghosting effect in analog televisions. The image separation results are illustrated in Figure 4.10(c)-(g). Clearly, only the CAMNS-based methods provided sufficiently good mitigation of the "ghosts". This result once again confirms that the CAMNS-based methods are not very sensitive to the effect of local dominance violation. The numerical results shown in Table 4.3 reflect that the SSE of CAMNS-AVM

45

is about 9 dB smaller than that of CAMNS-LP, which can be validated by visual inspection on Figure 4.10(d) where there are slight residuals on the 4th separated image. We argue that the residuals are harder to notice for the CAMNS-AVM method. In addition, one can easily observe that the SSE performance of nICA and Erdogan's algorithm is poor due to the high correlation between the sources in this example.

4.4.4 Example of 5-Source Case: Human Face Separation

Five 240×320 photos taken from five persons were used as the source images in this example; see Figure 4.11(a). Since each human face was captured almost at the same position, the source images have some correlations. Once again, the local dominance assumption is not perfectly satisfied as shown in Table 4.4. The five mixed images, displayed in Figure 4.11(b) were generated through a mixing matrix given by

$$\mathbf{A} = \begin{bmatrix} 0.01 & 0.05 & 0.35 & 0.21 & 0.38 \\ 0.04 & 0.14 & 0.26 & 0.20 & 0.36 \\ 0.23 & 0.26 & 0.19 & 0.28 & 0.04 \\ 0.12 & 0.23 & 0.19 & 0.22 & 0.24 \\ 0.29 & 0.32 & 0.02 & 0.12 & 0.25 \end{bmatrix}. \tag{4.43}$$

Figures 4.11(c)-(g) show the separated images of the various nBSS methods. Apparently, one can see that the CAMNS-based methods have more accurate separation than the other methods, except some slight residual image appearing in the 2nd CAMNS-LP separated image, by careful visual inspection. The numerical results shown in Table 4.3 indicate that the CAMNS-based methods performed better than the other methods. Moreover, comparing CAMNS-AVM and CAMNS-LP, there is a large performance gap of about 16 dB. Again, the poor SSE performance of nICA and Ergogan's algorithm is due to the strong correlation between the sources in this example.

46
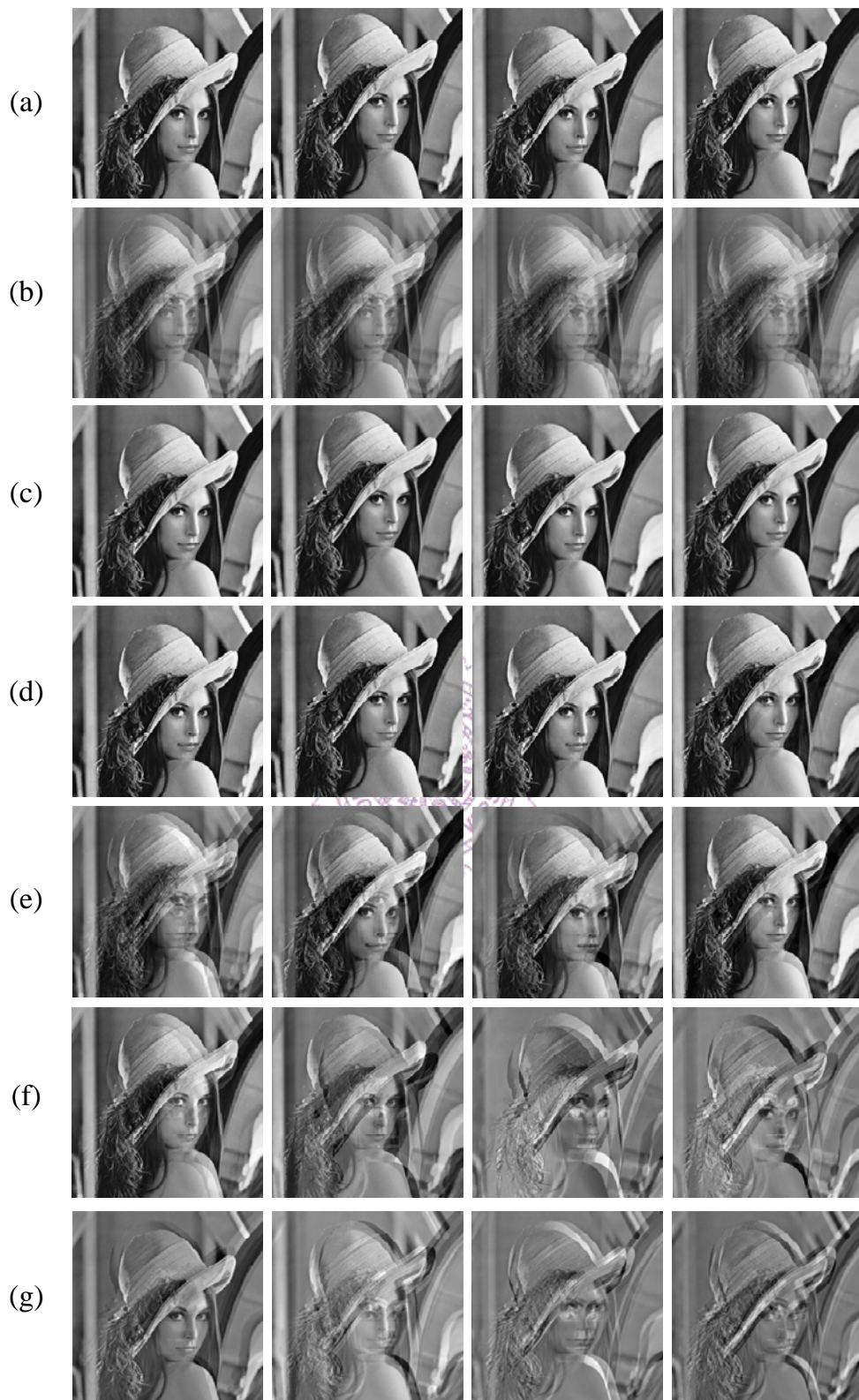
Figure 4.10. Ghosting reduction: (a) The sources, (b) the synthetic observations, and the extracted sources obtained by (c) CAMNS-AVM method, (d) CAMNS-LP method, (e) NMF, (f) nICA and (g) Erdogan's algorithm.

47
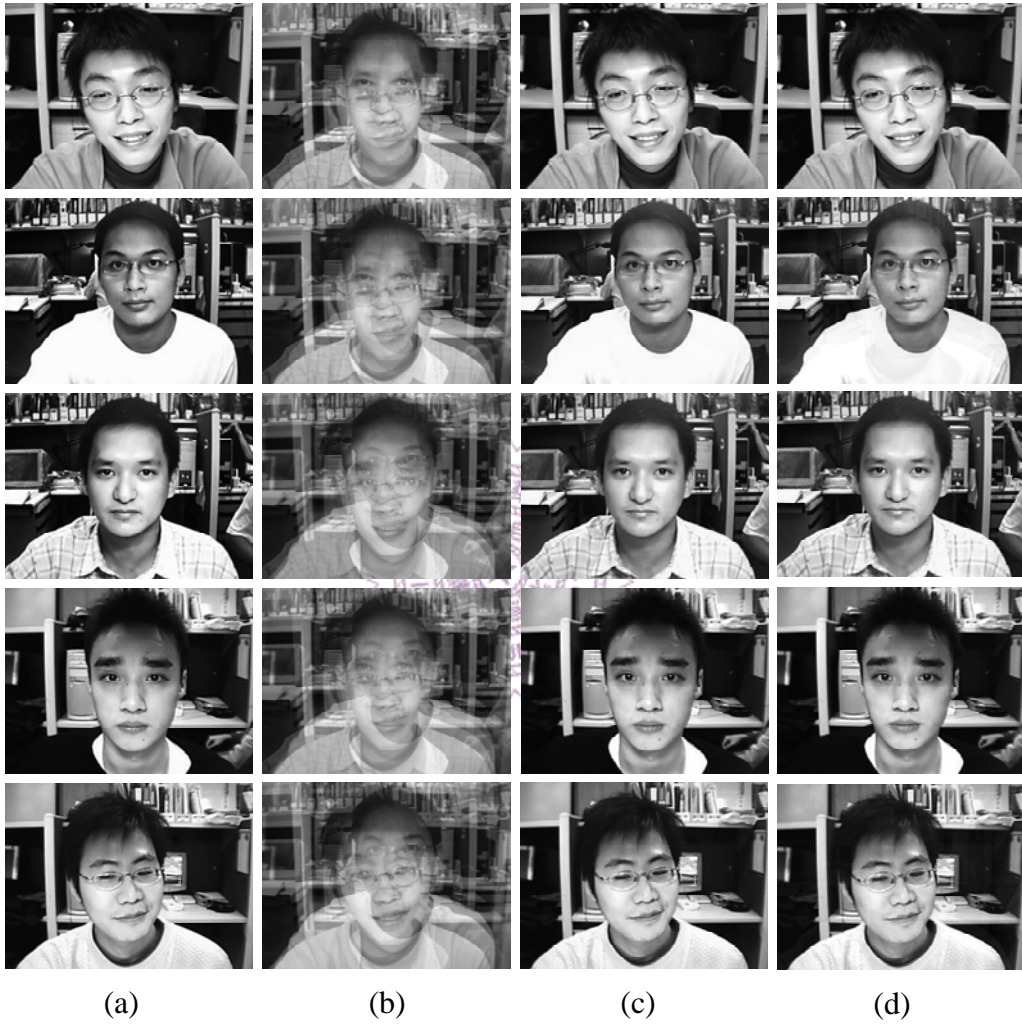
Figure 4.11. Human face separation: (a) The sources, (b) the synthetic observations, and the extracted sources obtained by (c) CAMNS-AVM method and (d) CAMNS-LP method.

(e)　　　　　　(f)　　　　　　(g)
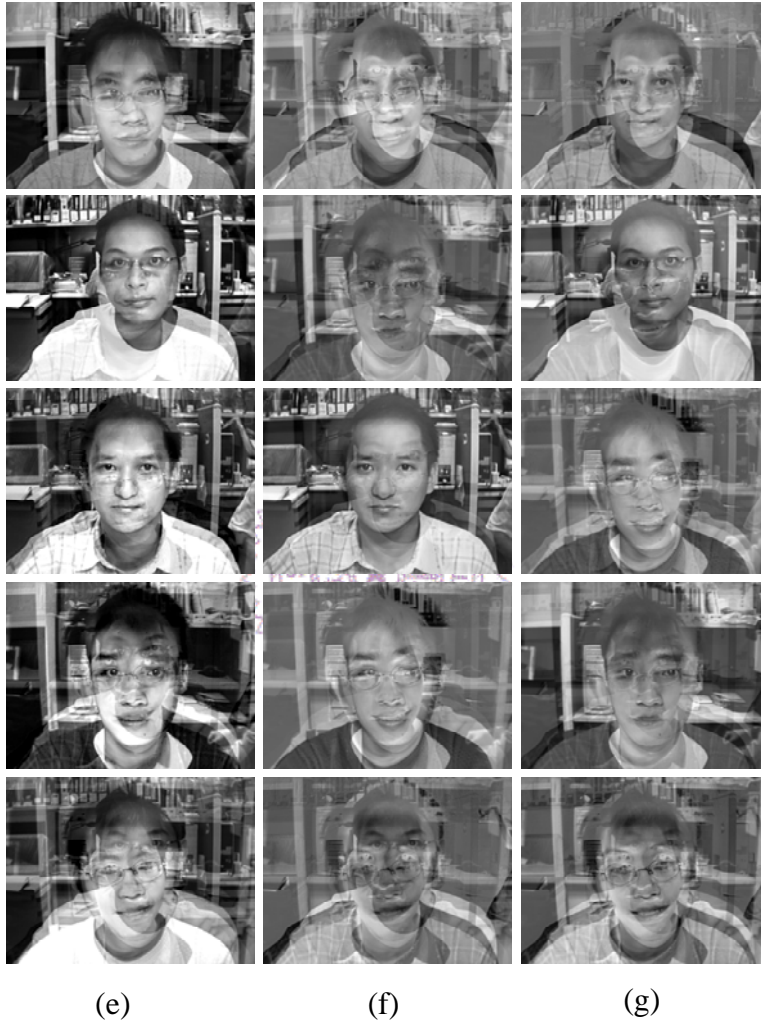
Figure 4.11. Human face separation (continued): The extracted sources obtained by (e) NMF, (f) nICA and (g) Erdogan's algorithm.
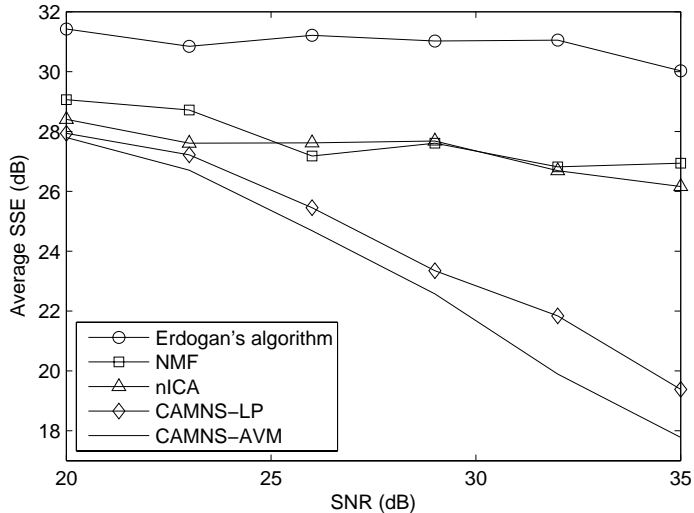
Figure 4.12. Performance evaluation of the CAMNS-based methods, NMF, nICA and Erdogan's method for the cell image experiment for $N = 3$, $M = 6$, and different SNRs.

4.4.5 Monte Carlo Simulation: Noisy Environment

We used Monte Carlo simulation to test the performance of the various methods when noise is present. The three cell images in Figure 4.9(a) were used to generate six noisy observations. The noise is independent and identically distributed (i.i.d.), following a Gaussian distribution with zero mean and variance σ^2. To maintain non-negativity of the observations in the simulation, we manually set the negative noisy observations to zero. We performed 100 independent runs. At each run the mixing matrix was i.i.d. uniformly generated on [0,1] and then each row was normalized to 1 to maintain (A3). The average SSE for different SNRs (defined here as SNR= $\sum_{i=1}^{N} \|\boldsymbol{s}_i\|^2 / LN\sigma^2$) are shown in Figure 4.12. One can see that the CAMNS-based methods performed better than the other methods.

We also examine the performance of the various methods for different number of noisy observations with fixed SNR= 25 (dB). The average SSE for the various methods are shown in Figure 4.13. One can see that the performance of CAMNS-based methods become better when more observations are given. This phenomenon clearly

50
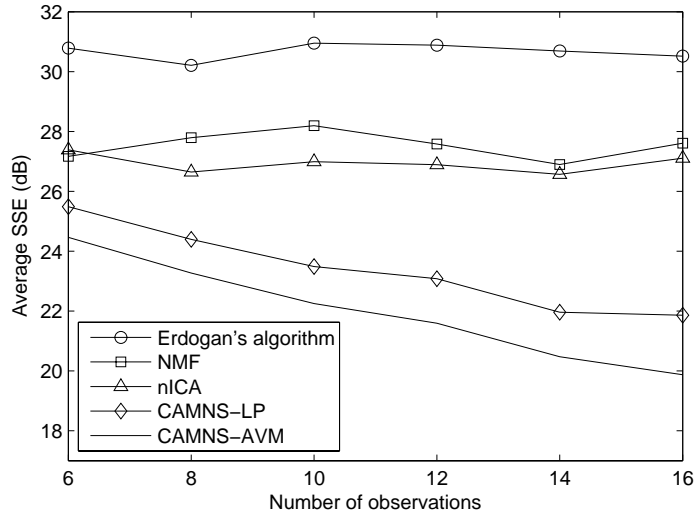
Figure 4.13. Performance evaluation of the CAMNS-based methods, NMF, nICA and Erdogan's method for the cell image experiment for $N = 3$, SNR= 25 (dB), and different number of noisy observations.

validated the noise mitigation merit of the affine set fitting procedure (Proposition 1) in CAMNS.
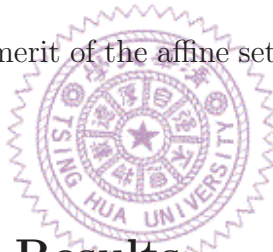
4.5 Experimental Results

A more stringent evaluation of the applicability of CAMNS framework is to directly test it with real image data. In this section, we used two sets of in-house real optical images to evaluate the performance of CAMNS. One is a set of dynamic fluorescent images, and the other is a set of multispectral images. These two data sets were based on the small mouse model, and were provided by Cambridge Research & Instrumentation (CRi), Inc[2].

4.5.1 Experiment: Dynamic Fluorescent Imaging

Fluorescence molecular imaging in vivo has great potential for advancing basic research and for discovery and development of drugs. However, widespread adoption of this modality is being held back because of obstacles to truly quantitative imaging of deeper organs, tissues, and targets. Hence, there is a need for imaging tools that can accurately and clearly acquire the data regardless of the location and nature of the molecular contrast agents being used [46].

Many researchers are exploring the use of multi-mode imaging, including co-registered X-ray, computed tomography and/or MRI, for "anatomical co-registration" (a capability which can help identify and locate the internal organ or structure from which a molecular signal may have originated). While promising, these are complex and costly.

Elizabeth Hillman et al. [46] recently describe a simple and new approach to anatomical co-registration for optically based small-animal imaging, which does not require multi-modality image acquisition but instead utilizes a time-series of fluorescent images acquired following a small bolus injection of a near-infrared dye. In [46], the authors utilize principal component analysis (PCA) and non-negative least-squares method for estimating anatomical maps of distinct organs (or sources). This problem can be generally viewed as an nBSS problem.

To perform anatomical co-registration using the CAMNS framework, we used two sets of dynamic fluorescent images (696×512 pixels) of a mouse acquired at supine and prone positions, respectively, each of which contains 150 images. Before applying the CAMNS framework to the data set, some preprocessing are needed as follows. We applied target masking to the image data set aiming to remove non-informative image pixels, and performed sum-based normalization to each observed image $\boldsymbol{x}_i$ such that assumption (A4) is satisfied [see Example 4]. Moreover, the number of sources N was empirically given by counting the major internal organs, which is likely less

than the true number of sources. Possibly due to such a source number mismatch problem, CAMNS framework would suffer from some amount of performance degradation. Therefore, we incorporated some prior knowledge to CAMNS framework to improve its effectiveness for real data applications. In particular, to find the extreme points of the polyhedral set $\mathcal{S}$ given by (4.9), we manually selected the direction $\mathbf{r} \in \mathbb{R}^L$ in solving (4.22), rather than the one randomly generated following Gaussian distribution. The modification of CAMNS is given as follows:

Example 7 CAMNS with Prior Information (CAMNS-PI)

The idea of CAMNS-PI is to maximize the average intensity of the signal within region of interest (ROI), while minimizing the average intensity of the signal out of the ROI. The ROI can be manually selected using prior knowledge of the organ (or source) location.

Now, consider to extract the source with the given ROI. Assume that there are L pixels in one observation indexed from 1 to L. Let the ROI have K pixels with the index $\mathcal{I} = \{i_1, \ldots, i_K\}$ and let the index of the non-ROI pixels denoted as $\mathcal{I}' = \{1, \ldots, L\} \setminus \mathcal{I}$ contains $L - K$ pixels. From (4.24), the idea of CAMNS-PI can be easily formulated as follows:

$$
\begin{aligned}
\max_{\boldsymbol{\alpha}} \quad & \mathbf{r}^T(\mathbf{C}\boldsymbol{\alpha} + \mathbf{d}) \\
\text{s.t.} \quad & \mathbf{C}\boldsymbol{\alpha} + \mathbf{d} \succeq \mathbf{0}.
\end{aligned}
\tag{4.44}
$$

where $\mathbf{r} = [\, r_1, \ldots, r_L \,]^T \in \mathbb{R}^L$ is given by

$$
\begin{aligned}
r_i &= 1/K, \ \forall \ i \in \mathcal{I}, \\
r_j &= -1/(L - K), \ \forall \ j \in \mathcal{I}'.
\end{aligned}
$$

Supposing $\boldsymbol{\alpha}^\star$ is obtained by solving (4.44), the source is then recovered by $\boldsymbol{s}^\star =$

$\mathbf{C\alpha^\star + d}$. By following the same procedure for N different ROIs (that correspond to the N sources), one can eventually get all the N anatomical maps. Even though the ROI is not perfectly given, the CAMNS-PI can still yield promising results, suggested by our experimental experience.

Figure 4.14 shows the results of CAMNS-PI for the supine-position image data, where the number of sources N was empirically set to 8. The last two rows of Figure 4.14 are the estimated source signals, say, the images associated with the locations of tongue, salivary gland, lymph nodes, lungs, heart, liver, small intestine, and blood vessels. By combining these eight estimated source images into a composite pseudocolor image, one may directly produce the anatomical map of the mouse in a supine position, as shown in the first row of Figure 4.14. We also show the results of CAMNS-PI for the prone-position image data in Figure 4.15, where the number of sources N was set to 5. The last two rows of Figure 4.15 are the estimated source images, corresponding to kidney, liver, brain, lung, and blood vessels, respectively, and the first row of Figure 4.15 is the estimated anatomical map of the prone-position mouse. It can be seen that the above anatomical maps obtained by CAMNS-PI clearly revealed the true organ locations of a mouse in both supine and prone positions. The results presented here also have a high agreement with the anatomy reference [63].

4.5.2 Experiment: Multispectral Imaging

Multispectral imaging has become a popular way to discriminate multiple proteins, organelles, or functions in a cell or animal. However, there are two general drawbacks in multispectral imaging, leading to the inability to accurately identify fluorescence contribution from multiple dyes. One is the spatially/spectrally-overlapped problem of the dye that may result in hardly identifying one particular target. The other is autofluorescence of the tissue such as skin and food that would limit the imaging sen-
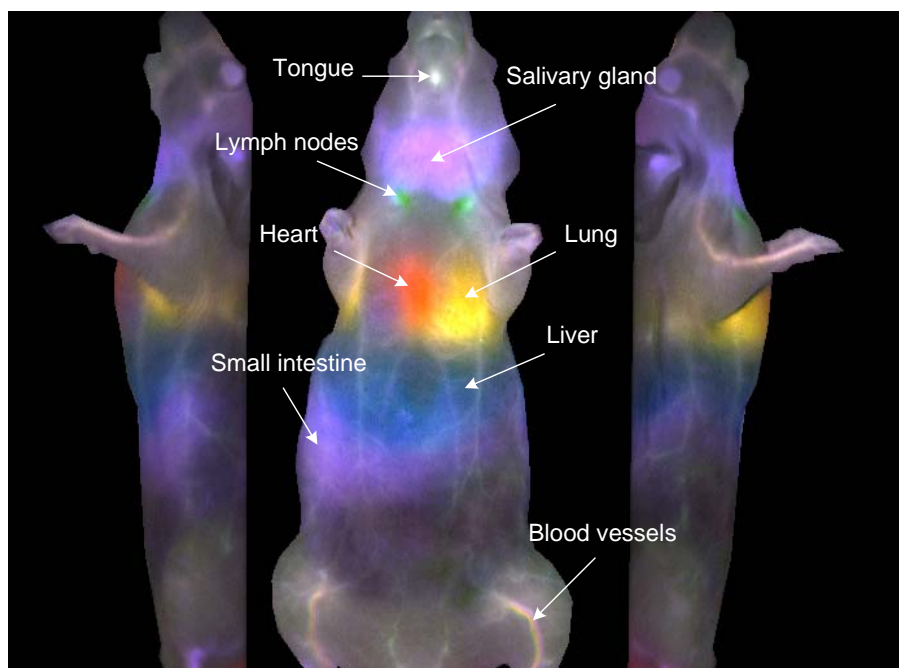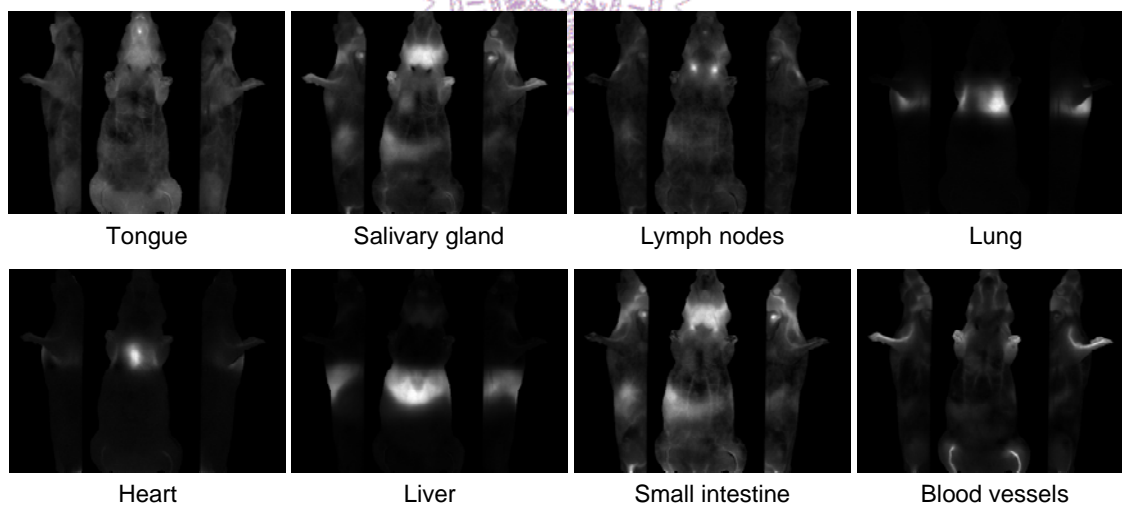
Figure 4.14. The anatomical map of a mouse in a supine position (first row) and the associated eight unmixed signals (last two rows) obtained by CAMNS-PI with pseudocolors, which correspond to tongue, salivary gland, lymph nodes, lungs, heart, liver, small intestine, and blood vessels, respectively.
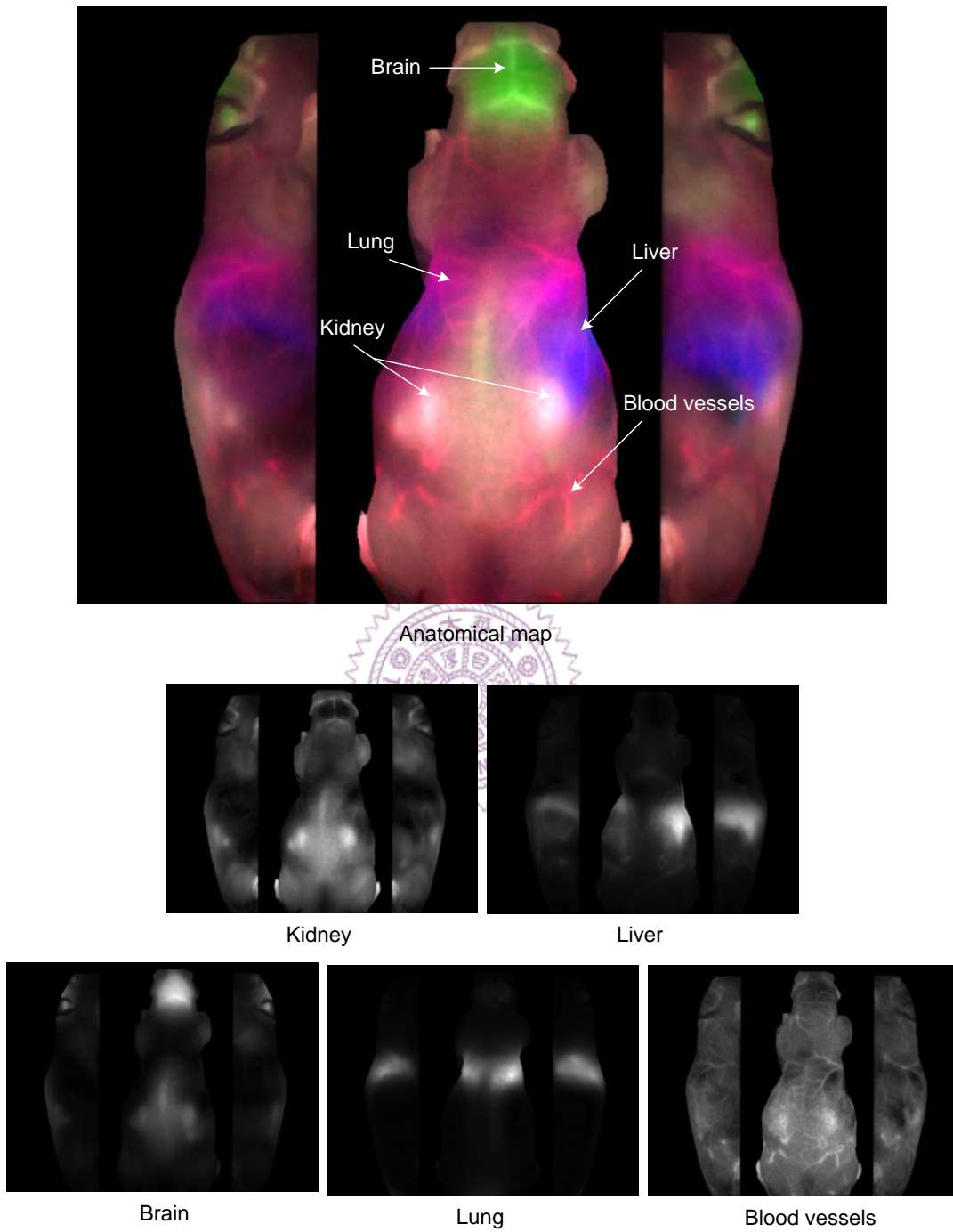
Figure 4.15. The anatomical map of a mouse in a prone position (first row) and the associated five unmixed signals (last two rows) obtained by CAMNS-PI with pseudocolors, which correspond to kidney, liver, brain, lung, and blood vessels, respectively.

sitivity. To resolve these problems by separating the fluorescence images into distribution maps of autofluorescence and dyes, we can generally formulate this as an nBSS problem [64,65,66]. Once the autofluorescence signals have been extracted/separated, one may isolate them for ease of biological interpretation.

A pair of nude mice have been injected subcutaneously with three fluorophores (FITC, TRITC, and Cy3.5) and it also exhibited food autofluorescence. Similar to the experiment in Section 4.5.1, we applied target masking to the image data set, and performed sum-based normalization to each observed image $\boldsymbol{x}_i$. The number of sources N was set to 4. The results of CAMNS-PI for multispectral image data are shown in Figure 4.16. One can see that CAMNS-PI can clearly identified the three fluorophore signals and one food autofluorescence.

4.6 Summary

In this chapter, we have shown how convex analysis provides a new avenue to solve non-negative blind source separation problems. Using convex geometry concepts such as affine hull and convex hull, an analysis was carried out to show that under some appropriate assumptions, nBSS can be boiled down to a problem of finding extreme points of a polyhedral set. We have also shown how this extreme point finding problem can be solved by convex optimization, specifically by using LPs to systematically find all the extreme points.

The key success of this new nBSS framework is based on a deterministic signal assumption, i.e., local dominance. Local dominance is a good model assumption for sparse or high-contrast images, but it may not be perfectly satisfied sometimes. We have developed an alternative to the systematic LP method that is expected to yield better robustness against violation of local dominance. The idea is to solve a volume maximization problem. Despite the fact that the proposed algorithm uses heuristics

FITC signal

TRITC signal

Food
autofluoresence

Cy3.5 signal

Composite image

| FITC signal | TRITC signal | Cy3.5 signal | Food autofluorescence |
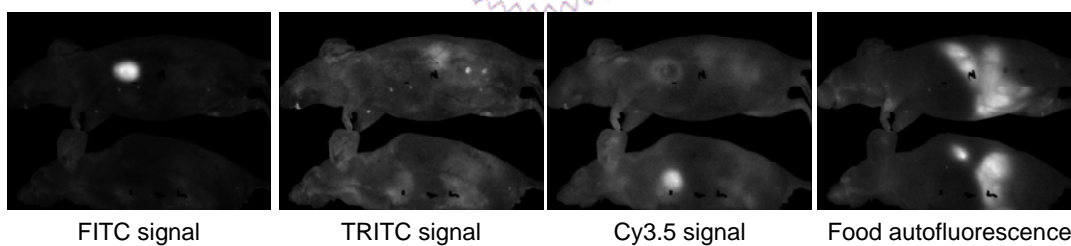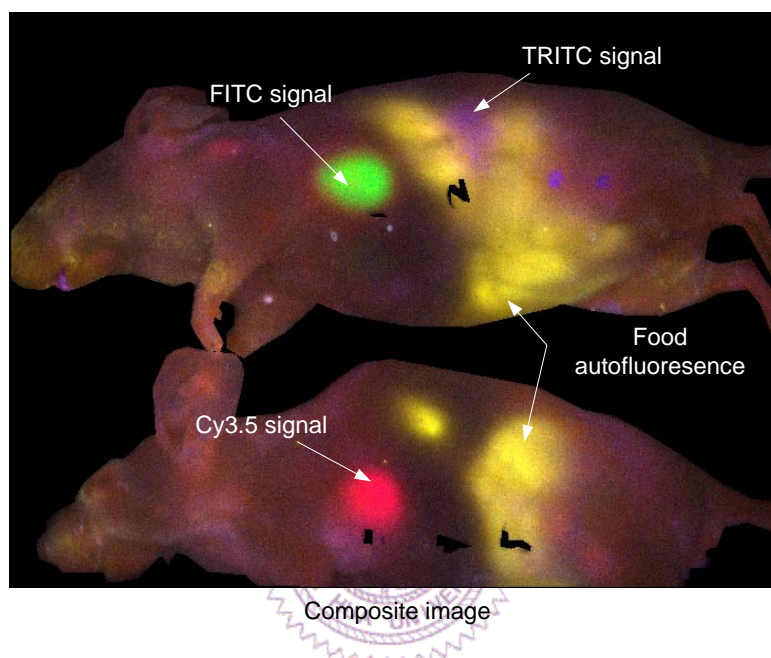
Figure 4.16. The composite image of the unmixed signals obtained by CAMNS-PI with pseudocolor, which correspond to three unmixed fluorophore signals and one food autofluorescence.

to handle volume maximization (which is nonconvex), simulation results match with our intuitive expectation that volume maximization (done by heuristic approach) can exhibit better resistance against the model mismatch.

We have carried out a number of simulations using different sets of image data, and have demonstrated that the proposed convex analysis based nBSS methods are promising, in terms of visual inspection and also in terms of sum-square-error separation performance measure. Other methods such as nICA and NMF were also compared to demonstrate the effectiveness of the proposed methods. In addition to the simulation results, we have conducted real data experiments using optical imaging data. In practical applications where the true number of sources is usually unknown, some modifications of the proposed nBSS method are made such that it can be applied even when model order mismatch occurs. The experimental results of our modified nBSS method are promising, and further demonstrated its superior applicability.
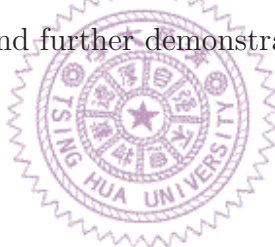
Chapter 5

Convex Analysis for Hyperspectral Unmixing
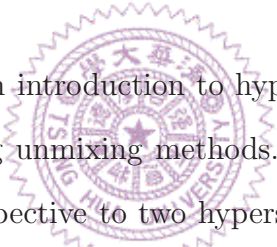
In this chapter, we first give an introduction to hyperspectral imaging, its potential applications, and some existing unmixing methods. We then provide a new convex analysis and optimization perspective to two hyperspectral unmixing problems that follow the intuitive ideas from the Winter's [43] and Craig's [45] works respectively. The relation between the two hyperspectral unmixing optimization problems is established when there exist pure pixels in the data. We also show how these two problems can be conveniently handled by alternating linear programming. Finally, some Monte Carlo simulations and real data experiments are presented to demonstrate the efficacy of the proposed methods. Throughout this chapter, we will assume that (A1), (A2), and (A5) are satisfied.

5.1   Introduction to Hyperspectral Imaging

Hyperspectral remote sensing [67, 68] is a crucial technique for the identification of disparate material substances from observed spectra, and has been utilized for plan-

etary exploration [69, 70] to analyze the composition and mineralogy of an observed planet in the solar system, e.g., Mars. Hyperspectral imaging also has a wide range of applications to the Earth, such as terrain classification, agricultural monitoring, environmental monitoring, and military surveillance [9, 47, 71, 72]. When a hyperspectral sensor explores a scene of interest where N unknown substances are involved over M spectral bands, due to low spatial resolution of the sensor used, each pixel of the observed spectra usually comprise multiple spectra from disparate materials. This physical phenomenon can be described by the $M \times N$ linear mixing model in (2.1); that is,

$$\mathbf{x}[n] = \sum_{i=1}^{N} \mathbf{a}_i s_i[n], \qquad n = 1, \ldots, L$$

where $\mathbf{x}[n] \in \mathbb{R}^M$ is the nth observed pixel vector, $\mathbf{a}_1, \ldots, \mathbf{a}_N$ denotes the spectral signatures (or endmembers), and $s_1[n], \ldots, s_N[n]$ are fractional abundances. Figure 5.1 illustrates the linear spectral mixing model for hyperspectral imaging, where each observed pixel $\mathbf{x}[n]$ is a linear combination of endmember signatures $\mathbf{a}_1, \ldots, \mathbf{a}_N$ weighted by their abundance fractions $s_1[n], \ldots, s_N[n]$.
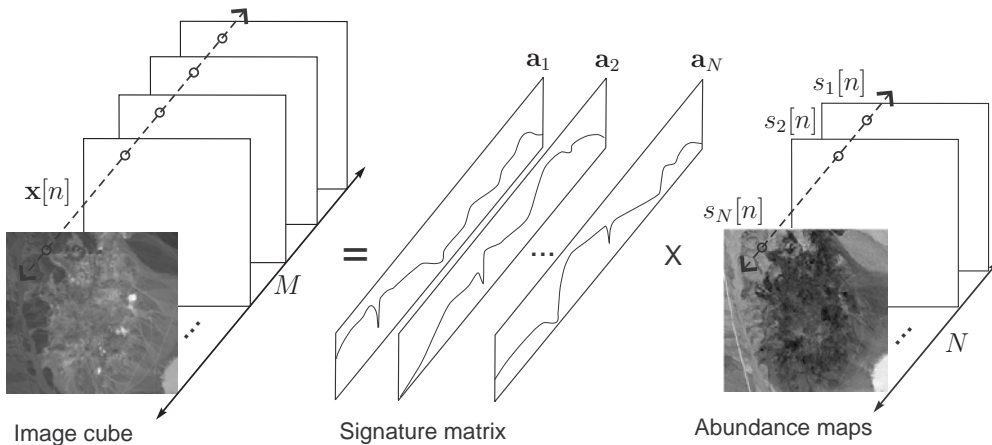
Figure 5.1. An illustration of the linear mixing model for hyperspectral imaging.

Hyperspectral unmixing [15, 20, 43, 44, 45, 73, 74, 75, 76, 77, 78, 79, 80, 81, 82, 83, 84, 85, 86] is a procedure to decompose the measured spectrum of an observed scene $\mathbf{x}[1], \ldots, \mathbf{x}[L]$ into a collection of endmembers $\mathbf{a}_1, \ldots, \mathbf{a}_N$ and their corresponding proportions (or abundances) $\mathbf{s}[1], \ldots, \mathbf{s}[L]$. It is essential in identifying individual materials from a hyperspectral scene. Certainly, some assumptions

(A1) All the abundance fractions are non-negative, i.e., $s_i[n] \geq 0$ for all i and n.

(A2) $\min\{L, M\} \geq N$ and $\mathbf{a}_1, \ldots, \mathbf{a}_N$ are linearly independent.

(A5) Sum of abundance fractions is equal to unity, i.e., $\sum_{i=1}^{N} s_i[n] = 1$ for all n.

are made in this chapter [9, 47, 71, 72]. This hyperspectral unmixing problem has a lot in common with nBSS problems.

In hyperspectral unmixing, basically there are three major processes, namely dimension reduction, endmember extraction, and the inversion process. Dimension reduction is useful for complexity reduction of the subsequent endmember extraction and inversion process. Principal component analysis (PCA) [74] and maximum noise fraction (MNF) [75] are typical dimension reduction algorithms. However, accurate estimation of the number of dimensions that can truly represent the data space still remain a challenging task, for which some model order estimation methods have been developed, for instance, virtual dimensionality (VD) [76] and hyperspectral signal identification by minimum error (HySime) [77]. Endmember extraction is to determine the endmembers that contribute to the measured spectra. A number of endmember extraction algorithms have been reported, e.g., pixel purity index (PPI) [78], N-finder (N-FINDR) [43, 44], vertex component analysis (VCA) [79], and convex cone analysis (CCA) [80]. Finally, the inversion process is to estimate the abundances associated with the endmember estimates. For instance, fully constrained least squares (FCLS) [81] is an effective algorithm for estimating the abundances. Nevertheless, there have been interesting unmixing methods that are capable of determining end-

members and abundances simultaneously, such as alternating projected subgradients (APS) [20], iterated constrained endmembers (ICE) [82], non-negative matrix factorization (NMF) [15, 83], joint Bayesian approach (JBA) [84], minimum volume transform (MVT) [45], and minimum volume simplex analysis (MVSA) [85].

Existing hyperspectral unmixing algorithms can be classified into two groups, between which the major distinction lies in whether pure pixels (i.e., pixels that are fully contributed from only one endmember) exist for all endmembers in the given data set or not. Such pure pixel assumption is conceptually the same as the local dominance assumption:

(A3) For each $i \in \{1, \ldots, N\}$, there exists an (unknown) index ℓ_i such that $\mathbf{x}[\ell_i] = \mathbf{a}_i$ for $i = 1, \ldots, N$.

A number of endmember extraction algorithms, such as PPI, N-FINDR and VCA, adopt the assumption of existence of pure pixels in the observed data set. Simply speaking, those algorithms attempt to search for the purest observed pixels over the data set as the endmember estimates, and are usually followed by FCLS to complete hyperspectral unmixing. PPI [78] projects all the observed pixels onto randomly generated unit-norm vectors and counts the number of times (i.e., scores) of the event that the value of each projected pixel reaches an extreme value (either minimum or maximum projected value). Then the purest pixels are identified as those pixels with the highest scores. N-FINDR [43] is based on a criterion that the volume of a simplex formed by the purest pixels is maximum, and fulfills this criterion by inflating the simplex inside the data set. VCA [79] iteratively projects the data onto a vector orthogonal to the subspace spanned by all the obtained endmember estimates before the current iteration, and identifies a new endmember as the one with the extreme value of the projected data. However, for the case of highly mixed data, the pure-pixel assumption may be seriously violated.

Hyperspectral unmixing algorithms that do not require the pure-pixel assump-

tion (A3) would be appropriate for highly mixed data. Examples of such algorithms are CCA, APS, ICE, NMF, JBA, MVT, and MVSA. CCA [80] determines the endmembers by searching for the boundary points of a convex cone constructed from the observed spectra. APS [20] is an alternating projected subgradient approach to solving a least squares problem, through the use of a regularization parameter that controls the difference between each target pixel of the abundances and its neighbors. ICE [82] uses quadratic programming to solve a least squares problem with a regularized term added to the objective function to limit the sum of the variances of the simplex vertices. NMF [15] was originally proposed for object recognition and has been recently applied to hyperspectral unmixing [83]. It basically decomposes the observation matrix into a product of two non-negative matrices, one serving as the endmember estimates while the other serving as the abundance estimates, whereas it suffers from the non-unique decomposition problem. To provide a more reliable decomposition in hyperspectral unmixing, a variant of NMF, called minimum volume constrained NMF (MVC-NMF) [86], has been proposed. JBA [84] estimates the endmembers by generating the posterior distribution of abundances and endmember parameters under a hierarchical Baysian model that assumes conjugate prior distributions for these parameters. Moreover, Craig [45] reported an unmixing criterion based on the belief that the vertices of a minimum-volume simplex enclosing all the observed pixels should serve as a high-fidelity estimate of the endmembers. To find such a simplex, Craig suggested a method (i.e., MVT) that begins with a simplex of large volume and then literally moves the faces of the simplex in toward the data cloud. However, MVT may be computationally intractable when dealing with a large amount of observed pixels. MVSA [85] considers Craig's criterion for hyperspectral unmixing. It uses sequential quadratic programming to solve non-convex unmixing problem with the results of VCA as initial points. However, MVSA can not work for the data with a large amount of observed pixels.

5.2 Convex Analysis to Hyperspectral Unmixing Problems

We now apply convex analysis to the nBSS problem [the model in (2.1) with assumptions (A1), (A2) and (A5)]. Due to the full additivity condition of the abundance vectors [(A5)], one can immediately infer that

$$\mathbf{x}[n] \in \mathrm{aff}\{\mathbf{a}_1, \ldots, \mathbf{a}_N\}, \ \forall \ n. \tag{5.1}$$

Like the results presented in Lemma 1 (in Chapter 4), we can recover the affine hull of $\mathbf{a}_1, \ldots, \mathbf{a}_N$ from the given observed pixels $\mathbf{x}[1], \mathbf{x}[2], \ldots, \mathbf{x}[L]$, as stated in the following lemma:

Lemma 8 *Under* (A2) *and* (A5)*, the observed pixel affine hull is equivalent to the endmember affine hull; that is,*

$$\mathrm{aff}\{\mathbf{x}[1], \ldots, \mathbf{x}[L]\} = \mathrm{aff}\{\mathbf{a}_1, \ldots, \mathbf{a}_N\}. \tag{5.2}$$

Since $\mathbf{a}_1, \ldots, \mathbf{a}_N$ are linearly independent [as assumed in (A2)], the endmember affine hull $\mathrm{aff}\{\mathbf{a}_1, \ldots, \mathbf{a}_N\}$ can be represented by

$$\mathrm{aff}\{\mathbf{a}_1, \ldots, \mathbf{a}_N\} = \left\{ \ \mathbf{x} = \mathbf{C}_e \boldsymbol{\alpha} + \mathbf{d}_e \ \middle| \ \boldsymbol{\alpha} \in \mathbb{R}^{N-1} \ \right\} \triangleq \mathcal{A}(\mathbf{C}_e, \mathbf{d}_e) \tag{5.3}$$

for some $(\mathbf{C}_e, \mathbf{d}_e) \in \mathbb{R}^{M \times (N-1)} \times \mathbb{R}^M$ and $\mathrm{rank}(\mathbf{C}_e) = N - 1$. From Lemma 8 (in Chapter 4) and (5.3), the affine hull parameter pair $(\mathbf{C}_e, \mathbf{d}_e)$ for both $\mathrm{aff}\{\mathbf{a}_1, \ldots, \mathbf{a}_N\}$ and $\mathrm{aff}\{\mathbf{x}[1], \ldots, \mathbf{x}[L]\}$ can be estimated through the affine set fitting (as presented

in Proposition 1 (in Chapter 4)) as follows:

$$\mathbf{d}_e = \frac{1}{L} \sum_{n=1}^{L} \mathbf{x}[n], \tag{5.4}$$

$$\mathbf{C}_e = [\, \boldsymbol{q}_1(\mathbf{U}\mathbf{U}^T), \boldsymbol{q}_2(\mathbf{U}\mathbf{U}^T), \dots, \boldsymbol{q}_{N-1}(\mathbf{U}\mathbf{U}^T) \,], \tag{5.5}$$

where $\mathbf{U} = [\, \mathbf{x}[1] - \mathbf{d}, \dots, \mathbf{x}[L] - \mathbf{d}_e \,] \in \mathbb{R}^{M \times L}$.

Then, due to $\mathbf{x}[n] \in \mathcal{A}(\mathbf{C}_e, \mathbf{d}_e)$, we can write its affine representation as

$$\mathbf{x}[n] = \mathbf{C}_e \tilde{\mathbf{x}}[n] + \mathbf{d}_e, \tag{5.6}$$

where $\tilde{\mathbf{x}}[n]$ is the inverse image of $\mathbf{x}[n]$ under (5.6), i.e.,

$$\tilde{\mathbf{x}}[n] = \mathbf{C}_e^{\dagger}(\mathbf{x}[n] - \mathbf{d}_e) \in \mathbb{R}^{N-1}. \tag{5.7}$$

The affinely transformed data $\tilde{\mathbf{x}}[1], \dots, \tilde{\mathbf{x}}[L]$ can be thought of as the dimension-reduced pixels. It follows by substituting (2.1) into (5.7) that

$$\tilde{\mathbf{x}}[n] = \sum_{j=1}^{N} s_j[n] \mathbf{C}_e^{\dagger} \mathbf{a}_j - \mathbf{C}_e^{\dagger} \mathbf{d}_e. \tag{5.8}$$

Since $\sum_{j=1}^{N} s_j[n] = 1$ [(A5)], the dimension-reduced pixels $\tilde{\mathbf{x}}[n]$ can be expressed as

$$\tilde{\mathbf{x}}[n] = \sum_{j=1}^{N} s_j[n](\mathbf{C}_e^{\dagger} \mathbf{a}_j - \mathbf{C}_e^{\dagger} \mathbf{d}_e) = \sum_{j=1}^{N} s_j[n] \boldsymbol{\alpha}_j, \tag{5.9}$$

where

$$\boldsymbol{\alpha}_j = \mathbf{C}_e^{\dagger}(\mathbf{a}_j - \mathbf{d}_e) \in \mathbb{R}^{N-1} \tag{5.10}$$

is the jth dimension-reduced endmember. The formulation given by (5.9) not only reduces the computational complexity of the subsequent processing steps, but also

enables us to apply the simplex geometry concept to the dimension-reduced pixels $\tilde{\mathbf{x}}[1], \ldots, \tilde{\mathbf{x}}[L]$, as stated in the following lemma.

Lemma 9 (Simplex geometry) *Under (A1), (A2) and (A5),*

$$\tilde{\mathbf{x}}[n] \in \text{conv}\{\boldsymbol{\alpha}_1, \ldots, \boldsymbol{\alpha}_N\} \subset \mathbb{R}^{N-1}, \ \forall n \tag{5.11}$$

and $\text{conv}\{\boldsymbol{\alpha}_1, \ldots, \boldsymbol{\alpha}_N\}$ *is a simplex.*

The proof of Lemma 9 is given in Appendix B.1.

Now, an interesting question is that how we can exploit simplex geometry to estimate $\boldsymbol{\alpha}_1, \ldots, \boldsymbol{\alpha}_N$ from $\tilde{\mathbf{x}}[1], \ldots, \tilde{\mathbf{x}}[L]$. The idea from Winter's work [43] (or Craig's work [45]) for hyperspectral unmixing that uses maximum (or minimum) volume simplex fitting approach could be adopted here. Figure 5.2 illustrates simplex geometry for the case of $N = 3$, where the data cloud is confined by the true simplex (solid-line triangle) $\text{conv}\{\boldsymbol{\alpha}_1, \ldots, \boldsymbol{\alpha}_N\}$, and the long dashed-line triangle $\text{conv}\{\boldsymbol{\nu}_1, \ldots, \boldsymbol{\nu}_N\}$ and short dashed-line triangle $\text{conv}\{\boldsymbol{\beta}_1, \ldots, \boldsymbol{\beta}_N\}$ are the possible solutions for Winter's and Craig's unmixing criteria, respectively.

In the ensuing development, we will formulate two optimization problems for hyperspectral unmixing using Winter's and Craig's unmixing criteria, and derive the relation between them under a certain condition.

5.2.1 Maximum Volume Simplex Fitting

Based on Winter's unmixing criterion [43] that determines the endmembers by identifying the vertices of the maximum volume simplex within the set of the dimension-reduced pixels, the unmixing problem of finding such a maximum volume simplex can
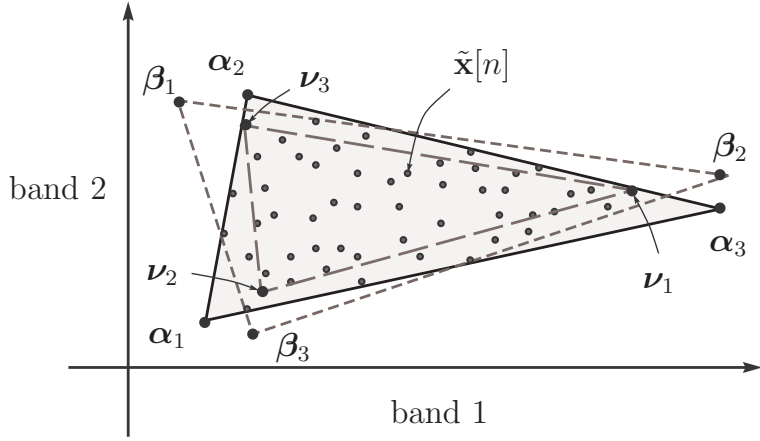
Figure 5.2. Scatter plot of the dimension-reduced pixels for $N = 3$, illustrating the Winter's and Craig's unmixing problems for hyperspectral unmixing.

be formulated as an optimization problem as shown below:

$$
\begin{aligned}
\max_{\boldsymbol{\nu}_1,\ldots,\boldsymbol{\nu}_N \in \mathbb{R}^{N-1}} \quad & V(\boldsymbol{\nu}_1,\ldots,\boldsymbol{\nu}_N) \\
\text{s.t.} \quad & \boldsymbol{\nu}_i \in \text{conv}\{\tilde{\mathbf{x}}[1],\ldots,\tilde{\mathbf{x}}[L]\}, \ \forall \ i = 1,\ldots,N,
\end{aligned}
\tag{5.12}
$$

where $V(\boldsymbol{\nu}_1,\ldots,\boldsymbol{\nu}_N)$ is the volume of the simplex $\text{conv}\{\boldsymbol{\nu}_1,\ldots,\boldsymbol{\nu}_N\}$ defined as in (4.28).

Let us consider the endmember identifiability of Winter's unmixing criterion, that is, a condition under which the optimal solution of (5.12) is identical to $\{\boldsymbol{\alpha}_1,\ldots,\boldsymbol{\alpha}_N\}$. Consider the pure pixel assumption [consequence of (A3)] that for each $i \in \{1,\ldots,N\}$, there exists an (unknown) index ℓ_i such that $\tilde{\mathbf{x}}[\ell_i] = \boldsymbol{\alpha}_i$ for $i = 1,\ldots,N$ (by 5.9). Though the pure pixel assumption has been frequently employed in pure-pixel based unmixing methods [43,78,79], the endmember identifiability is not mathematically analyzed and studied yet. In the following theorem, we show that pure pixel assumption is a sufficient and necessary endmember identifiability condition of Winter's unmixing criterion:

Theorem 4 (Endmember identifiability of Winter's unmixing criterion) *The optimal solution of (5.12) is uniquely given by $\boldsymbol{\alpha}_1, \ldots, \boldsymbol{\alpha}_N$ if and only if (A1) − (A3) and (A5) hold.*

The proof of Theorem 4 is given in Appendix B.2.

For ease of algorithm development for problem (5.12), an explicit form of (5.12) is given as follows. By (3.3), (4.28), and letting $\overline{\mathbf{X}} = [\ \tilde{\mathbf{x}}[1], \ldots, \tilde{\mathbf{x}}[L]\ ] \in \mathbb{R}^{(N-1) \times L}$, problem (5.12) can be expressed as

$$
\begin{aligned}
\max_{\substack{\boldsymbol{\nu}_i \in \mathbb{R}^{N-1} \\ \boldsymbol{\theta}_1, \ldots, \boldsymbol{\theta}_N \in \mathbb{R}^L}} \quad & |\det(\boldsymbol{\Delta}(\boldsymbol{\nu}_1, \ldots, \boldsymbol{\nu}_N))| \\
\text{s.t.} \quad & \boldsymbol{\nu}_i = \overline{\mathbf{X}}\boldsymbol{\theta}_i, \quad \boldsymbol{\theta}_i \succeq \mathbf{0}, \quad \mathbf{1}_L^T \boldsymbol{\theta}_i = 1, \ \forall\ i = 1, \ldots, N,
\end{aligned}
\tag{5.13}
$$

where $\boldsymbol{\Delta}(\boldsymbol{\nu}_1, \ldots, \boldsymbol{\nu}_N) \in \mathbb{R}^{N \times N}$ is defined as in (4.29). Problem (5.13) is nonconvex since its objective function is nonconvex. Nevertheless, the constraints are affine (or convex). The method to solve this problem will be presented in Section 5.3.

5.2.2 Minimum Volume Simplex Fitting

We now turn our attention to Craig's unmixing criterion [45] that does not need pure pixels. The criterion finds endmembers by the vertices of the minimum-volume simplex enclosing all the dimension-reduced pixels. The problem of finding such a minimum-volume simplex has been considered in computational geometry [87, 88], where the existing algorithms are combinatorial in nature and could be too complex to practically run for $N > 4$. Here, we formulate the unmixing problem as an optimization problem as follows:

$$
\begin{aligned}
\min_{\boldsymbol{\beta}_1, \ldots, \boldsymbol{\beta}_N} \quad & V(\boldsymbol{\beta}_1, \ldots, \boldsymbol{\beta}_N) \\
\text{s.t.} \quad & \tilde{\mathbf{x}}[n] \in \text{conv}\{\boldsymbol{\beta}_1, \ldots, \boldsymbol{\beta}_N\}, \ \forall\ n = 1, \ldots, L,
\end{aligned}
\tag{5.14}
$$

69

which enables us to utilize optimization skills to handle the minimum volume simplex fitting problem (as will see in Section 5.3).

Following the proof in Theorem 4, the endmember identifiability of Craig's unmixing criterion can also be proven under the pure-pixel assumption (see Appendix B.3 for the proof):

Theorem 5 (Endmember identifiability of Craig's unmixing criterion) *Under (A1)− (A3) and (A5), the optimal solution of (5.14) is uniquely given by $\boldsymbol{\alpha}_1, \ldots, \boldsymbol{\alpha}_N$.*

It should be pointed out that Theorem 5 provides a sufficient identifiability condition, but not a necessary one. We found that accurate endmember identification could still be possible in the absence of pure pixels, by our experience. So far our conjecture is that if there exist pixels that are close to pure pixels within some amount of tolerance, there is a good chance for Craig's unmixing criterion to achieve accurate endmember identification.

Summarizing Theorem 4 and Theorem 5, we can readily conclude that

Corollary 1 (Equivalence of Winter's and Craig's unmixing criteria) *Suppose that there exist at least one pure pixel per endmember in the data set [(A5)]. Then, problems (5.12) and (5.14) can identically yield the true dimension-reduced endmembers $\boldsymbol{\alpha}_1, \ldots, \boldsymbol{\alpha}_N$.*

Again, we formulate an explicit form of (5.14) for ease of algorithm development. Consider an alternative expression of the cost function in (5.14) given by [57]

$$V(\boldsymbol{\beta}_1, \ldots, \boldsymbol{\beta}_N) = \frac{|\det(\mathbf{B})|}{(N-1)!},$$
(5.15)

where

$$\mathbf{B} = [\ \boldsymbol{\beta}_1 - \boldsymbol{\beta}_N, \ldots, \boldsymbol{\beta}_{N-1} - \boldsymbol{\beta}_N\ ] \in \mathbb{R}^{(N-1)\times(N-1)}.$$
(5.16)

Moreover, any dimension-reduced pixel $\tilde{\mathbf{x}}[n] \in \text{conv}\{\boldsymbol{\beta}_1, \ldots, \boldsymbol{\beta}_N\}$ can be represented

70

by

$$\tilde{\mathbf{x}}[n] = \sum_{i=1}^{N} s_i[n]\boldsymbol{\beta}_i = \boldsymbol{\beta}_N + \mathbf{B}\mathbf{s}'[n], \qquad (5.17)$$

where $\mathbf{s}'[n] = (s_1[n], \ldots, s_{N-1}[n])^T \succeq \mathbf{0}$ and $s_N[n] = 1 - \mathbf{1}_{N-1}^T\mathbf{s}'[n] \geq 0$. Therefore, problem (5.14) is equivalent to

$$\min_{\substack{\mathbf{B},\ \boldsymbol{\beta}_N, \\ \mathbf{s}'[1],\ldots,\mathbf{s}'[L]}} \quad |\det(\mathbf{B})| \qquad (5.18a)$$

$$\text{s.t.} \quad \mathbf{s}'[n] \succeq \mathbf{0}, \ \mathbf{1}_{N-1}^T\mathbf{s}'[n] \leq 1, \qquad (5.18b)$$

$$\tilde{\mathbf{x}}[n] = \boldsymbol{\beta}_N + \mathbf{B}\mathbf{s}'[n], \ \forall \ n = 1, \ldots, L. \qquad (5.18c)$$

Problem (5.18) is nonconvex. While the nonconvexity of the objective function $|\det(\mathbf{B})|$ is an obstacle, the nonlinear equality constraints in (5.18c) impose additional difficulty.

We propose a reformulation of (5.18) where the original nonconvex constraints are transformed into convex constraints. Consider the following one-to-one mappings of the optimization variables:

$$\mathbf{H} = \mathbf{B}^{-1} \in \mathbb{R}^{(N-1)\times(N-1)}, \qquad (5.19a)$$

$$\mathbf{g} = \mathbf{B}^{-1}\boldsymbol{\beta}_N \in \mathbb{R}^{N-1}. \qquad (5.19b)$$

Then $\mathbf{s}'[n]$ can be represented by

$$\mathbf{s}'[n] = \mathbf{B}^{-1}(\tilde{\mathbf{x}}[n] - \boldsymbol{\beta}_N) = \mathbf{H}\tilde{\mathbf{x}}[n] - \mathbf{g}. \qquad (5.20)$$

71

Substituting (5.19) and (5.20) into (5.18), we obtain an equivalent problem of (5.18)

$$
\begin{aligned}
\max_{\mathbf{H},\ \mathbf{g}} \quad & |\det(\mathbf{H})| \\
\text{s.t.} \quad & \mathbf{H}\tilde{\mathbf{x}}[n] - \mathbf{g} \succeq \mathbf{0}, \\
& \mathbf{1}_{N-1}^{T}(\mathbf{H}\tilde{\mathbf{x}}[n] - \mathbf{g}) \leq 1,\ \forall\ n = 1, \ldots, L,
\end{aligned}
\tag{5.21}
$$

in which all constraints are now linear (and convex). Again, problem (5.21) is still nonconvex since its objective function is nonconvex.

5.3 Alternating Linear Programming Approaches

This section presents an alternating optimization approach to the non-convex optimization problems (5.13) and (5.21), named alternating volume maximization (AV-MAX) and alternating volume minimization (AVMIN), respectively. The idea is motivated by the cofactor expansion [57]. In the ensuing development, we will demonstrate how we use such an idea to tackle these two unmixing problems (5.13) and (5.21).

5.3.1 Alternating Volume Maximization

Now, we focus on handling the optimization problem in (5.13). Consider the cofactor expansion for $\det(\boldsymbol{\Delta}(\boldsymbol{\nu}_1, \ldots, \boldsymbol{\nu}_N))$ as follows:

$$
\det(\boldsymbol{\Delta}(\boldsymbol{\nu}_1, \ldots, \boldsymbol{\nu}_N)) = \mathbf{b}_j^T \boldsymbol{\nu}_j + (-1)^{N+j}\det(\boldsymbol{\mathcal{V}}_{Nj}),
\tag{5.22}
$$

where $\mathbf{b}_j = [(-1)^{i+j}\det(\boldsymbol{\mathcal{V}}_{ij})]_{i=1}^{N-1} \in \mathbb{R}^{N-1}$ and the matrix $\boldsymbol{\mathcal{V}}_{ij} \in \mathbb{R}^{(N-1)\times(N-1)}$ is a submatrix of $\boldsymbol{\Delta}(\boldsymbol{\nu}_1, \ldots, \boldsymbol{\nu}_N)$ with the ith row and jth column removed [57]. It is apparent from (5.22) that $\det(\boldsymbol{\Delta}(\boldsymbol{\nu}_1, \ldots, \boldsymbol{\nu}_N))$ is affine in each $\boldsymbol{\nu}_j$. Hence, we consider the partial maximization of (5.13) with respect to $\boldsymbol{\nu}_j$ and $\boldsymbol{\theta}_j$, while fixing $\boldsymbol{\nu}_i$ and $\boldsymbol{\theta}_i$

for $i \neq j$; that is,

$$\max_{\boldsymbol{\nu}_j \in \mathbb{R}^{N-1}, \boldsymbol{\theta}_j \in \mathbb{R}^L} \quad \left| \mathbf{b}_j^T \boldsymbol{\nu}_j + (-1)^{N+j} \det(\boldsymbol{\mathcal{V}}_{Nj}) \right| \tag{5.23}$$
$$\text{s.t.} \quad \boldsymbol{\nu}_j = \overline{\mathbf{X}} \boldsymbol{\theta}_j, \quad \boldsymbol{\theta}_j \succeq \mathbf{0}, \quad \mathbf{1}_L^T \boldsymbol{\theta}_j = 1.$$

Problem (5.23) is still nonconvex due to the nonconvex objective function, but it can be solved in a globally optimal manner by breaking it into two LPs:

$$p^\star = \max_{\boldsymbol{\nu}_j \in \mathbb{R}^{N-1}, \boldsymbol{\theta}_j \in \mathbb{R}^L} \quad \mathbf{b}_j^T \boldsymbol{\nu}_j + (-1)^{N+j} \det(\boldsymbol{\mathcal{V}}_{Nj}) \tag{5.24}$$
$$\text{s.t.} \quad \boldsymbol{\nu}_j = \overline{\mathbf{X}} \boldsymbol{\theta}_j, \quad \boldsymbol{\theta}_j \succeq \mathbf{0}, \quad \mathbf{1}_L^T \boldsymbol{\theta}_j = 1,$$

and

$$q^\star = \min_{\boldsymbol{\nu}_j \in \mathbb{R}^{N-1}, \boldsymbol{\theta}_j \in \mathbb{R}^L} \quad \mathbf{b}_j^T \boldsymbol{\nu}_j + (-1)^{N+j} \det(\boldsymbol{\mathcal{V}}_{Nj}) \tag{5.25}$$
$$\text{s.t.} \quad \boldsymbol{\nu}_j = \overline{\mathbf{X}} \boldsymbol{\theta}_j, \quad \boldsymbol{\theta}_j \succeq \mathbf{0}, \quad \mathbf{1}_L^T \boldsymbol{\theta}_j = 1.$$

The optimal solution of (5.23) is chosen as that of (5.24) if $|p^\star| > |q^\star|$, and that of (5.25) if $|q^\star| > |p^\star|$. The partial maximization is conducted cyclically (i.e., $j := (j \text{ modulo } N) + 1$ at each iteration) until some stopping rule is satisfied.

Suppose that a solution $\boldsymbol{\nu}_1^\star, \ldots, \boldsymbol{\nu}_N^\star$, are obtained by cyclic maximization of (5.13). One can simply recover the endmember estimates by the affine transformation $\hat{\mathbf{a}}_i = \mathbf{C} \hat{\boldsymbol{\nu}}_i^\star + \mathbf{d}$ for all i, and estimate the associated abundance maps by FCLS [81] with the given $\boldsymbol{\nu}_1^\star, \ldots, \boldsymbol{\nu}_N^\star$ and $\tilde{\mathbf{x}}[1], \ldots, \tilde{\mathbf{x}}[L]$. In addition, to initialize the proposed AVMAX, we can find some feasible $\boldsymbol{\nu}_1, \ldots, \boldsymbol{\nu}_N$ by randomly selecting the N dimension-reduced pixels from $\tilde{\mathbf{x}}[1], \ldots, \tilde{\mathbf{x}}[L]$ (which are surely feasible points for the problem (5.13)).

The proposed AVMAX is summarized in Table 5.1. If the LP solver used is a primal-dual interior-point method [54, 55], then each LP problem in (5.24) or (5.25) can be solved practically with a worst-case computational complexity of $\mathcal{O}((N+L-$

$1)^{0.5}(N^3 + N(N + L - 1))) \simeq \mathcal{O}(NL^{1.5})$ if $L \gg N$. Moreover, the proposed AVMAX involves $2N$ LPs per iteration, implying that its worst-case computational complexity order is $\mathcal{O}(N^2 L^{1.5})$ per iteration.

5.3.2 Alternating Volume Minimization

We here present the alternating linear programming for the unmixing problem (5.21). The cofactor expansion for $\det(\mathbf{H})$ is as follows

$$\det(\mathbf{H}) = \sum_{j=1}^{N-1} (-1)^{i+j} h_{ij} \det(\boldsymbol{\mathcal{H}}_{ij}), \qquad (5.26)$$

for any $i = 1, \ldots, N - 1$, where h_{ij} is the (i, j)th entry of $\mathbf{H}$, and $\boldsymbol{\mathcal{H}}_{ij} \in \mathbb{R}^{(N-2) \times (N-2)}$ is a submatrix of $\mathbf{H}$ with the ith row and jth column removed [57]. Note that with a fixed $\boldsymbol{\mathcal{H}}_{ij}$, $\det(\mathbf{H})$ is a linear function of h_{ij}, $j = 1, 2, \ldots, N - 1$. Let us consider updating one row vector of $\mathbf{H}$ and one entry of $\mathbf{g}$ while fixing the other rows of $\mathbf{H}$ and the other entries of $\mathbf{g}$. Let $\mathbf{h}_i^T$ denote the ith row vector of $\mathbf{H}$, and g_i denote the ith entry of $\mathbf{g}$. The partial maximization of (5.21) with respect to $\mathbf{h}_i$ and g_i is given by

$$\max_{\mathbf{h}_i^T, \, g_i} \quad \left| \sum_{j=1}^{N-1} (-1)^{i+j} h_{ij} \det(\boldsymbol{\mathcal{H}}_{ij}) \right|$$

$$\text{s.t.} \quad 0 \le \mathbf{h}_i^T \tilde{\mathbf{x}}[n] - g_i \le 1 - \sum_{j \ne i} (\mathbf{h}_j^T \tilde{\mathbf{x}}[n] - g_j), \; \forall \, n = 1, \ldots, L. \qquad (5.27)$$

Note that the objective function in (5.27) is still nonconvex. However, the partial maximization problem in (5.27) can be solved in a globally optimal manner by break-

Table 5.1. A Summary of AVMAX for Hyperspectral Unmixing

Given	A convergence tolerance $\varepsilon > 0$, an endmember affine set characterization $(\mathbf{C}_e, \mathbf{d}_e)$, the dimension-reduced pixels $\tilde{\mathbf{x}}[n]$ for all n, and the number of endmembers N.
Step 1.	Obtain some feasible initial $\boldsymbol{\nu}_1, \dots, \boldsymbol{\nu}_N$ by randomly selecting the N dimension-reduced pixels from $\tilde{\mathbf{x}}[1], \dots, \tilde{\mathbf{x}}[L]$.
Step 2.	Set $j := 1$ and $\varrho := |\det(\boldsymbol{\Delta}(\boldsymbol{\nu}_1, \dots, \boldsymbol{\nu}_N))|$.

Step 3. Solve the LPs

$$p^\star = \max_{\boldsymbol{\nu}_j \in \mathbb{R}^{N-1}, \boldsymbol{\theta}_j \in \mathbb{R}^L} \quad \mathbf{b}_j^T \boldsymbol{\nu}_j + (-1)^{N+j} \det(\boldsymbol{\mathcal{V}}_{Nj})$$

$$\text{s.t.} \quad \boldsymbol{\nu}_j = \overline{\mathbf{X}} \boldsymbol{\theta}_j, \quad \boldsymbol{\theta}_j \succeq \mathbf{0}, \quad \mathbf{1}_L^T \boldsymbol{\theta}_j = 1,$$

and

$$q^\star = \min_{\boldsymbol{\nu}_j \in \mathbb{R}^{N-1}, \boldsymbol{\theta}_j \in \mathbb{R}^L} \quad \mathbf{b}_j^T \boldsymbol{\nu}_j + (-1)^{N+j} \det(\boldsymbol{\mathcal{V}}_{Nj})$$

$$\text{s.t.} \quad \boldsymbol{\nu}_j = \overline{\mathbf{X}} \boldsymbol{\theta}_j, \quad \boldsymbol{\theta}_j \succeq \mathbf{0}, \quad \mathbf{1}_L^T \boldsymbol{\theta}_j = 1,$$

and obtain their optimal solutions, denoted by $(\bar{\boldsymbol{\nu}}_j, \bar{\boldsymbol{\theta}}_j)$ and $(\underline{\boldsymbol{\nu}}_j, \underline{\boldsymbol{\theta}}_j)$, respectively.

Step 4.	If $|p^\star| > |q^\star|$, then update $(\boldsymbol{\nu}_j, \boldsymbol{\theta}_j) := (\bar{\boldsymbol{\nu}}_j, \bar{\boldsymbol{\theta}}_j)$. Otherwise, update $(\boldsymbol{\nu}_j, \boldsymbol{\theta}_j) := (\underline{\boldsymbol{\nu}}_j, \underline{\boldsymbol{\theta}}_j)$.
Step 5.	If $(j \text{ modulo } N) \neq 0$, then $j := j + 1$, and go to **Step 3**, else
	If $|\max\{|p^\star|, |q^\star|\} - \varrho|/\varrho < \varepsilon$, then $\boldsymbol{\nu}_j^\star = \boldsymbol{\nu}_j$ for all j.
	Otherwise, set $\varrho := \max\{|p^\star|, |q^\star|\}$, $j := 1$, and go to **Step 3**.
Step 6.	Obtain endmember estimates $\hat{\mathbf{a}}_j = \mathbf{C}_e \boldsymbol{\nu}_j^\star + \mathbf{d}_e$ for $j = 1, \dots, N$.
Step 7.	Recover the abundance vectors by FCLS [81] with the given $\boldsymbol{\nu}_1^\star, \dots, \boldsymbol{\nu}_N^\star$ and $\tilde{\mathbf{x}}[1], \dots, \tilde{\mathbf{x}}[L]$.

ing it into two LPs:

$$p^\star = \max_{\mathbf{h}_i^T,\, g_i} \quad \sum_{j=1}^{N-1} (-1)^{i+j} h_{ij} \det(\boldsymbol{\mathcal{H}}_{ij}) \tag{5.28}$$

$$\text{s.t.} \quad 0 \le \mathbf{h}_i^T \tilde{\mathbf{x}}[n] - g_i \le 1 - \sum_{j \ne i} (\mathbf{h}_j^T \tilde{\mathbf{x}}[n] - g_j), \ \forall\, n = 1, \ldots, L.$$

and

$$q^\star = \min_{\mathbf{h}_i^T,\, g_i} \quad \sum_{j=1}^{N-1} (-1)^{i+j} h_{ij} \det(\boldsymbol{\mathcal{H}}_{ij}) \tag{5.29}$$

$$\text{s.t.} \quad 0 \le \mathbf{h}_i^T \tilde{\mathbf{x}}[n] - g_i \le 1 - \sum_{j \ne i} (\mathbf{h}_j^T \tilde{\mathbf{x}}[n] - g_j), \ \forall\, n = 1, \ldots, L.$$

The optimal solution of (5.27), denoted by $((\mathbf{h}_i^T)^\star,\, g_i^\star)$, is chosen as the optimal solution of (5.28) if $|p^\star| > |q^\star|$, and that of (5.29) if $|q^\star| > |p^\star|$. This row-wise minimization is conducted cyclically (i.e., $i := (i \bmod (N-1)) + 1$ at each iteration) until some stopping rule is satisfied.

Suppose that a solution $(\mathbf{H}^\star, \mathbf{g}^\star)$ is obtained by cyclic maximization of (5.21). By (5.16) and (5.19) the dimension-reduced endmember estimates, denoted by $\widehat{\boldsymbol{\alpha}}_1, \ldots, \widehat{\boldsymbol{\alpha}}_N$, are obtained by

$$\widehat{\boldsymbol{\alpha}}_N = (\mathbf{H}^\star)^{-1} \mathbf{g}^\star, \tag{5.30}$$

$$[\widehat{\boldsymbol{\alpha}}_1, ..., \widehat{\boldsymbol{\alpha}}_{N-1}] = \widehat{\boldsymbol{\alpha}}_N \mathbf{1}_{N-1}^T + (\mathbf{H}^\star)^{-1}. \tag{5.31}$$

The endmember signatures can then be recovered by (5.10), i.e., $\widehat{\mathbf{a}}_i = \mathbf{C} \widehat{\boldsymbol{\alpha}}_i + \mathbf{d}$ for $i = 1, \ldots, N$. Furthermore, from (5.20), the abundance vectors can be estimated as

$$\widehat{\mathbf{s}}[n] = [\ \mathbf{s}'[n]^T \quad 1 - \mathbf{1}_{N-1}^T \mathbf{s}'[n]\ ]^T,$$

$$= [\ (\mathbf{H}^\star \tilde{\mathbf{x}}[n] - \mathbf{g}^\star)^T \quad 1 - \mathbf{1}_{N-1}^T (\mathbf{H}^\star \tilde{\mathbf{x}}[n] - \mathbf{g}^\star)\ ]^T, \ \forall\, n = 1, \ldots, L. \tag{5.32}$$

Therefore, the proposed AVMIN yields the estimates of the endmembers and abundances given by (5.30), (5.31), and (5.32) simultaneously without involving any inversion process.

To initialize the proposed AVMIN, a feasible $(\mathbf{H}, \mathbf{g})$ for problem (5.27) is needed. We can find one feasible $(\mathbf{H}, \mathbf{g})$ by solving the following feasibility problem:

$$
\begin{aligned}
\text{find} \quad & (\mathbf{H}, \mathbf{g}) \\
\text{s.t.} \quad & \mathbf{H}\tilde{\mathbf{x}}[n] - \mathbf{g} \succeq \mathbf{0}, \\
& \mathbf{1}_{N-1}^T (\mathbf{H}\tilde{\mathbf{x}}[n] - \mathbf{g}) \leq 1, \ \forall \ n = 1, \ldots, L,
\end{aligned}
\tag{5.33}
$$

which can also be implemented by LP.

The proposed AVMIN is summarized in Table 5.2. As in Section 5.3.1, if the LP solver used is a primal-dual interior-point method [55,54], each LP problem in (5.28) or (5.29) can be solved practically with a worst-case computational complexity of $\mathcal{O}(L^{0.5}(2LN + N^3)) \simeq \mathcal{O}(NL^{1.5})$ if $L \gg N$ [39]. Since the proposed AVMIN involves $2N$ LPs per iteration, its worst-case computational complexity order is $\mathcal{O}(N^2 L^{1.5})$ per iteration.

We summarize our perspective to hyperspectral unmixing by a signal processing flow chart in Figure 5.3.

5.4 Numerical Results

To demonstrate the efficacy of the proposed AVMAX and AVMIN, simulations for four different scenarios are presented in this section. In each scenario, the simulation results are obtained by performing 100 Monte Carlo runs. Section 5.4.1 presents some results for noiseless data with different purity levels. Section 5.4.2 presents the results for different number of endmembers. Sections 5.4.3 and 5.4.4 consider white and non-uniform noise scenarios for different SNRs, respectively. We also tested seven

Table 5.2. A Summary of AVMIN for Hyperspectral Unmixing

Given   A convergence tolerance $\varepsilon > 0$, an endmember affine set characterization $(\mathbf{C}_e, \mathbf{d}_e)$, the dimension-reduced pixels $\tilde{\mathbf{x}}[n]$ for all n, and the number of endmembers N.

Step 1.   Set $i := 1$ and $\varrho := |\det(\mathbf{H})|$. Obtain a feasible initial $(\mathbf{H}, \mathbf{g})$ by solving the LP feasibility problem in (5.33).

Step 2.   Solve the LPs

$$p^\star = \max_{\mathbf{h}_i^T,\, g_i} \quad \sum_{j=1}^{N-1} (-1)^{i+j} h_{ij} \det(\boldsymbol{\mathcal{H}}_{ij})$$
$$\text{s.t.} \quad 0 \le \mathbf{h}_i^T \tilde{\mathbf{x}}[n] - g_i \le 1 - \sum_{j \ne i} \mathbf{h}_j^T \tilde{\mathbf{x}}[n] + g_j, \ \forall\, n = 1, \ldots, L.$$

and

$$q^\star = \min_{\mathbf{h}_i^T,\, g_i} \quad \sum_{j=1}^{N-1} (-1)^{i+j} h_{ij} \det(\boldsymbol{\mathcal{H}}_{ij})$$
$$\text{s.t.} \quad 0 \le \mathbf{h}_i^T \tilde{\mathbf{x}}[n] - g_i \le 1 - \sum_{j \ne i} \mathbf{h}_j^T \tilde{\mathbf{x}}[n] + g_j, \ \forall\, n = 1, \ldots, L.$$

and obtain their optimal solutions, denoted by $(\bar{\mathbf{h}}_i^T, \bar{g}_i)$ and $(\underline{\mathbf{h}}_i^T, \underline{g}_i)$, respectively.

Step 3.   If $|p^\star| > |q^\star|$, then update $(\mathbf{h}_i^T, g_i) := (\bar{\mathbf{h}}_i^T, \bar{g}_i)$. Otherwise, update $(\mathbf{h}_i^T, g_i) := (\underline{\mathbf{h}}_i^T, \underline{g}_i)$.

Step 4.   If $(i \text{ modulo } (N-1)) \ne 0$, then $i := i+1$, and go to **Step 2**, else

  If $|\max\{|p^\star|, |q^\star|\} - \varrho|/\varrho < \varepsilon$, then $\mathbf{H}^\star = \mathbf{H}$ and $\mathbf{g}^\star = \mathbf{g}$.

  Otherwise, set $\varrho := \max\{|p^\star|, |q^\star|\}$, $i := 1$, and go to **Step 2**.

Step 5.   Calculate $\widehat{\boldsymbol{\alpha}}_N = (\mathbf{H}^\star)^{-1} \mathbf{g}^\star$ and $[\widehat{\boldsymbol{\alpha}}_1, ..., \widehat{\boldsymbol{\alpha}}_{N-1}] = \widehat{\boldsymbol{\alpha}}_N \mathbf{1}_{N-1}^T + (\mathbf{H}^\star)^{-1}$.

Step 6.   Obtain endmember estimates $\widehat{\mathbf{a}}_i = \mathbf{C}_e \widehat{\boldsymbol{\alpha}}_i + \mathbf{d}_e$ for $i = 1, ..., N$.

Step 7.   Recover the abundance vectors

$$\widehat{\mathbf{s}}[n] = [\ (\mathbf{H}^\star \tilde{\mathbf{x}}[n] - \mathbf{g}^\star)^T \quad 1 - \mathbf{1}_{N-1}^T (\mathbf{H}^\star \tilde{\mathbf{x}}[n] - \mathbf{g}^\star) \ ]^T$$

for $n = 1, ..., L$.
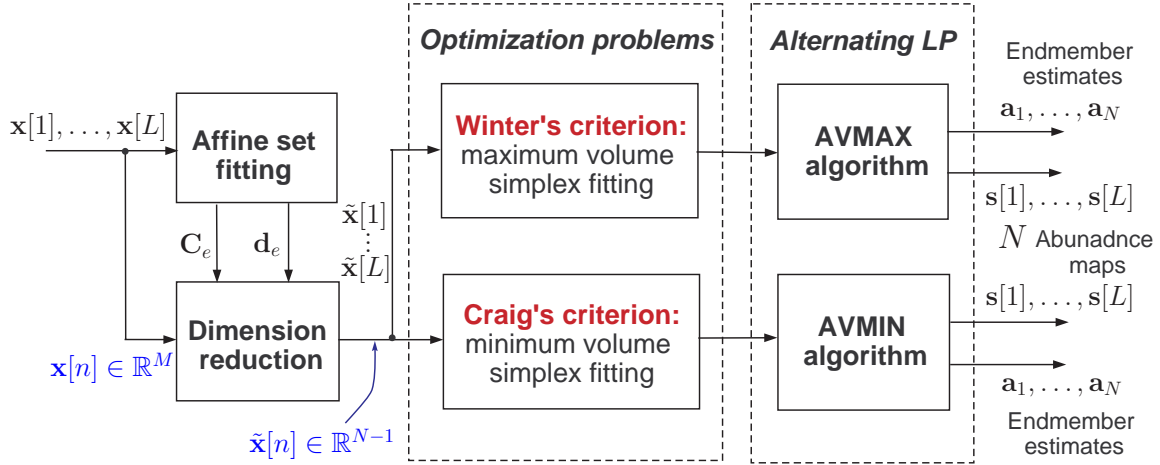
Figure 5.3. Signal processing flow chart of the proposed hyperspectral unmixing algorithms.

existing algorithms, N-FINDR [43], PPI [78], VCA [79], APS [20], MVC-NMF [86], MVSA [85], and ICE [82] for performance comparison. Note that the first three algorithms require the pure pixel assumption, while the other four do not.

The simulation settings for each unmixing algorithm under test are as follows. In PPI, the number of skewers (which is data dependent) was set to 1000 (beyond which no further performance improvements were noticeable in the simulations). The affine set fitting (presented in Section 5.2) was used for dimension reduction in N-FINDR, PPI, AVMAX and AVMIN. Since PPI, N-FINDR, and VCA are endmember extraction algorithms, the FCLS [81] was used to find their associated abundances. Hence, we termed them as PPI-FCLS, N-FINDR-FCLS, and VCA-FCLS, respectively. Since the operations of APS, MVC-NMF, and ICE are data dependent, the regularization parameters in APS, MVC-NMF, and ICE were set to the values between 0.01 and 0.0001 to ensure the best performance. The convergence accuracy for APS, MVC-NMF, and ICE was set to 10^{-6}, and the convergence tolerance in AVMAX and AVMIN was set to $\varepsilon = 10^{-7}$. It is to be mentioned that APS, MVC-NMF, ICE, and MVSA were initialized by the endmember and abundance estimates of VCA-FCLS.

Let $\hat{\mathbf{a}}_1, \ldots, \hat{\mathbf{a}}_N$ denote the endmembers estimates, and let $\boldsymbol{s}_1, \ldots, \boldsymbol{s}_N$ and $\hat{\boldsymbol{s}}_1, \ldots, \hat{\boldsymbol{s}}_N$

79

denote the true and estimated abundances, respectively, where $\boldsymbol{s}_i = [\, s_i[1], \ldots, s_i[L]\,]^T \in \mathbb{R}^L$ and $\hat{\boldsymbol{s}}_i = [\, \hat{s}_i[1], \ldots, \hat{s}_i[L]\,]^T \in \mathbb{R}^L$. The root-mean-square (rms) spectral angle distance between endmembers and their estimates was used as a performance measure [79]:

$$\phi_{en} = \min_{\boldsymbol{\pi} \in \Pi_N} \sqrt{\frac{1}{N} \sum_{i=1}^{N} \left[\arccos \left(\frac{\mathbf{a}_i^T \hat{\mathbf{a}}_{\pi_i}}{\|\mathbf{a}_i\| \|\hat{\mathbf{a}}_{\pi_i}\|} \right) \right]^2} \qquad (5.34)$$

where $\boldsymbol{\pi} = (\pi_1, \ldots, \pi_N)$, and $\Pi_N = \{\boldsymbol{\pi} \in \mathbb{R}^N \mid \pi_i \in \{1, 2, \ldots, N\},\ \pi_i \neq \pi_j \text{ for } i \neq j\}$ is the set of all the permutations of $\{1, 2, ..., N\}$. Similarly, the performance measure for the estimated abundances was

$$\phi_{ab} = \min_{\boldsymbol{\pi} \in \Pi_N} \sqrt{\frac{1}{N} \sum_{i=1}^{N} \left[\arccos \left(\frac{\boldsymbol{s}_i^T \hat{\boldsymbol{s}}_{\pi_i}}{\|\boldsymbol{s}_i\| \|\hat{\boldsymbol{s}}_{\pi_i}\|} \right) \right]^2}. \qquad (5.35)$$

It is clear that the smaller the values of ϕ_{en} and ϕ_{ab}, the better the performance of the unmixing algorithm. The performance measures defined in (5.34) and (5.35) themselves are optimal assignment problems due to $N!$ permutations $\boldsymbol{\pi}$, but it can be efficiently solved by Hungarian algorithm [1] [60].

As for the computational complexity comparison of the proposed AVMAX and AVMIN and the other seven unmixing methods, the computation time (in secs) of each algorithm (implemented in Matlab version 7.0) when executed in a desktop computer (equipped with Pentium 4 CPU 3.03GHz, 4GB RAM) was used as our computational complexity measure.

---

[1]A Matlab implementation is available at `http://si.utia.cas.cz/Tichavsky.html`.

5.4.1 Monte Carlo Simulations for Data with Various Purity Levels

Six endmembers (i.e., Alunite, Buddingtonite, Calcite, Copiapite, Kaolinite, and Muscovite) with 417 bands selected from the U.S. geological survey (USGS) library [89] [see Figure 5.4] were used to produce 1000 observed pixels (i.e., $N = 6$, $M = 417$, $L = 1000$). The corresponding abundances were generated following a Dirichlet distribution with $\boldsymbol{\mu} = (\mu_1, \ldots, \mu_N)^T = \frac{1}{N}\mathbf{1}_N$ [79], given by

$$D(\mathbf{s}, \boldsymbol{\mu}) = \frac{\prod_{i=1}^{N} \Gamma(\mu_i)}{\Gamma(\sum_{i=1}^{N} \mu_i)} \prod_{i=1}^{N} s_i^{\mu_i - 1} \tag{5.36}$$

where $\mathbf{s} = (s_1, \ldots, s_N)^T$, $0 \leq s_i \leq 1$, $\sum_{i=1}^{N} s_i = 1$ and $\Gamma(\cdot)$ denotes the Gamma function. Note that the expected value of the ith fraction s_i is $E[s_i] = \mu_i / \sum_{i=1}^{N} \mu_i$. The Dirichlet distribution of the abundances automatically enforces (A1) and (A5).
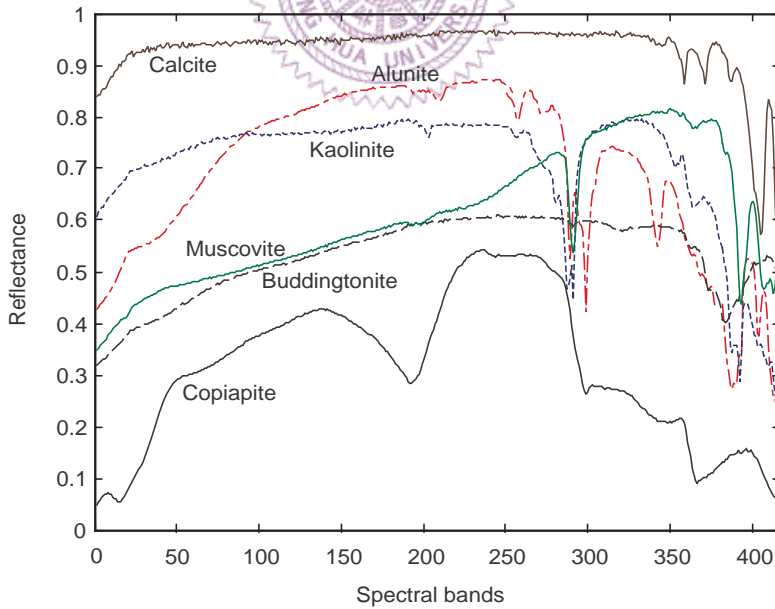
Figure 5.4. USGS library spectra of the six minerals: Alunite, Buddingtonite, Calcite, Copiapite, Kaolinite, and Muscovite.

To generate the observed data set with different purity levels, let us define a

purity measure for an observed pixel vector $\mathbf{x}[n]$, to quantify the domination of a single endmember in that pixel vector, as follows:

$$\rho_n = \frac{\|\mathbf{s}[n]\|}{\mathbf{1}_N^T \mathbf{s}[n]} = \|\mathbf{s}[n]\|. \tag{5.37}$$

The second equality is due to (A5). Note that $1/\sqrt{N} \le \rho_n \le 1$ and the purity of the observed pixel $\mathbf{x}[n]$ is higher for larger ρ_n. A set of L observed pixels $\mathbf{x}[n]$ with $\rho - 0.1 \le \rho_n \le \rho$ is called a data set with purity level of ρ (where $(0.1 + 1/\sqrt{N}) \le \rho \le 1$). The data set can be generated through the following steps.

(S1) Generate a set of $K = 10L$ observed pixels where the abundance vectors $\mathbf{s}[k]$ following a Dirichlet distribution, i.e.,

$$\Omega = \left\{ \mathbf{x}[k] = \mathbf{A}\mathbf{s}[k] \mid \mathbf{s}[k] \sim D(\mathbf{s}[k], \boldsymbol{\mu}), \ \forall k = 1, \ldots, K \right\},$$

and calculate the corresponding purity $\rho_k = \|\mathbf{s}[k]\|$ of each $\mathbf{x}[k]$ for all k.

(S2) Construct a set of observed pixels with purity level equal to ρ by randomly picking L observed pixels from Ω while satisfying $\rho_n \in [\rho - 0.1, \rho]$, i.e.,

$$\{\mathbf{x}[n] \mid \mathbf{x}[n] \in \Omega, \ \rho_n \in [\rho - 0.1, \rho], \ \forall n = 1, \ldots, L\}.$$

Note that the generated data for $\rho = 1$ includes some $\mathbf{x}[n]$ with $\rho_n \simeq 1$, i.e., highly pure pixels.

The average ϕ_{en} and ϕ_{ab} of the unmixing methods under test for different values of $\rho = 0.7, 0.75, \ldots, 1$ are shown in Figures 5.5 and 5.6, respectively. One can see from Figures 5.5 and 5.6 that all the algorithms performed better for higher purity level. That implies all the algorithms achieved almost perfect unmixing (i.e., $\phi_{en} = \phi_{ab} = 0$) for $\rho = 1$. The ICE, MVC-NMF, MVSA and AVMIN performed well

Table 5.3. The average computation time (secs) per realization of the various unmixing methods in the absence of noise (Section 5.4.1) and in the presence of noise (Section 5.4.3).

Scenarios	N-FINDR	PPI	VCA	APS	MVC-NMF	MVSA	ICE	AVMAX	AVMIN
No noise	3.35	3.23	3.06	40.70	64.54	4.08	81.37	15.79	54.79
With noise	3.37	3.42	5.62	31.55	54.57	17.11	96.95	15.20	47.34

even for lower purity levels, while the performance of N-FINDR-FCLS, PPI-FCLS, VCA-FCLS, APS, and AVMAX degraded significantly. In addition, the performance of the proposed AVMAX was very comparable to that of N-FINDR-FCLS, and the MVSA and proposed AVMIN outperformed all the other algorithms. The results not only validated equivalence of Winter's and Craig's unmixing criteria under pure pixel assumption [(A3)] (see Corollary 1), but also substantiated our conjecture that Craig's unmixing criterion can also achieve accurate endmember identification even when $\rho < 1$.

The average computation time (secs) per realization of each unmixing method for the noiseless case is shown in Table 5.3. From this table, one can observe that the average computation time spent by most of the pure-pixel based unmixing algorithms, such as N-FINDR-FCLS, PPI-FCLS, and VCA-FCLS, were less than that of the algorithms that do not require pure pixels. Among the algorithms that does not need the pure pixels, the proposed AVMIN spent less computation time than MVC-NMF and ICE, but more than APS and MVSA.

The complexity results in Table 5.3 indicate that the proposed AVMIN has relatively high complexity (though not the highest). As a future direction, the complexity of AVMIN may be reduced by making specialized LP algorithms, and by introducing a warm start for each LP in running the AVMIN.
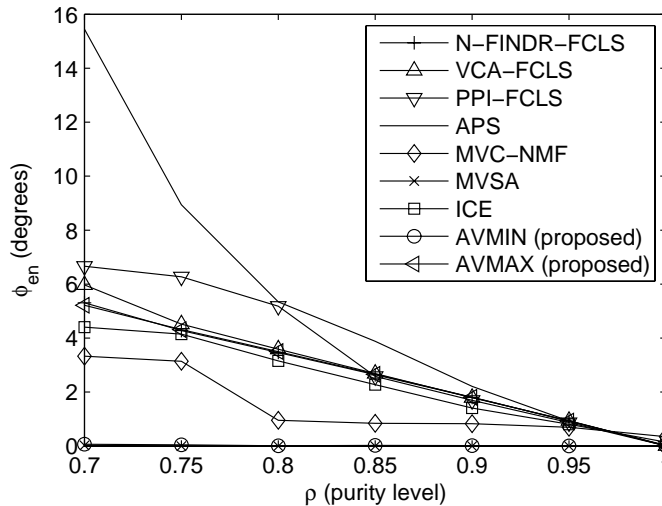
Figure 5.5. Simulation results of the endmember estimates obtained by the various algorithms under test for different purity levels (ϕ_{en}).
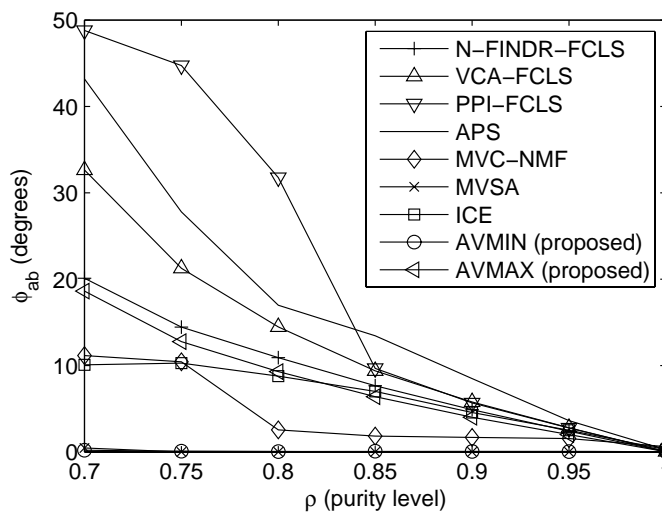
Figure 5.6. Simulation results of the abundance estimates obtained by the various algorithms under test for different purity levels (ϕ_{ab}).

5.4.2 Monte Carlo Simulations for Various Number of Endmembers

The synthetic data were generated in the same manner ($M = 417$ and $L = 1000$) as in Section 5.4.1, where the purity level was fixed as $\rho = 0.75$ and the N endmembers were randomly picked from USGS library [89].

The average ϕ_{en} and ϕ_{ab} of the unmixing methods for $N = 6, 8, ..., 14$ are shown in Figures 5.7 and 5.8, respectively. One can observe that the performance of the unmixing algorithms (except MVSA and AVMIN) slightly degraded as the number of endmembers increased. Specifically, MVSA and our AVMIN showed the best performance, and the PPI-FCLS was the worst one, among all the algorithms under test.
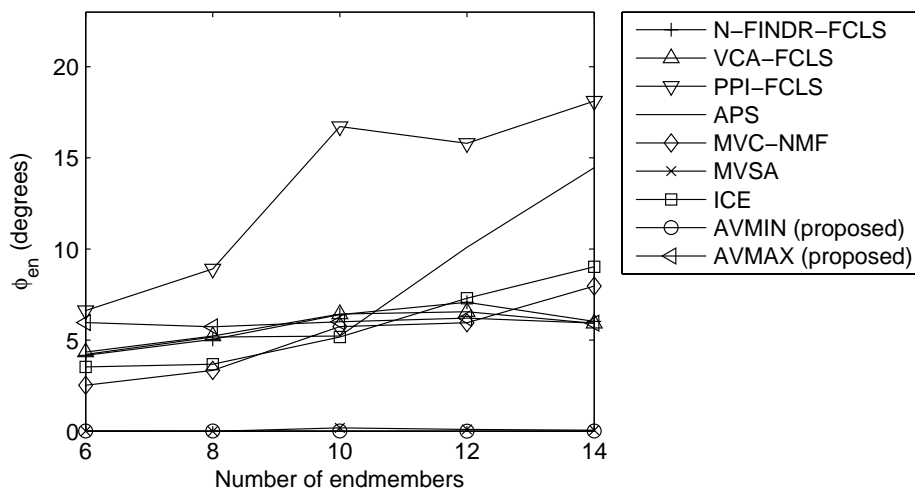
Figure 5.7. Simulation results of the endmember estimates obtained by the various algorithms under test for different number of endmembers (ϕ_{en}).
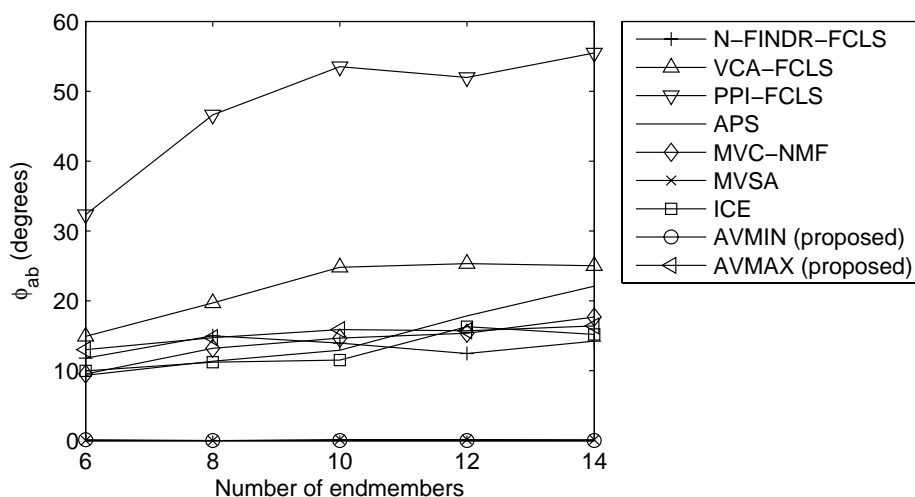
Figure 5.8. Simulation results of the abundance estimates obtained by the various algorithms under test for different number of endmembers (ϕ_{ab}).

5.4.3 Monte Carlo Simulations for Various SNRs

The noise-free synthetic data $\mathbf{x}[n]$ were generated in the same manner as in Section 5.4.1. The noisy data were obtained by adding independent and identically distributed (i.i.d.) zero-mean Gaussian noise to the noise-free data for different values of SNR, where

$$\text{SNR} = \frac{\sum_{n=1}^{L} \|\mathbf{x}[n]\|^2}{\sigma^2 M L}$$

in which σ^2 is the noise variance. To maintain non-negativity of the noisy observed pixels, we manually set the negative values of the noisy pixels to zero. Again 100 Monte Carlo runs were performed to evaluate the performance of the unmixing algorithms under test.

The average ϕ_{en} and ϕ_{ab} for all the unmixing algorithms over SNR = 15, 20, ..., 40, ∞ dB and $\rho = 0.7, 0.85, 1$ are shown in Table 5.4, where each bold-faced number denotes the minimum rms spectral angle associated with a specific pair (ρ, SNR) over all the algorithms. Some observations from Table 5.4 are as follows. Basically, for a fixed SNR most algorithms (except for MVSA and the proposed AVMIN) performed better for higher purity level. For a fixed purity level, most algorithms (without involving pure pixels, i.e., MVC-NMF, MVSA, ICE and AVMIN) performed better for higher SNR. This was also true for APS and PPI-FCLS for $\rho = 0.85$ and $\rho = 1$, and true for N-FINDR-FCLS and VCA-FCLS when $\rho = 1$. Specifically, in terms of ϕ_{en}, the proposed AVMIN performed best for $\rho = 0.7$ and $20 \leq \text{SNR} \leq 40$ dB, and when $\rho = 0.85$ and SNR$= 40$ dB, and in terms of ϕ_{ab}, the AVMIN outperformed all the other algorithms for $\rho = 0.7$ and $20 \leq \text{SNR} \leq 40$ dB. The pure-pixel based methods, PPI-FCLS, N-FINDR-FCLS, VCA-FCLS, and AVMAX generally performed better than the other algorithms for $\rho = 1$ and SNR≤ 40 dB. However, the proposed AVMIN showed slightly worse performance as purity level increases, so does MVSA. The reason for this may be due to their mild susceptibility to noise effects. Nevertheless,

their performances for SNR= ∞ indeed become better as purity level increases. On the other hand, the average computation time (secs) per realization for each unmixing methods under the presence of noise is also displayed in Table 5.3. The complexity comparison results of all the algorithms were similar to those in the noise-free case.

Table 5.4. Performance comparison of average ϕ_{en} and ϕ_{ab} (degrees) over the various unmixing methods for different purity levels (ρ) and SNRs.

| Methods | ρ | ϕ_{en} | | | | | ϕ_{ab} | | | | |
| | | SNR (dB) | | | | | SNR (dB) | | | | |
		20	25	30	35	40	20	25	30	35	40
PPI-FCLS	0.7	6.24	6.09	6.02	6.05	6.01	44.77	45.80	46.27	46.60	45.78
	0.85	4.05	3.56	2.77	2.78	2.71	23.46	20.02	12.02	11.59	10.82
	1	1.46	**0.58**	0.33	**0.17**	**0.09**	7.59	3.46	**2.04**	**1.21**	**0.70**
N-FINDR-FCLS	0.7	5.45	5.31	5.24	5.11	5.16	22.54	21.86	21.63	19.76	19.82
	0.85	2.65	2.67	2.66	2.65	2.61	9.60	8.37	8.03	7.93	7.77
	1	1.15	0.58	0.33	0.18	0.10	6.14	3.59	2.13	1.24	0.72
VCA-FCLS	0.7	5.77	5.56	5.64	5.56	5.50	31.57	29.97	29.71	28.54	28.38
	0.85	2.79	2.70	2.67	2.71	2.61	10.83	9.45	9.00	8.89	8.82
	1	**1.12**	0.61	**0.32**	0.18	0.11	**6.00**	**3.45**	2.05	1.23	0.76
APS	0.7	8.22	7.56	7.79	7.22	15.44	28.45	28.13	27.49	24.98	26.83
	0.85	4.16	4.27	4.04	3.93	4.01	18.56	15.67	13.98	13.67	13.11
	1	2.75	1.55	1.25	1.10	1.01	12.59	7.18	4.99	4.75	4.47
MVC-NMF	0.7	6.80	5.32	4.50	6.05	4.49	26.69	20.55	16.54	21.89	15.60
	0.85	**2.47**	**1.37**	**1.31**	**1.34**	1.32	**5.81**	**4.61**	**4.26**	4.27	4.18
	1	1.48	0.89	0.71	0.66	0.64	7.87	4.52	2.87	2.07	1.75
MVSA	0.7	5.95	4.03	2.67	2.12	1.40	20.80	14.56	7.88	4.81	3.14
	0.85	5.99	3.75	2.61	2.07	1.27	19.65	12.12	7.17	**4.16**	**2.34**
	1	6.12	3.96	2.71	2.14	1.33	18.93	11.55	6.68	3.85	2.15
ICE	0.7	6.43	5.13	4.21	4.22	4.22	24.13	17.85	12.03	12.23	12.62
	0.85	2.86	2.76	2.79	2.78	2.79	9.45	8.66	8.58	8.40	8.48
	1	1.69	1.50	1.47	1.42	1.36	7.21	6.63	6.28	5.64	4.88
AVMAX	0.7	5.50	5.36	5.39	5.13	5.10	24.60	21.94	20.95	18.77	16.48
	0.85	2.77	2.64	2.65	2.69	2.65	9.15	7.96	7.10	6.70	6.48
	1	1.14	0.61	0.33	0.18	0.10	6.39	3.66	2.13	1.22	**0.70**
AVMIN	0.7	**5.17**	**3.26**	**2.43**	**1.73**	**1.01**	**16.66**	**10.58**	**6.51**	**3.81**	**2.17**
	0.85	5.28	3.59	2.65	1.85	**1.11**	16.88	10.98	7.20	4.26	2.38
	1	6.67	4.37	3.35	2.50	1.55	19.81	13.09	9.58	6.81	4.50

5.4.4 Monte Carlo Simulations for Non-uniform Noise

Here we consider a more realistic scenario where noise variances over spectral bands are non-uniform. To do this, we generated independent zero-mean Gaussian noise

for the M spectral bands, whose variances denoted as $\sigma_1^2, \ldots, \sigma_M^2$ follow a Gaussian shape centered at the $(M/2)$th band [77], i.e.,

$$\sigma_i^2 = \sigma^2 \frac{e^{-\frac{(i-M/2)^2}{2\eta^2}}}{\sum_{j=1}^{M} e^{-\frac{(j-M/2)^2}{2\eta^2}}}, \ \forall \ i = 1, \ldots, M, \tag{5.38}$$

where η controls the variance of the Gaussian shape among $\sigma_1^2, \ldots, \sigma_M^2$. It corresponds to white noise for $\eta = \infty$, and one-band noise for $\eta = 0$.

The average ϕ_{en} and ϕ_{ab} of all the unmixing algorithms for $\rho = 0.75$, SNR $= 20, 25$, ..., 40 dB, $\eta = \infty, 18, 9$ are shown in Table 5.5, where again each bold-faced number represents the minimum rms spectral angle associated with a specific pair (η, SNR) over all the algorithms. One can see that while the performance of our AVMIN almost outperformed all the other algorithms under the white noise scenario ($\eta = \infty$), it may not be true for some non-uniform noise scenarios ($\eta = 18, 9$). Nevertheless, AVMIN showed competitive performance in general. Our speculation is that the affine set fitting in AVMIN may not provide very accurate affine subspace estimates (i.e., $\mathbf{d}_e$ and $\mathbf{C}_e$ in (5.4) and (5.5), respectively) in the presence of non-uniform noise. One possible approach to mitigate this problem is by employing the recently proposed subspace identification method [77] which considers the non-uniform noise and may provide more accurate subspace estimates than those used in this paper. This may be an interesting future direction to pursue.

The above Monte Carlo simulation results (as shown in Figures 5.5, 5.6, 5.7, and 5.8, and Tables 5.4 and 5.5) demonstrate that the performance of AVMAX and N-FINDR-FCLS were very comparable, and that the AVMIN performed better than N-FINDR-FCLS, VCA-FCLS, PPI-FCLS, APS, MVC-NMF, ICE, and AVMAX for both the noiseless and noisy cases (especially for data with lower purity levels). Regarding the comparison of MVSA and our AVMIN, we conclude that their performances were very comparable, and in most white noise cases with lower purity levels and various

SNRs the AVMIN slightly outperformed the MVSA. However, we also see from Table 5.3 that AVMIN spent more computation time than MVSA. There appears to be a tradeoff between performance and complexity for the two algorithms.

Table 5.5. Performance comparison of average ϕ_{en} and ϕ_{ab} (degrees) over the various unmixing methods for white noise ($\eta = \infty$) and non-uniform noise ($\eta = 18, 9$), and purity level $\rho = 0.75$.

Methods	η	ϕ_{en} SNR (dB)					ϕ_{ab} SNR (dB)				
		20	25	30	35	40	20	25	30	35	40
PPI-FCLS	∞	6.48	6.74	6.09	6.07	6.11	44.60	49.68	45.18	47.65	40.66
	18	7.08	6.43	6.39	6.29	6.01	47.04	48.29	48.68	41.26	42.13
	9	8.75	6.61	6.32	6.21	6.29	55.63	48.04	42.97	44.67	44.90
N-FINDR-FCLS	∞	4.51	4.57	4.48	4.38	4.51	15.75	14.84	14.31	14.11	14.12
	18	4.77	4.48	4.30	4.50	4.49	17.69	14.71	14.08	14.33	13.98
	9	6.06	4.58	4.22	4.54	4.36	34.32	15.83	14.90	15.53	14.97
VCA-FCLS	∞	5.76	5.40	5.39	5.00	4.86	27.59	28.63	26.08	25.94	23.94
	18	5.86	5.19	5.13	5.10	4.93	33.81	28.02	27.31	25.24	23.60
	9	**6.01**	5.74	4.56	4.91	4.94	38.78	33.31	24.18	22.87	25.5
APS	∞	4.36	4.98	4.61	4.37	4.12	17.53	17.18	15.43	15.40	14.89
	18	**5.03**	4.79	4.28	4.29	4.32	22.61	18.57	16.50	15.74	14.42
	9	7.54	6.31	3.93	4.38	3.23	32.41	22.54	17.31	14.61	13.75
MVC-NMF	∞	5.42	4.21	2.95	2.71	1.70	**16.22**	16.68	15.51	9.42	7.14
	18	5.14	3.37	2.66	2.60	2.21	26.20	12.29	8.13	8.17	8.32
	9	6.60	7.00	3.60	2.08	2.60	29.60	28.79	14.91	8.25	8.47
MVSA	∞	5.28	3.75	2.77	2.11	1.17	19.48	12.75	7.49	4.41	2.52
	18	9.21	4.09	**2.26**	**1.31**	**0.71**	27.95	12.93	**5.85**	**3.18**	**1.73**
	9	10.13	9.15	2.43	**1.35**	**0.62**	37.78	31.85	**4.12**	**3.25**	**1.67**
ICE	∞	5.83	5.74	5.65	5.69	5.30	28.36	25.39	25.92	25.07	26.19
	18	5.40	5.37	5.37	4.64	5.30	25.47	25.49	24.21	30.75	26.19
	9	5.40	5.29	5.40	5.16	5.46	**26.11**	27.59	26.47	25.16	27.41
AVMAX	∞	**4.40**	4.37	4.26	4.47	4.29	16.69	14.67	13.74	13.64	12.93
	18	7.11	5.09	4.31	4.26	4.30	25.93	14.39	13.57	13.27	12.88
	9	6.20	4.35	4.18	4.31	4.21	35.17	15.21	13.33	12.66	13.29
AVMIN	∞	5.18	**3.30**	**2.47**	**1.74**	**1.05**	16.83	**10.74**	**6.88**	**3.96**	**2.25**
	18	7.11	**3.48**	2.57	1.62	1.16	**22.14**	**10.57**	6.41	4.22	2.36
	9	8.56	**3.67**	**2.09**	1.40	0.73	32.20	**12.23**	5.28	3.65	2.05

5.5 Experimental Results

Since the performance of the proposed AVMAX is quite comparable to that of N-FINDR-FCLS (suggested by the numerical results in Section 5.4), we here applied the

proposed AVMIN to process real hyperspectral image data [90], collected by airborne visible/infrared imaging spectrometer (AVIRIS) flight over the Cuprite mining site, Nevada, in 1997. This data set has been widely used for remote sensing experiments [70, 79, 86], and it consists of 224 spectral channels with 10 nm spectral resolution covering wavelengths ranging from 0.4 to 2.5 μm. The spectral bands 1-2, 104-113, 148-167, and 221-224 were removed due to low SNR and water-vapor absorption. Hence, a total of 188 bands were used in this experiment. The subimage of the 150th band, including 200 vertical lines with 200 pixels per line is shown in Figure 5.9. Two existing benchmark methods, VCA-FCLS [79,81] and MVC-NMF [86], were also tested for performance comparison.

One of VD methods [76], the noise-whitened HFC (NWHFC)-based eigenthresholding method with false-alarm probability $P_F = 10^{-5}$, was applied to the data set to estimate the number of endmembers, and the estimated number of endmembers is $N = 14$. By visually comparing the abundance maps estimated by the AVMIN with the ground truth reported in [91,92], the abundance maps obtained by AVMIN were identified as mineral maps of Muscovite, Goethite, Halloysite, Nontronite, Montmorillonite, Alunite, Buddingtonite, Pyrope, Kaolinite #1, Kaolinite #2, Chalcedony, Desert Varnish, Kaolinite #3, and Andradite as shown in Figures 5.10(a)-(n), respectively. Likewise, the abundance maps obtained by MVC-NMF were identified as mineral maps of Muscovite, Nontronite, Montmorillonite, Alunite, Buddingtonite, Pyrope, Kaolinite #1, Chalcedony, Desert Varnish, Andradite, Kaolinite #4, and Dumortierite as shown in Figure 5.11(a)-(n), respectively, and those obtained by VCA-FCLS were identified as mineral maps of Muscovite, Nontronite, Montmorillonite, Alunite, Buddingtonite, Pyrope, Kaolinite #1, Chalcedony, Desert Varnish, Andradite, Kaolinite #4, and Dumortierite as shown in Figure 5.12(a)-(n), respectively. Furthermore, the endmember estimates obtained by the three unmixing algorithms associated with the identified minerals are also shown in Figure 5.13. Figure 5.13(a)

shows the library spectra of all the identified minerals. The endmember estimates obtained by AVMIN are shown in Figure 5.13(b), and those obtained by MVC-NMF and VCA are shown in Figures 5.13(c) and 5.13(d), respectively. One can see from Figure 5.13 that all the fourteen distinct minerals were retrieved by AVMIN, while twelve distinct minerals were retrieved by both MVC-NMF and VCA. Although MVC-NMF adds Craig's criterion (as a regularization term) in its objective function, the reason for fewer minerals retrieved by MVC-NMF may be due to its initialization by VCA. By the same token, one can also observe that MVC-NMF and VCA retrieved the same minerals in this experiment.

To further evaluate the accuracy of the mineral-identified endmember estimates obtained by the three unmixing algorithms, we used the mean-removed spectral angle between each mineral-identified endmember estimate $\widehat{\mathbf{a}}$ and its corresponding signature in the library spectrum of the identified mineral $\mathbf{a}$ [93] as a performance index, i.e.,

$$\phi = \arccos \left(\frac{(\widehat{\mathbf{a}} - \mathbf{m}(\widehat{\mathbf{a}}))^T (\mathbf{a} - \mathbf{m}(\mathbf{a}))}{\|\widehat{\mathbf{a}} - \mathbf{m}(\widehat{\mathbf{a}})\| \, \|\mathbf{a} - \mathbf{m}(\mathbf{a})\|} \right), \tag{5.39}$$

where $\mathbf{m}(\mathbf{a}) = (\mathbf{1}_M^T \mathbf{a}/M)\mathbf{1}_M$ for any vector $\mathbf{a} \in \mathbb{R}^M$.

The spectral angles ϕ associated with the endmember estimates obtained by the three unmixing algorithms are shown in Table 5.6 where those numbers in the parentheses represents the mean-removed spectral angles of the endmember estimates classified as the same mineral. One can see from Table 5.6 that the average mean-removed spectral angle associated with AVMIN was smaller than that associated with MVC-NMF, but larger than that associated with VCA. The possible cause may be due to serious effect of non-uniform noise which might have resulted in some performance degradation of the proposed AVMIN. We would consider the non-uniform noise issues for the AVMIN as our future research. In spite of that, AVMIN also showed the capability of retrieving some less prevalent minerals, i.e., Goethite and Halloysite, which were not retrieved by MVC-NMF and VCA. Moreover, we also compared the above

experimental results to the results reported in [20, 79, 86, 91, 92], and found that they all exhibit a high degree of agreement between them.
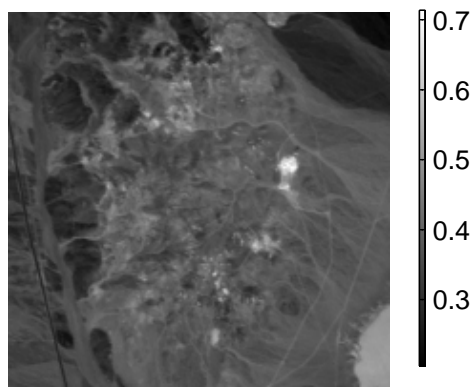
Figure 5.9. The subimage of the AVIRIS hyperspectral image data for the 150th band.

5.6   Summary

In this chapter, we have analytically proven the intuitive ideas of Winter [43] and Craig [45] from a convex analysis and optimization perspective. After performing dimension reduction of observed pixels through an affine set fitting, we have shown that all such dimension-reduced pixels are enclosed by a simplex. The main idea of Winter's (or Craig's) unmixing criterion is to find a maximum-volume (or minimum-volume) simplex within (or enclosing) all the dimension-reduced pixels. We have formulated two optimization problems for hyperspectral unmixing by utilizing these two criteria, and proven that these two problems achieve endmember identifiability and lead to identical optimal solutions under the pure-pixel assumption [(A3)]. We have also demonstrated the application of alternating linear programming to approximate the formulated maximum-volume (or minimum-volume) simplex fitting problems.

We have carried out extensive computer simulations to demonstrate the compa-
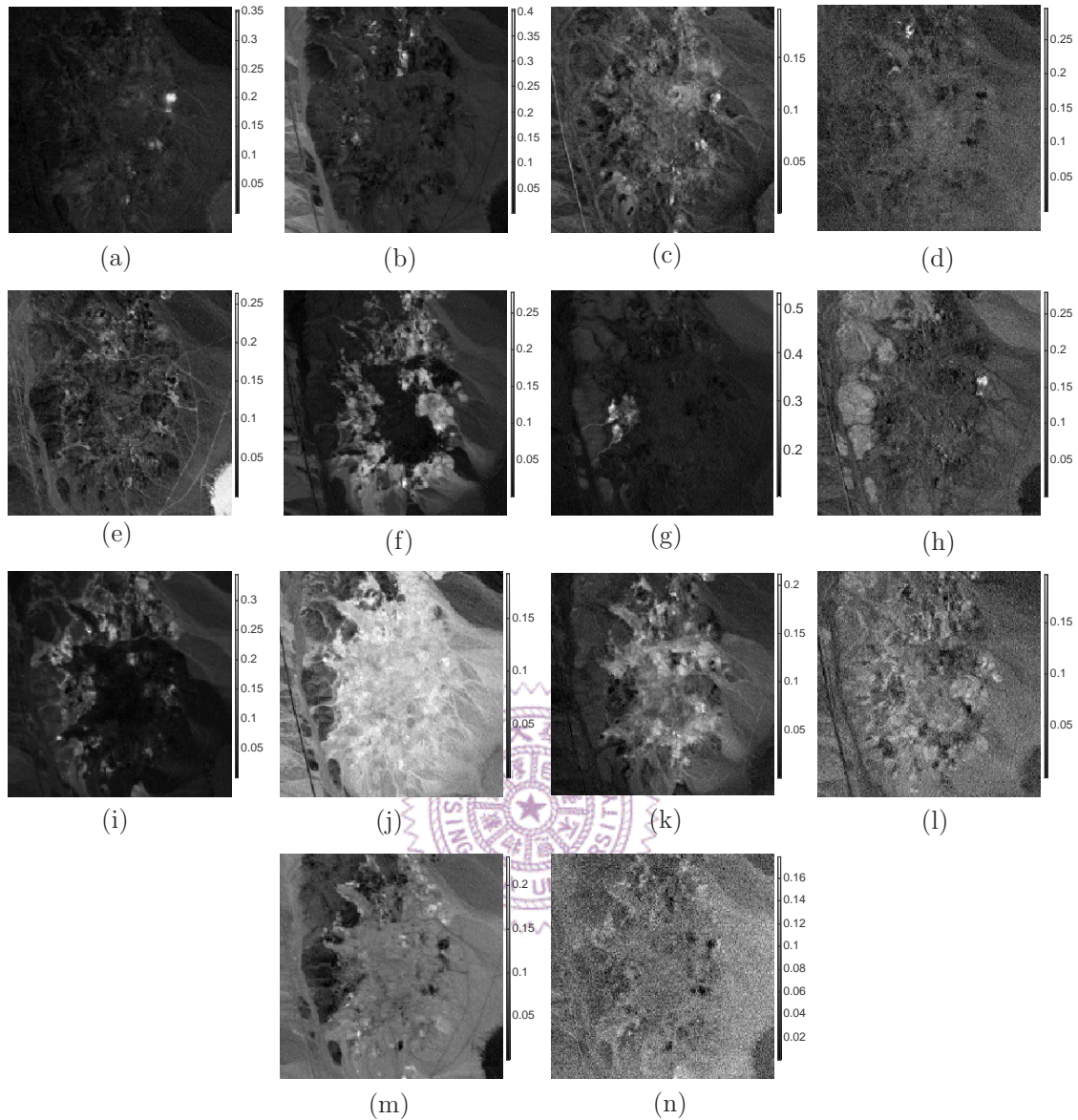
Figure 5.10. Fourteen respective estimated abundances obtained by AVMIN: (a) Muscovite, (b) Goethite, (c) Halloysite, (d) Nontronite, (e) Montmorillonite, (f) Alunite, (g) Buddingtonite, (h) Pyrope, (i) Kaolinite #1, (j) Kaolinite #2, (k) Chalcedony, (l) Desert Varnish, (m) Kaolinite #3, and (n) Andradite.

rable performance of the proposed AVMAX with that of N-FINDR, and to show that the proposed AVMIN outperforms some existing benchmark hyperspectral unmixing algorithms. In addition, the simulation results also provide a validation for our analytical results which says that AVMAX and AVMIN are equivalent when pure

93
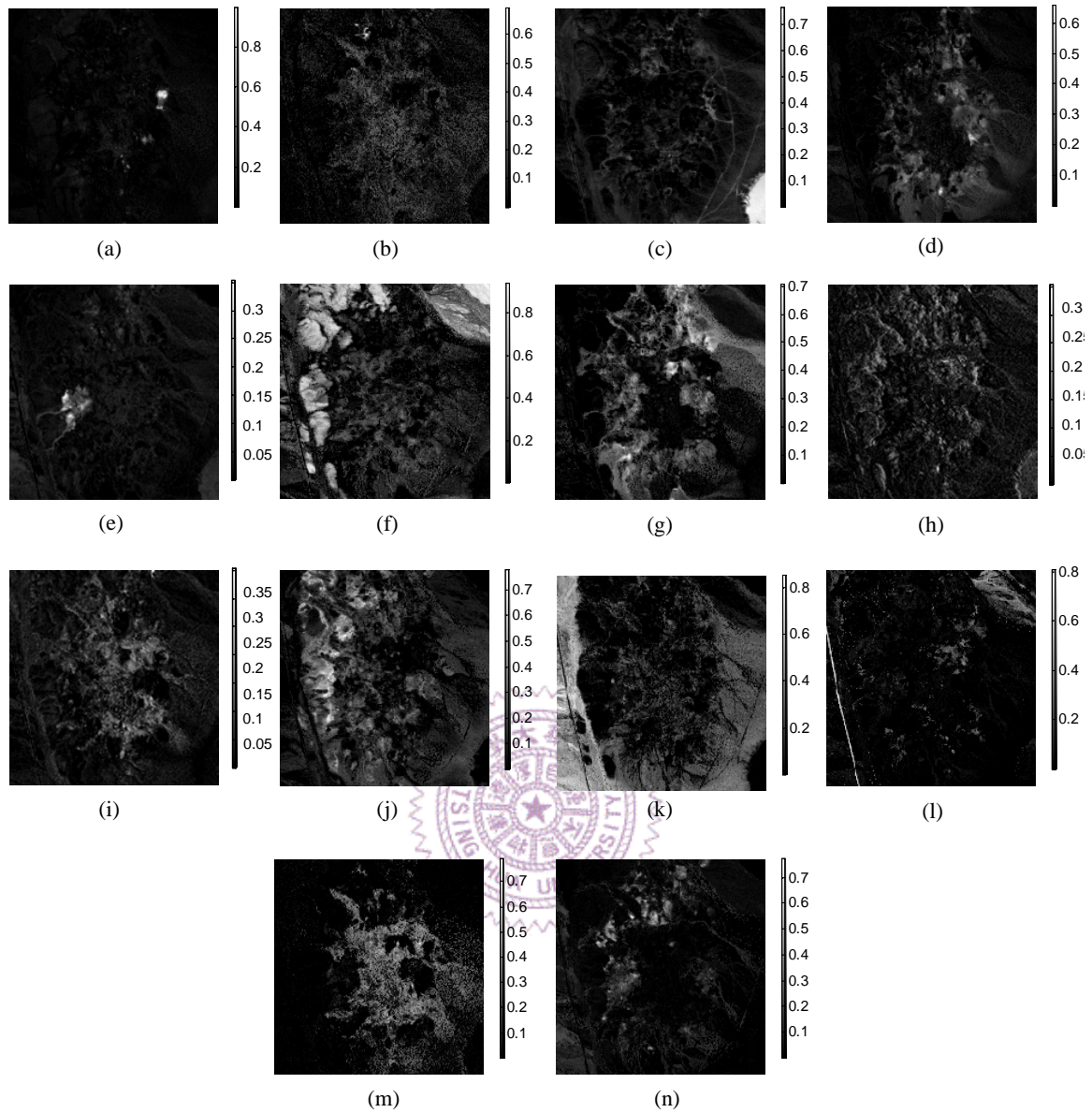
Figure 5.11. Fourteen respective estimated abundances obtained by MVC-NMF algorithm: (a) Muscovite, (b) Nontronite, (c) Montmorillonite, (d) Alunite, (e) Buddingtonite, (f) Pyrope, (g) Kaolinite #1, (h) Kaolinite #1, (i) Chalcedony, (j) Desert Varnish, (k) Andradite, (l) Kaolinite #4, (m) Kaolinite #4, and (n) Dumortierite.

pixels exist in the observed data. Finally, the experimental results with real hyperspectral image data show that the proposed AVMIN can estimate endmembers and abundances which highly agrees with the reported ground truth.
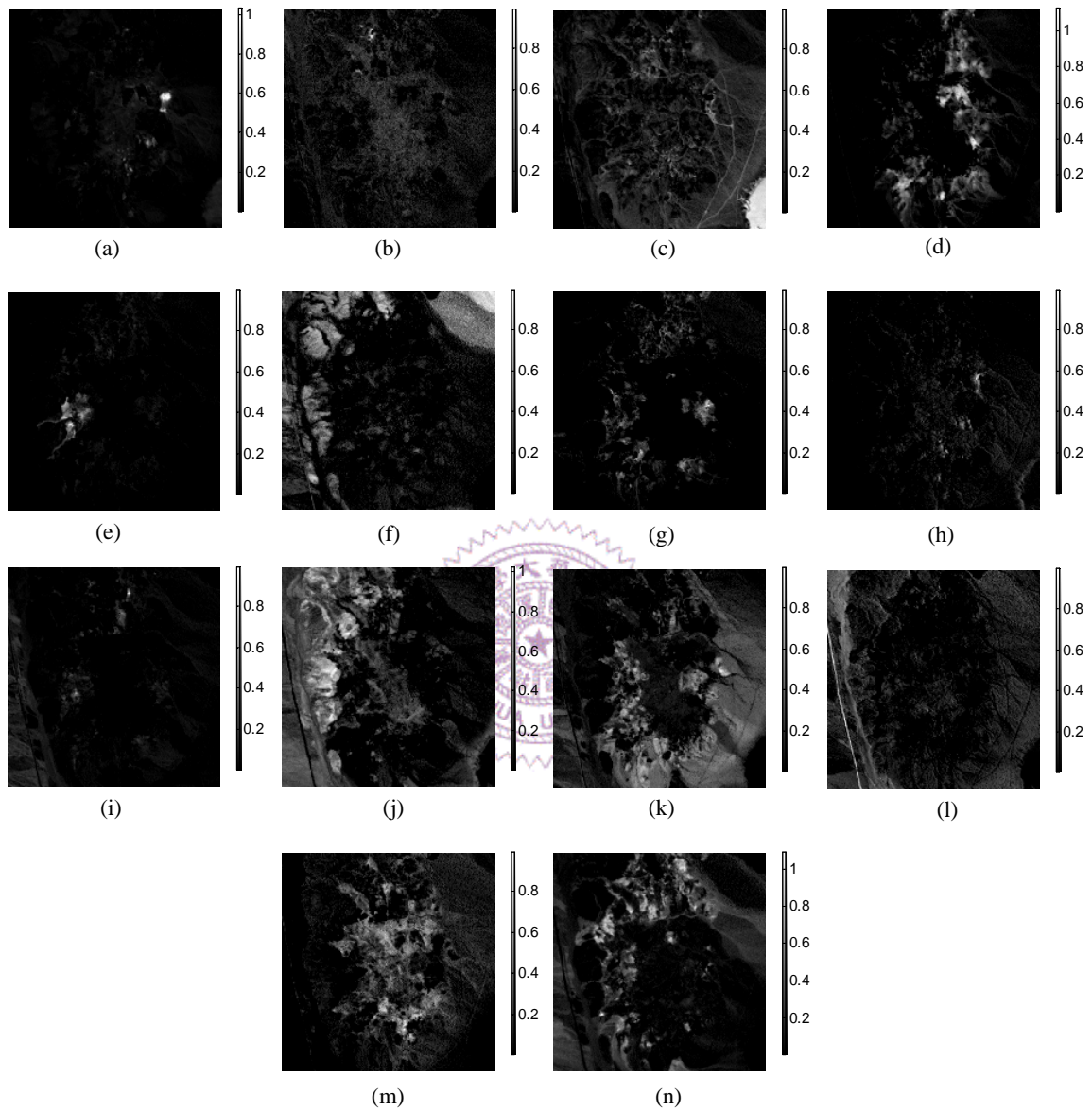
Figure 5.12. Fourteen respective estimated abundances obtained by VCA-FCLS algorithm: (a) Muscovite, (b) Nontronite, (c) Montmorillonite, (d) Alunite, (e) Buddingtonite, (f) Pyrope, (g) Kaolinite #1, (h) Kaolinite #1, (i) Chalcedony, (j) Desert Varnish, (k) Andradite, (l) Kaolinite #4, (m) Kaolinite #4, and (n) Dumortierite.
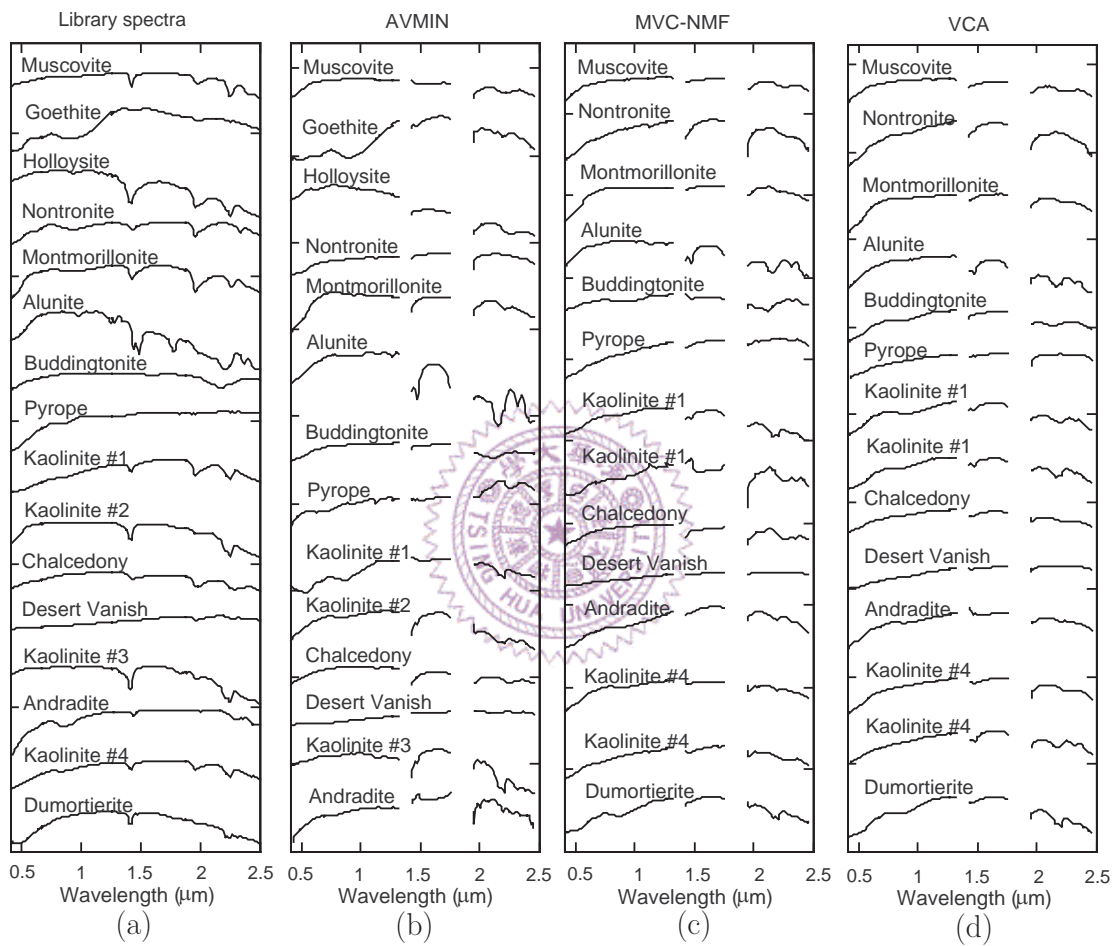
Figure 5.13. (a) The endmember signatures provided by the USGS library, and the endmember estimates obtained by (b) AVMIN (c) MVC-NMF and (d) VCA.

Table 5.6. Mean-removed spectral angles ϕ (degrees) between library spectra and end-members estimated by AVMIN, MVC-NMF, and VCA.

	AVMIN	MVC-NMF	VCA
Muscovite	35.64	33.93	32.70
Goethite	15.08	-	-
Halloysite	13.10	-	-
Nontronite	29.74	20.21	16.14
Montmorillonite	25.54	19.81	15.98
Alunite	19.55	18.97	23.48
Buddingtonite	20.68	36.91	27.25
Pyrope	32.37	14.49	19.97
Kaolinite #1	22.95	27.74 (31.84)	22.55 (22.04)
Kaolinite #2	21.32	-	-
Chalcedony	26.01	23.02	31.09
Desert Varnish	14.74	15.69	16.13
Kaolinite #3	17.52	-	-
Andradite	26.80	19.21	18.16
Kaolinite #4	-	19.77 (12.00)	18.17 (21.05)
Dumortierite	-	33.34	20.44
Average ϕ	22.92	23.35	21.80

Chapter 6

Conclusions and Future Works

In this dissertation, we have provided a new avenue to solve nBSS by using convex geometry without any source statistical independence/uncorrelatedness assumption.

We have developed CAMNS framework (presented in Chapter 4), which utilizes the local dominance assumption [(A3)] to connect nBSS and convex geometry. We have established a deterministic, convex analysis based nBSS criterion that determines the true sources by finding the extreme points of the observation-constructed polyhedral set. We adopted LP to develop two methods for fulfilling the proposed nBSS criterion (a vertex enumeration problem). The first one is the CAMNS-LP which is supported by rigorous mathematical analysis. It uses LP to systematically locate all the extreme points. The second one is CAMNS-AVM which uses alternating volume maximization heuristic for locating the extreme points. We have shown by simulations that CAMNS-AVM can provide better robustness than CAMNS-LP when model assumptions are not perfectly satisfied. The extensive simulation results with some scenarios including X-ray, blood cells, human portraits, and ghosting were presented to demonstrate the superior performance of CAMNS-based methods over several benchmark nBSS methods. In real data experiments with dynamic fluorescent images and multispectral microscopy where the true number of sources is unknown, we

have modified the CAMNS framework by utilizing some prior knowledge to improve its effectiveness. The experimental results demonstrated the efficacy and applicability of CAMNS-PI in solving nBSS problems with real image data.

We have also provided a convex analysis and optimization perspective to nBSS problems in hyperspectral remote sensing (presented in Chapter 5), which analytically proves the intuitive ideas of Winter's and Craig's unmixing criteria, respectively. Using the notion of convex analysis, we have shown that the dimension reduction of the observed pixels would lead to dimension-reduced pixels that are confined by a simplex. The main idea of Winter's (or Craig's) unmixing criterion is to find a maximum-volume (or minimum-volume) simplex within (or enclosing) all the dimension-reduced pixels. Based on these two unmixing criteria, we have formulated the maximum-volume simplex fitting and minimum-volume simplex fitting problems as optimization problems respectively, and shown that these two problems identically achieve perfect unmixing when there exist pure pixels [(A3)]. We have also demonstrated how we use alternating linear programming to solve the formulated simplex volume maximization and simplex volume minimization problems, referred therein as AVMAX and AVMIN, respectively. Monte Carlo simulation results with four synthetic data sets have validated our analytical results that Winter's and Craig's unmixing criteria are equivalent under the pure pixel assumption [(A3)], and demonstrated the efficacy of the proposed unmixing methods. Using the real hyperspectral image data collected over the Cuprite mining site, Nevada, in 1997, we have shown that the proposed AVMIN can estimate endmembers and abundances both in a high agreement with the reported ground truth.

We have also released MATLAB source codes for practical implementations of CAMNS-LP and AVMIN at http://www.ee.cuhk.edu.hk/~wkma/CAMNS/CAMNS.htm and http://www.ee.nthu.edu.tw/cychi/software_download.htm, respectively. We encourage readers to verify our results and give us some feedback. One should note

that the AVMIN in this dissertation is exactly the same as the minimum-volume enclosing simplex (MVES) algorithm available on the website.

This dissertation leave some worthwhile future research directions as follows. The first one is convergence analysis for the proposed nBSS methods involving alternating LP (such as CAMNS-AVM, AVMAX, and AVMIN), which could possibly be done under the local dominance assumption [(A3)]. The second one is the complexity reduction of the CAMNS-AVM, AVMAX, and AVMIN such that they can be more suitable for large-scale real data experiments. This may be accomplished by making specialized LP algorithms and by introducing a warm start for each LP in running the algorithm. This can also be achieved by identifying and removing the inactive constraints associated with the LPs. The third one is the refinement of the proposed nBSS methods for accommodating different types of noise scenarios, such as white noise and non-uniform noise. In this dissertation, the number of sources N is assumed to be known in advance, and hence the fourth research direction will be the estimation of the number of sources for a given real data. The last one would be tests of the proposed nBSS algorithms for more potential applications; e.g., analytical chemistry, deconvolution of genomic signals, and superresolution image reconstruction, where the sources are non-negative in nature.

Appendix A

Proofs of Theorems and Lemmas in Chapter 4

A.1 Proof of Lemma 1

Any $\boldsymbol{x} \in \text{aff}\{\boldsymbol{x}_1, ..., \boldsymbol{x}_M\}$ can be represented by

$$\boldsymbol{x} = \sum_{i=1}^{M} \theta_i \boldsymbol{x}_i, \tag{A.1}$$

where $\boldsymbol{\theta} \in \mathbb{R}^M$, $\boldsymbol{\theta}^T \boldsymbol{1}_M = 1$. Substituting (2.2) into (A.1), we get

$$\boldsymbol{x} = \sum_{j=1}^{N} \beta_j \boldsymbol{s}_j, \tag{A.2}$$

where $\beta_j = \sum_{i=1}^{M} \theta_i a_{ij}$ for $j = 1, ..., N$, or equivalently

$$\boldsymbol{\beta} = \mathbf{A}^T \boldsymbol{\theta}. \tag{A.3}$$

Since $\mathbf{A}$ has unit row sum [(A4)], we have

$$\boldsymbol{\beta}^T \mathbf{1}_N = \boldsymbol{\theta}^T (\mathbf{A} \mathbf{1}_N) = \boldsymbol{\theta}^T \mathbf{1}_N = 1. \tag{A.4}$$

This implies that $\boldsymbol{\beta}^T \mathbf{1}_N = 1$, and as a result it follows from (A.2) that $\boldsymbol{x} \in \mathrm{aff}\{\boldsymbol{s}_1, ..., \boldsymbol{s}_N\}$.

On the other hand, any $\boldsymbol{x} \in \mathrm{aff}\{\boldsymbol{s}_1, ..., \boldsymbol{s}_N\}$ can be represented by (A.2) for $\boldsymbol{\beta}^T \mathbf{1}_N = 1$. Since $\mathbf{A}$ has full column rank [(A2)], there always exist a $\boldsymbol{\theta}$ such that (A.3) holds. Substituting (A.3) into (A.2) yields (A.1). Since (A.4) implies that $\boldsymbol{\theta}^T \mathbf{1}_M = 1$, we conclude that $\boldsymbol{x} \in \mathrm{aff}\{\boldsymbol{x}_1, ..., \boldsymbol{x}_M\}$.

A.2 Proof of Lemma 2

We prove the linear independence of $\boldsymbol{s}_1, ..., \boldsymbol{s}_N$ by showing that $\sum_{j=1}^{N} \theta_j \boldsymbol{s}_j = \boldsymbol{0}$ only has the trivial solution $\theta_1 = \theta_2 = ... = \theta_L = 0$.

Suppose that $\sum_{j=1}^{N} \theta_j \boldsymbol{s}_j = \boldsymbol{0}$ is true. Under (A3), for each source i we have the ℓ_ith entry (the local dominant point) of $\sum_{j=1}^{N} \theta_j \boldsymbol{s}_j$ given by

$$0 = \sum_{j=1}^{N} \theta_j s_j[\ell_i] = \theta_i s_i[\ell_i]. \tag{A.5}$$

Since $s_i[\ell_i] > 0$, we must have $\theta_i = 0$ and this has to be satisfied for all i. As a result, Lemma 2 is obtained. ∎

A.3 Proof of Proposition 1

As a basic result in least squares, each projection error in (4.4)

$$e_{\mathcal{A}(\tilde{\mathbf{C}}, \tilde{\mathbf{d}})}(\boldsymbol{x}_i) = \min_{\boldsymbol{\alpha} \in \mathbb{R}^{N-1}} \|\tilde{\mathbf{C}} \boldsymbol{\alpha} + \tilde{\mathbf{d}} - \boldsymbol{x}_i\|_2^2 \tag{A.6}$$

has a closed form

$$e_{\mathcal{A}(\tilde{\mathbf{C}},\tilde{\mathbf{d}})}(\boldsymbol{x}_i) = (\boldsymbol{x}_i - \tilde{\mathbf{d}})^T \mathbf{P}_{\tilde{\mathbf{C}}}^{\perp} (\boldsymbol{x}_i - \tilde{\mathbf{d}}) \tag{A.7}$$

where $\mathbf{P}_{\tilde{\mathbf{C}}}^{\perp}$ is the orthogonal complement projection of $\tilde{\mathbf{C}}$. Using (A.7), the affine set fitting problem [in (4.4)] can be rewritten as

$$\min_{\tilde{\mathbf{C}}^T \tilde{\mathbf{C}} = \mathbf{I}_{N-1}} \left\{ \min_{\tilde{\mathbf{d}}} \sum_{i=1}^{M} (\boldsymbol{x}_i - \tilde{\mathbf{d}})^T \mathbf{P}_{\tilde{\mathbf{C}}}^{\perp} (\boldsymbol{x}_i - \tilde{\mathbf{d}}) \right\}. \tag{A.8}$$

The inner minimization problem in (A.8) is an unconstrained convex quadratic program, and it can be easily verified that $\mathbf{d} = \frac{1}{M} \sum_{i=1}^{M} \boldsymbol{x}_i$ is an optimal solution to the inner minimization problem. By substituting this optimal $\mathbf{d}$ into (A.8) and by letting $\mathbf{U} = [\boldsymbol{x}_1 - \mathbf{d}, ..., \boldsymbol{x}_M - \mathbf{d}]$, problem (A.8) can be reduced to

$$\min_{\tilde{\mathbf{C}}^T \tilde{\mathbf{C}} = \mathbf{I}_{N-1}} \operatorname{Trace}\{\mathbf{U}^T \mathbf{P}_{\tilde{\mathbf{C}}}^{\perp} \mathbf{U}\}. \tag{A.9}$$

When $\tilde{\mathbf{C}}^T \tilde{\mathbf{C}} = \mathbf{I}_{N-1}$, the projection matrix $\mathbf{P}_{\tilde{\mathbf{C}}}^{\perp}$ can be simplified to $\mathbf{I}_L - \tilde{\mathbf{C}}\tilde{\mathbf{C}}^T$. Subsequently (A.9) can be further reduced to

$$\max_{\tilde{\mathbf{C}}^T \tilde{\mathbf{C}} = \mathbf{I}_{N-1}} \operatorname{Trace}\{\mathbf{U}^T \tilde{\mathbf{C}}\tilde{\mathbf{C}}^T \mathbf{U}\}. \tag{A.10}$$

An optimal solution of (A.10) is known to be the $N-1$ principal eigenvector matrix of $\mathbf{U}\mathbf{U}^T$ [56] as given by (4.8). ∎

A.4 Proof of Lemma 3

Assume that $\boldsymbol{z} \in \operatorname{aff}\{\boldsymbol{s}_1, ..., \boldsymbol{s}_N\} \cap \mathbb{R}_+^L$:

$$\boldsymbol{z} = \sum_{i=1}^{N} \theta_i \boldsymbol{s}_i \succeq \mathbf{0}, \quad \mathbf{1}_N^T \boldsymbol{\theta} = 1.$$

From (A3), it follows that $z[\ell_i] = \theta_i s_i[\ell_i] \geq 0$, $\forall i$. Since $s_i[\ell_i] > 0$, we must have $\theta_i \geq 0$, $\forall i$. Therefore, $\boldsymbol{z}$ lies in $\text{conv}\{\boldsymbol{s}_1, ..., \boldsymbol{s}_N\}$. On the other hand, assume that $\boldsymbol{z} \in \text{conv}\{\boldsymbol{s}_1, ..., \boldsymbol{s}_N\}$, i.e.,

$$\boldsymbol{z} = \sum_{i=1}^{N} \theta_i \boldsymbol{s}_i, \quad \boldsymbol{1}_N^T \boldsymbol{\theta} = 1, \quad \boldsymbol{\theta} \succeq \boldsymbol{0}$$

implying that $\boldsymbol{z} \in \text{aff}\{\boldsymbol{s}_1, ..., \boldsymbol{s}_N\}$. From (A1), we have $\boldsymbol{s}_i \succeq \boldsymbol{0}$ $\forall i$ and subsequently $\boldsymbol{z} \succeq \boldsymbol{0}$. This completes the proof for (4.10).

A.5   Proof of Lemma 5

Equation (4.12) can also be expressed as

$$\mathcal{F} = \{ \ \boldsymbol{\alpha} \in \mathbb{R}^{N-1} \mid \mathbf{C}\boldsymbol{\alpha} + \mathbf{d} \in \text{conv}\{\boldsymbol{s}_1, ..., \boldsymbol{s}_N\} \ \}.$$

Thus, every $\boldsymbol{\alpha} \in \mathcal{F}$ satisfies

$$\mathbf{C}\boldsymbol{\alpha} + \mathbf{d} = \sum_{i=1}^{N} \theta_i \boldsymbol{s}_i \tag{A.11}$$

for some $\boldsymbol{\theta} \succeq \boldsymbol{0}$, $\boldsymbol{\theta}^T \boldsymbol{1}_N = 1$. Since $\mathbf{C}$ has full column rank, (A.11) can be re-expressed as

$$\boldsymbol{\alpha} = \sum_{i=1}^{N} \theta_i \boldsymbol{\alpha}_i, \tag{A.12}$$

where $\boldsymbol{\alpha}_i = \mathbf{C}^\dagger(\boldsymbol{s}_i - \mathbf{d})$ (or $\mathbf{C}\boldsymbol{\alpha}_i + \mathbf{d} = \boldsymbol{s}_i$). Equation (A.12) implies that $\mathcal{F} = \text{conv}\{\boldsymbol{\alpha}_1, ..., \boldsymbol{\alpha}_N\}$.

We now show that $\mathcal{F} = \text{conv}\{\boldsymbol{\alpha}_1, ..., \boldsymbol{\alpha}_N\}$ is a simplex by contradiction. Suppose that $\{\boldsymbol{\alpha}_1, ..., \boldsymbol{\alpha}_N\}$ is not affinely independent. This means that for some $\gamma_1, \ldots, \gamma_{N-1}$, $\sum_{i=1}^{N-1} \gamma_i = 1$, $\boldsymbol{\alpha}_N = \sum_{i=1}^{N-1} \gamma_i \boldsymbol{\alpha}_i$ can be satisfied. One then has $\boldsymbol{s}_N = \mathbf{C}\boldsymbol{\alpha}_N + \mathbf{d} = \sum_{i=1}^{N-1} \gamma_i \boldsymbol{s}_i$, which is a contradiction to the property that $\{\boldsymbol{s}_1, ..., \boldsymbol{s}_N\}$ is linearly independent. $\blacksquare$

A.6 Proof of Lemma 6

Any point in $\mathcal{S} = \mathrm{conv}\{\boldsymbol{s}_1, ..., \boldsymbol{s}_N\}$ can be equivalently represented by $\boldsymbol{s} = \sum_{i=1}^{N} \theta_i \boldsymbol{s}_i$, where $\boldsymbol{\theta} \succeq \boldsymbol{0}$ and $\boldsymbol{\theta}^T \boldsymbol{1}_N = 1$. Applying this result to (4.22), problem (4.22) can be reformulated as

$$
\begin{aligned}
\min_{\boldsymbol{\theta} \in \mathbb{R}^N} \quad & \sum_{i=1}^{N} \theta_i \rho_i \\
\text{s.t.} \quad & \boldsymbol{\theta}^T \boldsymbol{1}_N = 1, \ \boldsymbol{\theta} \succeq \boldsymbol{0},
\end{aligned}
\tag{A.13}
$$

where $\rho_i = \mathbf{r}^T \boldsymbol{s}_i$. We assume without loss of generality that $\rho_1 < \rho_2 \leq \cdots \leq \rho_N$. If $\rho_1 < \rho_2 < \cdots < \rho_N$, then it is easy to verify that the optimal solution to (A.13) is uniquely given by $\boldsymbol{\theta}^\star = \mathbf{e}_1$. In its counterpart in (4.22), this translates into $\boldsymbol{s}^\star = \boldsymbol{s}_1$. However, when $\rho_1 = \rho_2 = \cdots = \rho_P$ and $\rho_P < \rho_{P+1} \leq \cdots \leq \rho_N$ for some P, the solution of (A.13) is not unique. In essence, the latter case can be shown to have a solution set

$$
\Theta^\star = \{\boldsymbol{\theta} \mid \boldsymbol{\theta}^T \boldsymbol{1}_N = 1, \ \boldsymbol{\theta} \succeq \boldsymbol{0}, \ \theta_{P+1} = ... = \theta_N = 0\}.
\tag{A.14}
$$

We now prove that the non-unique solution case happens with probability zero. Suppose that $\rho_i = \rho_j$ for some $i \neq j$, which means that

$$
(\boldsymbol{s}_i - \boldsymbol{s}_j)^T \mathbf{r} = 0.
\tag{A.15}
$$

Let $v = (\boldsymbol{s}_i - \boldsymbol{s}_j)^T \mathbf{r}$. Apparently, v follows a distribution $\mathcal{N}(0, \|\boldsymbol{s}_i - \boldsymbol{s}_j\|^2)$. Since $\boldsymbol{s}_i \neq \boldsymbol{s}_j$, the probability $\Pr[\rho_i = \rho_j] = \Pr[v = 0]$ is of measure zero. This in turn implies that $\rho_1 < \rho_2 < \cdots < \rho_N$ holds with probability 1. $\blacksquare$

A.7 Proof of Lemma 7

The approach to proving Lemma 7 is similar to that in Lemma 6. Let

$$\rho_i = \mathbf{r}^T \boldsymbol{s}_i = (\mathbf{B}\boldsymbol{w})^T \boldsymbol{s}_i \tag{A.16}$$

for which we have $\rho_i = 0$ for $i = 1, ..., l$. It can be shown that

$$\rho_{l+1} < \rho_{l+2} < \cdots < \rho_N \tag{A.17}$$

holds with probability 1, as long as $\{\boldsymbol{s}_1, \ldots, \boldsymbol{s}_N\}$ is linearly independent. Problems (4.22) and (4.24) are respectively equivalent to

$$p^\star = \min_{\boldsymbol{\theta} \in \mathbb{R}^N} \sum_{i=l+1}^{N} \theta_i \rho_i$$
$$\text{s.t.} \quad \boldsymbol{\theta} \succeq \mathbf{0}, \ \boldsymbol{\theta}^T \mathbf{1} = 1, \tag{A.18}$$

$$q^\star = \max_{\boldsymbol{\theta} \in \mathbb{R}^N} \sum_{i=l+1}^{N} \theta_i \rho_i$$
$$\text{s.t.} \quad \boldsymbol{\theta} \succeq \mathbf{0}, \ \boldsymbol{\theta}^T \mathbf{1}_N = 1. \tag{A.19}$$

Assuming (A.17), we have three distinct cases to consider: (C1) $\rho_{l+1} < 0$, $\rho_N < 0$, (C2) $\rho_{l+1} < 0$, $\rho_N > 0$, and (C3) $\rho_{l+1} > 0$, $\rho_N > 0$.

For (C2), we can see the following: Problem (A.18) has a unique optimal solution $\boldsymbol{\theta}^\star = \mathbf{e}_{l+1}$ [and $\boldsymbol{s}^\star = \boldsymbol{s}_{l+1}$ in its counterpart in (4.22)], attaining an optimal value $p^\star = \rho_{l+1} < 0$. Problem (A.19) has a unique optimal solution $\boldsymbol{\theta}^\star = \mathbf{e}_N$ [and $\boldsymbol{s}^\star = \boldsymbol{s}_N$ in its counterpart in (4.24)], attaining an optimal value $q^\star = \rho_N > 0$. In other words, both (A.18) and (A.19) lead to finding new extreme points. For (C1), problem (A.19)

is shown to have a solution set

$$\Theta^\star = \{\boldsymbol{\theta} \mid \boldsymbol{\theta}^T \mathbf{1}_N = 1, \; \boldsymbol{\theta} \succeq \mathbf{0}, \; \theta_{l+1} = \cdots = \theta_N = 0\}, \tag{A.20}$$

which contains convex combinations of the old extreme points, and the optimal value is $q^\star = 0$. Nevertheless, it is still true that (A.18) finds a new extreme point with $p^\star < 0$. A similar situation happens with (C3), where (A.18) does not find a new extreme point with $p^\star = 0$, but (A.19) finds a new extreme point with $q^\star > 0$. ■

A.8   Proof of Theorem 3

In problem (4.30), the constraints $\boldsymbol{\beta}_i \in \mathcal{F} = \text{conv}\{\boldsymbol{\alpha}_1, \ldots, \boldsymbol{\alpha}_N\}$ imply that

$$\boldsymbol{\beta}_i = \sum_{j=1}^{N} \theta_{ij} \boldsymbol{\alpha}_j \tag{A.21}$$

where $\sum_{j=1}^{N} \theta_{ij} = 1$ and $\theta_{ij} \geq 0$ for $i = 1, \ldots, N$. Hence we can write

$$\boldsymbol{\Delta}(\boldsymbol{\beta}_1, \ldots, \boldsymbol{\beta}_N) = \boldsymbol{\Delta}(\boldsymbol{\alpha}_1, \ldots, \boldsymbol{\alpha}_N)\boldsymbol{\Theta}^T, \tag{A.22}$$

where $\boldsymbol{\Theta} = [\theta_{ij}] \in \mathbb{R}_+^{N \times N}$ and $\boldsymbol{\Theta}\mathbf{1}_N = \mathbf{1}_N$. For such a structured $\boldsymbol{\Theta}$ it was shown that (Lemma 1 in [94])

$$|\det(\boldsymbol{\Theta})| \leq 1 \tag{A.23}$$

and that $|\det(\boldsymbol{\Theta})| = 1$ if and only if $\boldsymbol{\Theta}$ is a permutation matrix. It follows from

(4.28), (A.22) and (A.23) that

$$V(\boldsymbol{\beta}_1, \ldots, \boldsymbol{\beta}_N) = |\det(\boldsymbol{\Delta}(\boldsymbol{\alpha}_1, \ldots, \boldsymbol{\alpha}_N)\boldsymbol{\Theta}^T)|/(N-1)!$$

$$= |\det(\boldsymbol{\Delta}(\boldsymbol{\alpha}_1, \ldots, \boldsymbol{\alpha}_N))| \cdot |\det(\boldsymbol{\Theta})|/(N-1)!$$

$$\leq V(\boldsymbol{\alpha}_1, \ldots, \boldsymbol{\alpha}_N) \tag{A.24}$$

and that the equality holds if and only if $\boldsymbol{\Theta}$ is a permutation matrix, which implies $\{\boldsymbol{\beta}_1, \ldots, \boldsymbol{\beta}_N\} = \{\boldsymbol{\alpha}_1, \ldots, \boldsymbol{\alpha}_N\}$. Hence we conclude that $V(\boldsymbol{\beta}_1, \ldots, \boldsymbol{\beta}_N)$ is maximized if and only if $\{\boldsymbol{\beta}_1, \ldots, \boldsymbol{\beta}_N\} = \{\boldsymbol{\alpha}_1, \ldots, \boldsymbol{\alpha}_N\}$. ∎

Appendix B

Proofs of Theorems and Lemmas

in Chapter 5

B.1 Proof of Lemma 9

It is easy to see from (A1) and (5.9) that (5.11) is true. Next, let us prove that $\text{conv}\{\boldsymbol{\alpha}_1, \ldots, \boldsymbol{\alpha}_N\}$ is a simplex. Assume that $\{\boldsymbol{\alpha}_1, ..., \boldsymbol{\alpha}_N\}$ is affinely dependent, i.e., there exists an $\boldsymbol{\alpha}_j = \sum_{i \neq j}^{N} \theta_i \boldsymbol{\alpha}_i$ where $\sum_{i \neq j}^{N} \theta_i = 1$. One then has $\mathbf{a}_j = \mathbf{C}_e \boldsymbol{\alpha}_j + \mathbf{d}_e = \sum_{i \neq j}^{N} \theta_i \mathbf{a}_i$ where $\sum_{i \neq j}^{N} \theta_i = 1$ by (5.10), implying $\mathbf{a}_1, ..., \mathbf{a}_N$ are affinely dependent (or linearly dependent), which is a contradiction to (A2).

B.2 Proof of Theorem 4

By letting $\overline{\mathbf{X}} = [\, \tilde{\mathbf{x}}[1], \ldots, \tilde{\mathbf{x}}[L] \,] \in \mathbb{R}^{(N-1) \times L}$, the constraint of (5.12) can be expressed as

$$[\, \boldsymbol{\nu}_1, \ldots, \boldsymbol{\nu}_N \,] = \overline{\mathbf{X}} \boldsymbol{\Phi}, \tag{B.1}$$

for some $\mathbf{\Phi} \in \mathbb{R}_+^{L \times N}$ and $\mathbf{1}_L^T \mathbf{\Phi} = \mathbf{1}_N^T$. It follows by substituting (5.8) into (B.1) that

$$[\, \boldsymbol{\nu}_1, \ldots, \boldsymbol{\nu}_N \,] = [\, \boldsymbol{\alpha}_1, \ldots, \boldsymbol{\alpha}_N \,]\mathbf{S}\mathbf{\Phi}, \tag{B.2}$$

where $\mathbf{S} = [\, \mathbf{s}[1], \ldots, \mathbf{s}[L] \,] \in \mathbb{R}_+^{N \times L}$ [(A1)] and $\mathbf{1}_N^T \mathbf{S} = \mathbf{1}_L^T$ [(A5)]. From (4.29), one can further have an equivalent form of (B.2) given by

$$\mathbf{\Delta}(\boldsymbol{\nu}_1, \ldots, \boldsymbol{\nu}_N) = \mathbf{\Delta}(\boldsymbol{\alpha}_1, \ldots, \boldsymbol{\alpha}_N)\mathbf{Q}, \tag{B.3}$$

where $\mathbf{Q} = \mathbf{S}\mathbf{\Phi} \in \mathbb{R}_+^{N \times N}$ and $\mathbf{1}_N^T \mathbf{Q} = \mathbf{1}_N^T$. By (4.28) and Lemma 1 in [94], we can easily infer from (B.3) that

$$V(\boldsymbol{\nu}_1, \ldots, \boldsymbol{\nu}_N) = V(\boldsymbol{\alpha}_1, \ldots, \boldsymbol{\alpha}_N) \left|\det(\mathbf{Q})\right|, \tag{B.4}$$

$$\leq V(\boldsymbol{\alpha}_1, \ldots, \boldsymbol{\alpha}_N), \tag{B.5}$$

and the equality holds (or the the optimality of (5.12) is achieved) if and only if $\mathbf{Q}$ is a permutation matrix. This implies that the optimum solution for $\{\boldsymbol{\nu}_1, \ldots, \boldsymbol{\nu}_N\}$ is exactly $\{\boldsymbol{\alpha}_1, \ldots, \boldsymbol{\alpha}_N\}$ by (B.3).

Next, we will show (A3) is a sufficient and necessary condition for $\mathbf{Q}$ being a identity matrix (without loss of generality) under the premise of (A1) and (A5), i.e.,

$$\mathbf{Q} = \mathbf{S}\mathbf{\Phi} = \mathbf{I}_N. \tag{B.6}$$

We first prove the sufficiency of (A3). Under (A3), there exists an index set $\{\ell_1, \ldots, \ell_N\}$ such that $s_i[\ell_i] = 1$ and $s_i[\ell_j] = 0$ for all $i = 1, \ldots, N$ and $j \neq i$. It can be shown that there always exists a trivial solution of $\mathbf{\Phi}$ such that (B.6) holds, given by $\Phi_{\ell_i,i} = 1$ and $\Phi_{\ell,i} = 0$ for $\ell \neq \ell_i$ and $i = 1, \ldots, N$, where $\Phi_{p,q}$ denotes the (p, q)-th entry of $\mathbf{\Phi}$.

We prove necessity of (A3) by contradiction. Assuming that (A3) is not satis-

fied for all sources $\boldsymbol{s}_1, \ldots, \boldsymbol{s}_N$, then there must exist at least one source, say $\boldsymbol{s}_i = [\ s_i[1], \ldots, s_i[L]\ ]^T$, such that $s_i[n] < 1$ for all n. Then, the (i, i)th entry of $\mathbf{Q}$ given by

$$q_{ii} = \sum_{n=1}^{L} s_i[n]\Phi_{n,i} \leq \max_n\{s_i[n]\} < 1, \tag{B.7}$$

implies that $\mathbf{Q} \neq \mathbf{I}_N$. Hence, we complete the proof. ∎

B.3 Proof of Theorem 5

The constraint of (5.14) can be equivalently written as

$$\text{conv}\{\tilde{\mathbf{x}}[1], \ldots, \tilde{\mathbf{x}}[L]\} \subseteq \text{conv}\{\boldsymbol{\beta}_1, \ldots, \boldsymbol{\beta}_N\}. \tag{B.8}$$

Under (A3), we can have

$$\text{conv}\{\tilde{\mathbf{x}}[1], \ldots, \tilde{\mathbf{x}}[L]\} = \text{conv}\{\tilde{\mathbf{x}}[\ell_1], \ldots, \tilde{\mathbf{x}}[\ell_N]\}$$
$$= \text{conv}\{\boldsymbol{\alpha}_1, \ldots, \boldsymbol{\alpha}_N\}. \tag{B.9}$$

Hence, (B.8) becomes $\text{conv}\{\boldsymbol{\alpha}_1, \ldots, \boldsymbol{\alpha}_N\} \subseteq \text{conv}\{\boldsymbol{\beta}_1, \ldots, \boldsymbol{\beta}_N\}$, which means $\boldsymbol{\alpha}_i \in \text{conv}\{\boldsymbol{\beta}_1, \ldots, \boldsymbol{\beta}_N\}$, i.e.,

$$\boldsymbol{\alpha}_i = \sum_{j=1}^{N} \theta_{ij}\boldsymbol{\beta}_j \tag{B.10}$$

where $\sum_{j=1}^{N} \theta_{ij} = 1$ and $\theta_{ij} \geq 0$ for $i = 1, \ldots, N$. Then, from (4.29) and (B.10), one can easily infer that

$$\boldsymbol{\Delta}(\boldsymbol{\alpha}_1, \ldots, \boldsymbol{\alpha}_N) = \boldsymbol{\Delta}(\boldsymbol{\beta}_1, \ldots, \boldsymbol{\beta}_N)\boldsymbol{\Theta}^T, \tag{B.11}$$

where $\boldsymbol{\Theta} = [\theta_{ij}] \in \mathbb{R}_+^{N \times N}$ and $\boldsymbol{\Theta} \mathbf{1}_N = \mathbf{1}_N$. By (B.11) and (4.28), we can have

$$V(\boldsymbol{\alpha}_1, \ldots, \boldsymbol{\alpha}_N) = \left| \det \left(\boldsymbol{\Delta}(\boldsymbol{\beta}_1, \ldots, \boldsymbol{\beta}_N) \boldsymbol{\Theta}^T \right) \right| / (N-1)! \tag{B.12}$$

$$= V(\boldsymbol{\beta}_1, \ldots, \boldsymbol{\beta}_N) \left| \det \left(\boldsymbol{\Theta} \right) \right|. \tag{B.13}$$

According to Lemma 1 reported in [94], we have $\left| \det \left(\boldsymbol{\Theta} \right) \right| \le 1$ and the equality holds if and only if $\boldsymbol{\Theta}$ is a permutation matrix. Hence, we can easily see from (B.13) that

$$V(\boldsymbol{\alpha}_1, \ldots, \boldsymbol{\alpha}_N) \le V(\boldsymbol{\beta}_1, \ldots, \boldsymbol{\beta}_N), \tag{B.14}$$

and that the equality holds (or the the optimality of (5.14) is achieved) if and only if $\boldsymbol{\Theta}$ is a permutation matrix. This further implies that the optimum solution for $\{\boldsymbol{\beta}_1, \ldots, \boldsymbol{\beta}_N\}$ is exactly $\{\boldsymbol{\alpha}_1, \ldots, \boldsymbol{\alpha}_N\}$ by (B.10). $\blacksquare$
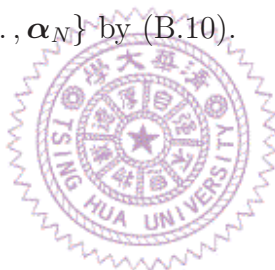
Bibliography

[1] A. Hyvärinen, J. Karhunen, and E. Oja, *Independent Component Analysis.* New York: John Wiley, 2001.

[2] A. Cichocki and S. Amari, *Adaptive Blind Signal and Image Processing.* John Wiley and Sons, Inc., 2002.

[3] L. Parra and C. Spence, "Convolutive blind separation of non-stationary sources," *IEEE Trans. Speech Audio Process.*, vol. 8, no. 3, pp. 320–327, 2000.

[4] D.-T. Pham and J.-F. Cardoso, "Blind separation of instantaneous mixtures of nonstationary sources," *IEEE Trans. Signal Process.*, vol. 49, no. 9, pp. 1837–1848, 2001.

[5] A. Prieto, C. G. Puntonet, and B. Prieto, "A neural learning algorithm for blind separation of sources based on geometric properties," *Signal Processing*, vol. 64, pp. 315–331, 1998.

[6] A. T. Erdogan, "A simple geometric blind source separation method for bound magnitude sources," *IEEE Trans. Signal Process.*, vol. 54, no. 2, pp. 438–449, 2006.

[7] F. Vrins, J. A. Lee, and M. Verleysen, "A minimum-range approach to blind extraction of bounded sources," *IEEE Trans. Neural Netw.*, vol. 18, no. 3, pp. 809–822, 2006.

[8] Y. Wang, J. Xuan, R. Srikanchana, and P. L. Choyke, "Modeling and reconstruction of mixed functional and molecular patterns," *Intl. J. Biomed. Imaging*, p. ID29707, 2006.

[9] N. Keshava and J. Mustard, "Spectral unmixing," *IEEE Signal Process. Mag.*, vol. 19, no. 1, pp. 44–57, Jan. 2002.

[10] E. R. Malinowski, *Factor Analysis in Chemistry.* New York: John Wiley, 2002.

[11] M. D. Plumbley, "Algorithms for non-negative independent component analysis," *IEEE Trans. Neural Netw.*, vol. 14, no. 3, pp. 534–543, 2003.

[12] S. A. Astakhov, H. Stogbauer, A. Kraskov, and P. Grassberger, "Monte Carlo algorithm for least dependent non-negative mixture decomposition," *Analytical Chemistry*, vol. 78, no. 5, pp. 1620–1627, 2006.

[13] S. Moussaoui, D. Brie, A. Mohammad-Djafari, and C. Carteret, "Separation of non-negative mixture of non-negative sources using a Bayesian approach and MCMC sampling," *IEEE Trans. Signal Process.*, vol. 54, no. 11, pp. 4133–4145, Nov. 2006.

[14] M. D. Plumbley, "Conditions for nonnegative independent component analysis," *IEEE Signal Processing Letters*, vol. 9, no. 6, pp. 177–180, 2002.

[15] D. D. Lee and H. S. Seung, "Learning the parts of objects by non-negative matrix factorization," *Nature*, vol. 401, pp. 788–791, Oct. 1999.

[16] ——, "Algorithms for non-negative matrix factorization," in *NIPS*. MIT Press, 2001, pp. 556–562.

[17] R. Zdunek and A. Cichocki, "Nonnegative matrix factorization with constrained second-order optimization," *Signal Processing*, vol. 87, no. 8, pp. 1904–1916, 2007.

[18] C. Lawson and R. J. Hanson, *Solving Least-Squares Problems*. New Jersey: Prentice-Hall, 1974.

[19] R. Tauler and B. Kowalski, "Multivariate curve resolution applied to spectral data from multiple runs of an industrial process," *Anal. Chem.*, vol. 65, pp. 2040–2047, 1993.

[20] A. Zymnis, S.-J. Kim, J. Skaf, M. Parente, and S. Boyd, "Hyperspectral image unmixing via alternating projected subgradients," in *41st Asilomar Conference on Signals, Systems, and Computers*, Pacific Grove, CA, Nov. 4-7, 2007.

[21] C.-J. Lin, "Projected gradient methods for non-negative matrix factorization," *Neural Computation*, vol. 19, no. 10, pp. 2756–2779, 2007.

[22] H. Laurberg, M. G. Christensen, M. D. Plumbley, L. K. Hansen, and S. H. Jensen, "Theorems on positive data: On the uniqueness of NMF," *Computational Intelligence and Neuroscience*, p. ID764206, 2008.

[23] P. Hoyer, "Nonnegative sparse coding," in *IEEE Workshop on Neural Networks for Signal Processing*, Martigny, Switzerland, Sept. 4-6, 2002, pp. 557–565.

[24] H. Kim and H. Park, "Sparse non-negative matrix factorizations via alternating non-negativity-constrained least squares for microarray data analysis," *Bioinformatics*, vol. 23, no. 12, pp. 1495–1502, 2007.

[25] W.-K. Ma, T. N. Davidson, K. M. Wong, Z.-Q. Luo, and P. C. Ching, "Quasi-maximum-likelihood multiuser detection using semi-definite relaxation with application to synchronous CDMA," *IEEE Trans. Signal Process.*, vol. 50, no. 4, pp. 912–922, April 2002.

[26] D. P. Palomar, J. M. Cioffi, and M. A. Lagunas, "Joint Tx-Rx beamforming design for multicarrier MIMO channels: A unified framework for convex optimization," *IEEE Trans. Signal Process.*, vol. 51, no. 9, pp. 2381–2401, 2003.

[27] Z.-Q. Luo, T. N. Davidson, G. B. Giannakis, and K. M. Wong, "Transceiver optimization for block-based multiple access through ISI channels," *IEEE Trans. Signal Process.*, vol. 52, no. 4, pp. 1037–1052, 2004.

[28] Y. Ding, T. N. Davidson, Z.-Q. Luo, and K. M. Wong, "Minimum BER block precoders for zero-forcing equalization," *IEEE Trans. Signal Process.*, vol. 51, no. 9, pp. 2410–2423, 2003.

[29] A. Wiesel, Y. C. Eldar, and S. Shamai, "Linear precoding via conic optimization for fixed MIMO receivers," *IEEE Trans. Signal Process.*, vol. 54, no. 1, pp. 161–176, 2006.

[30] N. D. Sidiropoulos, T. N. Davidson, and Z.-Q. Luo, "Transmit beamforming for physical-layer multicasting," *IEEE Trans. Signal Process.*, vol. 54, no. 6, pp. 2239–2251, 2006.

[31] S. A. Vorobyov, A. B. Gershman, and Z.-Q. Luo, "Robust adaptive beamforming using worst-case performance optimization: A solution to the signal mismatch problem," *IEEE Trans. Signal Process.*, vol. 51, no. 2, pp. 313–324, 2003.

[32] P. Biswas, T.-C. Lian, T.-C. Wang, and Y. Ye, "Semidefinite programming based algorithms for sensor network localization," *ACM Trans. Sensor Networks*, vol. 2, no. 2, pp. 188–220, 2006.

[33] F.-Y. Wang, Y. Wang, T.-H. Chan, and C.-Y. Chi, "Blind separation of multi-channel biomedical image patterns by non-negative least-correlated component analysis," in *Lecture Notes in Bioinformatics (Proc. PRIB'06), Springer-Verlag*, vol. 4146, Berlin, Dec. 9-14, 2006, pp. 151–162.

[34] F.-Y. Wang, C.-Y. Chi, T.-H. Chan, and Y. Wang, "Blind separation of positive dependent sources by non-negative least-correlated component analysis," in *IEEE International Workshop on Machine Learning for Signal Processing (MLSP'06)*, Maynooth, Ireland, Sept. 6-8, 2006, pp. 73–78.

[35] J. W. Boardman, "Automating spectral unmixing of AVIRIS data using convex geometry concepts," in *Proc. Summ. 4th Annu. JPL Airborne Geosci. Workshop*, vol. 1, Dec. 9-14, 1993, pp. 11–14.

[36] ——, "Geometric mixture analysis of imaging spectrometry data," in *Proc. IEEE International Geoscience and Remote Sensing Symposium*, vol. 4, Pasadena, CA, Aug. 8-12, 1994, pp. 2369–2371.

[37] T.-H. Chan, W.-K. Ma, C.-Y. Chi, and Y. Wang, "A convex analysis based criterion for blind separation of non-negative sources," in *Proc. IEEE International Conference on Acoustics, Speech, and Signal Processing*, Honolulu, Hawaii, April 15-20, 2007, pp. 961–964.

[38] ——, "Blind separation of non-negative sources by convex analysis: Effective method using linear programming," in *Proc. IEEE International Conference on Acoustics, Speech, and Signal Processing*, Las Vegas, Nevada, USA, March 30 - April 4, 2008.

[39] ——, "A convex analysis framework for blind separation of non-negative sources," *IEEE Trans. Signal Processing*, vol. 56, no. 10, pp. 5120–5134, Oct. 2008.

[40] T.-H. Chan, C.-Y. Chi, Y.-M. Huang, and W.-K. Ma, "A convex analysis based minimum-volume enclosing simplex algorithm for hyperspectral unmixing," in *Proc. IEEE International Conference on Acoustics, Speech, and Signal Processing*, Taipei, Taiwan, April 19-24, 2009, pp. 1089–1092.

[41] T.-H. Chan, W.-K. Ma, C.-Y. Chi, and A. ArulMurugan, "Hyperspectral unmixing from a convex analysis and optimization perspective," in *Proc. First IEEE Workshop on Hyperspectral Image and Signal Processing: Evolution in Remote Sensing (WHISPERS)*, Grenoble, France, Aug. 26-28, 2009.

[42] T.-H. Chan, C.-Y. Chi, Y.-M. Huang, and W.-K. Ma, "A convex analysis based minimum-volume enclosing simplex algorithm for hyperspectral unmixing," to appear in *IEEE Trans. Signal Processing*, 2009.

[43] M. E. Winter, "N-findr: An algorithm for fast autonomous spectral end-member determination in hyperspectral data," in *Proc. SPIE Conf. Imaging Spectrometry*, Pasadena, CA, Oct. 1999, pp. 266–275.

[44] ——, "A proof of the N-FINDR algorithm for the automated detection of endmembers in a hyperspectral image," in *Proc. SPIE Conf. Algorithms and Technologies for Multispectral, Hyperspectral, and Ultraspectral Imagery*, vol. 5425, Aug. 2004, pp. 31–41.

[45] M. D. Craig, "Minimum-volume transforms for remotely sensed data," *IEEE Trans. Geosci. Remote Sens.*, vol. 32, no. 3, pp. 542–552, May 1994.

[46] E. Hillman and A. Moore, "All-optical anatomical co-registration for molecular imaging of small animals using dynamic contrast," *Nature Photonics Letters*, vol. 1, pp. 526–530, 2007.

[47] G. Shaw and D. Manolakis, "Signal processing for hyperspectral image exploitation," *IEEE Signal Process. Mag.*, vol. 19, no. 1, pp. 12–16, Jan. 2002.

[48] S. Boyd and L. Vandenberghe, *Convex Optimization.* Cambridge Univ. Press, 2004.

[49] D. P. Bertsekas, A. Nedić, and A. E. Ozdaglar, *Convex Analysis and Optimization.* Athena Scientific, 2003.

[50] B. Grünbaum, *Convex Polytopes.* Springer, 2003.

[51] M. E. Dyer, "The complexity of vertex enumeration methods," *Mathematics of Operations Research*, vol. 8, no. 3, pp. 381–402, 1983.

[52] K. G. Murty and S.-J. Chung, "Extreme point enumeration," College of Engineering, University of Michigan," Technical Report 92-21, 1992, available online: `http://deepblue.lib.umich.edu/handle/2027.42/6731`.

[53] K. Fukuda, T. M. Liebling, and F. Margot, "Analysis of backtrack algorithms for listing all vertices and all faces of a convex polyhedron," *Computational Geometry: Theory and Applications*, vol. 8, no. 1, pp. 1–12, 1997.

[54] J. F. Sturm, "Using SeDuMi 1.02, a MATLAB toolbox for optimization over symmetric cones," *Optimization Methods and Software*, vol. 11-12, pp. 625–653, 1999.

[55] I. J. Lustig, R. E. Marsten, and D. F. Shanno, "Interior point methods for linear programming: Computational state of the art," *ORSA Journal on Computing*, vol. 6, no. 1, pp. 1–14, 1994.

[56] G. H. Golub and C. F. V. Loan, *Matrix Computations.* The Johns Hopkins University Press, 1996.

[57] G. Strang, *Linear Algebra and Its Applications*, 4th ed. CA: Thomson, 2006.

[58] P. Tichavský and Z. Koldovský, "Optimal pairing of signal components separated by blind techniques," *IEEE Signal Process. Lett.*, vol. 11, no. 2, pp. 119–122, 2004.

[59] J. R. Hoffman and R. P. S. Mahler, "Multitarget miss distance via optimal assignment," *IEEE Trans. System, Man, and Cybernetics*, vol. 34, no. 3, pp. 327–336, May 2004.

[60] H. W. Kuhn, "The Hungarian method for the assignment method," *Naval Research Logistics Quarterly*, vol. 2, pp. 83–97, 1955.

[61] S. G. Armato, "Enhanced visualization and quantification of lung cancers and other diseases of the chest," *Experimental Lung Res.*, vol. 30, no. 30, pp. 72–77, 2004.

[62] K. Suzuki, R. Engelmann, H. MacMahon, and K. Doi, "Virtual dual-energy radiography: Improved chest radiographs by means of rib suppression based on a massive training artificial neural network (MTANN)," *Radiology*, vol. 238. [Online]. Available: `http://suzukilab.uchicago.edu/research.htm`

[63] *Virtual Mouse Necropsy*, available online: `http://www3.niaid.nih.gov/labs/aboutlabs/cmb/InfectiousDiseasePathogenesisSection/mouseNecropsy/step6IntestinesStomachSpleenPancreas.htm`.

[64] M. E. Dickinson, G. Bearman, S. Tille, R. Lansford, and S. E. Fraser, "Multi-spectral imaging and linear unmixing add a whole new dimension to laser scanning fluorescence microscopy," *BioTechniques*, vol. 31, no. 6, pp. 1272–1278, Jan. 2001.

[65] J. R. Mansfield, K. W. Gossage, C. C. Hoyt, and R. M. Levenson, "Autofluorescence removal, multiplexing, and automated analysis methods for in-vivo fluorescence imaging," *Journal of Biomedical Optics*, vol. 10, no. 4, p. 041207, Aug. 2005.

[66] R. M. Levenson and J. R. Mansfield, "Multispectral imaging in biology and medicine: Slices of life," *International Society for Analytical Cytology*, vol. 69, no. 8, pp. 748–758, Aug. 2006.

[67] T. M. Lillesand, R. W. Kiefer, and J. W. Chipman, *Remote Sensing and Image Interpretation*, 2nd ed. New York: Wiley, 2004.

[68] J. A. Richards, "Analysis of remotely sensed data: The formative decades and the future," *IEEE Trans. Geosci. Remote Sens.*, vol. 43, no. 2, pp. 422–432, Mar. 2005.

[69] B. A. Campbell, *Radar Remote Sensing of Planetary Surfaces*. New York: Cambridge University Press, 2002.

[70] R. N. Clark, G. A. Swayze, K. E. Livo, R. F. Kokaly, S. Sutley, J. B. Dalton, R. R. McDougal, and C. A. Gent, "Imaging spectroscopy: Earth and planetary remote sensing with the USGS tetracorder and expert systems," *Journal of Geophysical Research*, vol. 108, no. 12, pp. 5–44, Dec. 2003.

[71] D. Landgrebe, "Hyperspectral image data analysis," *IEEE Signal Process. Mag.*, vol. 19, no. 1, pp. 17–28, Jan. 2002.

[72] D. Stein, S. Beaven, L. Hoff, E. Winter, A. Schaum, and A. Stocker, "Anomaly detection from hyperspectral imagery," *IEEE Signal Process. Mag.*, vol. 19, no. 1, pp. 58–69, Jan. 2002.

[73] N. Keshava, "A survey of spectral unmixing algorithms," *Lincoln Lab. Journal*, vol. 14, no. 1, pp. 55–78, Jan. 2003.

[74] M. O. Smith, P. E. Johnson, and J. B. Adams, "Quantitative determination of mineral types and abundances from reflectance spectra using principal component analysis," *Journal Geophys. Res.*, vol. 90, no. 2, pp. C797–C804, Oct. 1985.

[75] A. A. Green, "A transformation for ordering multispectral data in terms of image quality with implications for noise removal," *IEEE Trans. Geosci. Remote Sens.*, vol. 32, no. 1, pp. 65–74, May 1988.

[76] C.-I. Chang and Q. Du, "Estimation of number of spectrally distinct signal sources in hyperspectral imagery," *IEEE Trans. Geosci. Remote Sens.*, vol. 42, no. 3, pp. 608–619, Mar. 2004.

[77] J. M. Bioucas-Dias and J. M. P. Nascimento, "Hyperspectral subspace identification," *IEEE Trans. Geosci. Rem. Sens.*, vol. 46, no. 8, pp. 2435–2445, 2008.

[78] J. W. Boardman, F. A. Kruse, and R. O. Green, "Mapping target signatures via partial unmixing of AVIRIS data," in *Proc. Summ. JPL Airborne Earth Sci. Workshop*, vol. 1, Pasadena, CA, Dec. 9-14, 1995, pp. 23–26.

[79] J. M. P. Nascimento and J. M. B. Dias, "Vertex component analysis: A fast algorithm to unmix hyperspectral data," *IEEE Trans. Geosci. Remote Sens.*, vol. 43, no. 4, pp. 898–910, Apr. 2005.

[80] A. Ifarraguerri and C.-I. Chang, "Multispectral and hyperspectral image analysis with convex cones," *IEEE Trans. Geosci. Remote Sens.*, vol. 37, no. 2, pp. 756–770, Mar. 1999.

[81] D. Heinz and C.-I. Chang, "Fully constrained least squares linear mixture analysis for material quantification in hyperspectral imagery," *IEEE Trans. Geosci. Remote Sens.*, vol. 39, no. 3, pp. 529–545, Mar. 2001.

[82] M. Berman, H. Kiiveri, R. Lagerstrom, A. Ernst, R. Dunne, and J. F. Huntington, "ICE: A statistical approach to identifying endmembers in hyperspectral images," *IEEE Trans. Geosci. Remote Sens.*, vol. 42, no. 10, pp. 2085–2095, Oct. 2004.

[83] V. P. Pauca, J. Piper, and R. J. Plemmons, "Nonnegative matrix factorization for spectral data analysis," *Linear Algebra Appl.*, vol. 1, no. 416, pp. 29–47, 2006.

[84] N. Dobigeon, S. Moussaoui, M. Coulon, J.-Y. Tourneret, and A. O. Hero, "Joint Bayesian endmember extraction and linear unmixing for hyperspectral imagery," to appear in *IEEE Trans. Signal Processing*, 2009.

[85] J. Li and J. Bioucas-Dias, "Minimum volume simplex analysis: A fast algorithm to unmix hyperspectral data," in *Proc. IEEE International Geoscience and Remote Sensing Symposium*, vol. 4, Boston, MA, Aug. 8-12, 2008, pp. 2369–2371.

[86] L. Miao and H. Qi, "Endmember extraction from highly mixed data using minimum volume constrained nonnegative matrix factorization," *IEEE Trans. Geosci. Remote Sens.*, vol. 45, no. 3, pp. 765–777, Mar. 2007.

[87] P. Gritzmann and V. Klee, "On the complexity of some basic problems in computational convexity: I.: containment problems," *Discrete Mathematics*, vol. 136, no. 1-3, pp. 129–174, Dec. 1994.

[88] Y. Zhou and S. Suri, "Algorithms for a minimum volume enclosing simplex in three dimensions," *SIAM Journal on Computing*, vol. 31, no. 5, pp. 1339–1357, 2002.

[89] Tech. Rep., available online: `http://speclab.cr.usgs.gov/cuprite.html`.

[90] *AVIRIS Free Standard Data Products*, available online: `http://aviris.jpl.nasa.gov/html/aviris.freedata.html`.

[91] G. Swayze, R. Clark, S. Sutley, and A. Gallagher, "Ground-truthing AVIRIS mineral mapping at Cuprite, Nevada," in *Proc. Summ. 4th Annu. JPL Airborne Geosci. Workshop*, vol. 2, 1992, pp. 47–49.

[92] G. Swayze, "The hydrothermal and structural history of the Cuprite Mining District, southwestern Nevada: An integrated geological and geophysical approach," Ph.D. dissertation, University of Colorado, Boulder, 1997.

[93] R. N. Clark, G. A. Swayze, A. Gallagher, T. V. King, and W. M. Calvin, "The U.S. geological survey digital spectral library: Version 1: 0.2 to 3.0 μm," in *U.S. Geol. Surv., Open File Report 93-592*, 1993.

[94] F.-Y. Wang, C.-Y. Chi, T.-H. Chan, and Y. Wang, "Non-negative least-correlated component analysis for separation of dependent sources by volume maximization," to appear in *IEEE Trans. Pattern Analysis and Machine Intelligence*, 2009.

Publication List of The Author

Journal papers:

1. <u>T.-H. Chan</u>, W.-K. Ma, C.-Y. Chi, and Y. Wang, "A convex analysis framework for blind separation of non-negative sources," *IEEE Trans. Signal Processing*, vol. 56, no. 10, pp. 5120-5134, Oct. 2008.

2. F.-Y. Wang, C.-Y. Chi, <u>T.-H. Chan</u>, and Y. Wang, "Non-negative least-correlated component analysis for separation of dependent sources by volume maximization," to appear in *IEEE Trans. Pattern Analysis and Machine Intelligence*, 2009 (regular paper).

3. <u>T.-H. Chan</u>, C.-Y. Chi, Y.-M. Huang and W.-K. Ma, "A convex analysis based minimum-volume enclosing simplex algorithm for hyperspectral unmixing," to appear in *IEEE Trans. Signal Processing*, 2009 (regular paper).

Book Chapter:

1. W.-K. Ma, <u>T.-H. Chan</u>, C.-Y. Chi, and Y. Wang, "Convex analysis for non-negative blind source separation with application in imaging," a Chapter (41 pages) to appear in *Convex Optimization in Signal Processing and Communications*, Cambridge University Press, 2009.

International conference papers:

1. F.-Y. Wang, Y. Wang, <u>T.-H. Chan</u>, and C.-Y. Chi, "Blind separation of multichannel biomedical image patterns by non-negative least-correlated component analysis," in *Lecture Notes in Bioinformatics (Proc. PRIB'06)*, LNBI 4146, pp. 151-162, Springer-Verlag, Berlin, 2006.

2. F.-Y. Wang, C.-Y. Chi, <u>T.-H. Chan</u>, and Y. Wang, "Blind separation of positive dependent sources by non-negative least-correlated component analysis," in *Proc. IEEE International Workshop on Machine Learning for Signal Processing (MLSP)*, Maynooth, Ireland, Sept. 6-8, 2006, pp. 73-78.

3. <u>T.-H. Chan</u>, W.-K. Ma, C.-Y. Chi, and Y. Wang, "A convex analysis based criterion for blind separation of non-negative sources," in *Proc. IEEE International Conference on Acoustics, Speech, and Signal Processing (ICASSP)*, Honolulu, Hawaii, April 15-20, 2007, pp. 961-964.

4. <u>T.-H. Chan</u>, W.-K. Ma, C.-Y. Chi, and Y. Wang, "Blind separation of non-negative sources by convex analysis: Effective method using linear programming," in *Proc. IEEE International Conference on Acoustics, Speech, and Signal Processing (ICASSP)*, Las Vegas, Nevada, March 30-April 4, 2008, pp. 3493-3496.

5. L. Chen, <u>T.-H. Chan</u>, P. L. Choyke, C.-Y. Chi, G. Wang, and Y. Wang, "Convex analysis and separation of composite signals in DCE-MRI," in *Proc. 5th IEEE International Symposium on Biomedical Imaging: From Nano to Macro (ISBI)*, Paris, France, May 14-17, 2008, pp. 1557-1560.

6. <u>T.-H. Chan</u>, L. Chen, P. L. Choyke, C.-Y. Chi, G. Wang, and Y. Wang, "Convex analysis for separation of functional patterns in DCE-MRI: A longitudinal study to antiangiogenic therapy," in *Proc. IEEE International Workshop on Machine Learning for Signal Processing (MLSP)*, Cancún, Mexico, Oct. 16-19, 2008.

7. Yitan Zhu, <u>T.-H. Chan</u>, E. P. Hoffman, and Y. Wang, "Gene expression dissection by non-negative well-grounded source separation," in *Proc. IEEE International Workshop on Machine Learning for Signal Processing (MLSP)*, Cancún, Mexico, Oct. 16-19, 2008.

8. <u>T.-H. Chan</u>, C.-Y. Chi, Y.-M. Huang and W.-K. Ma, "A convex analysis based minimum-volume enclosing simplex algorithm for hyperspectral unmixing," in *Proc. IEEE International Conference on Acoustics, Speech, and Signal Processing (ICASSP)*, Taipei, Taiwan, April 19-24, 2009.

9. <u>T.-H. Chan</u>, W.-K. Ma, C.-Y. Chi, and A. ArulMurugan, "Hyperspectral unmixing from a convex analysis and optimization perspective," to appear in *Proc. First IEEE Workshop on Hyperspectral Image and Signal Processing: Evolution in Remote Sensing (WHISPERS)*, Grenoble, France, August 26-28, 2009. (Invited paper)

Papers to be submitted for publication:

1. L. Chen, <u>T.-H. Chan</u>, P. L. Choyke, C.-Y. Chi, G. Wang, and Y. Wang, "Unmixing tumor vasculature patterns in dynamic contrast-enhanced MRI," to be submitted to *IEEE Trans. Medical Imaging*.